Dielectric Characterization: A 3D EM Simulation Approach

Lyle M. Sewall

Thesis submitted to the faculty of the
Virginia Polytechnic Institute and State University
in partial fulfillment of the requirements for the degree of

Master of Science
In
Electrical Engineering

Sedki M. Riad, Chair
William A. Davis
Ahmad Safaai-Jazi

August 23rd, 2006
Blacksburg, VA

Keywords: Waveguide, Capacitor, Dielectric, Material, Characterization,
Electromagnetic Simulation, Simulator, Systematic Error

© 2006, Lyle M. Sewall

Dielectric Characterization: A 3D EM Simulation Approach

Lyle M. Sewall

ABSTRACT

A new approach is presented that relies upon 3D electromagnetic simulation results to characterize the complex permittivity of homogeneous dielectric materials. By modeling the test fixture and obtaining a set of simulated S-parameters through an iterative solution process, the dielectric constant and loss tangent can be found. With further development, the 3D simulation results may be used to replace the need for complex theoretical analysis of the measurement geometry.

The method is applied to an X-band rectangular waveguide setup, for which the theoretical S-parameters can be readily calculated. A Teflon sample, for which the dielectric properties are well-known, is used for all measurements and calculations. After presenting a detailed derivation to obtain the theoretical S-parameters, the Teflon sample is measured and compared to the theoretical results, from which the comparison shows great promise. An inverse solution algorithm is used to solve for the material properties from the experimental S-parameters.

Low-frequency measurement of the Teflon sheet was performed by using a dielectric capacitor test fixture. The results show the effect of an air gap between the electrode and sample, producing serious errors.

Acknowledgements

Above all, I would like to give thanks to Jesus Christ, who has given me the wisdom, vision, and strength to persevere through the tough moments encountered in this work. I would like to thank all of those who have been centrally involved in the completion of this work. Thank you, Dr. Riad, for your continuous grateful supervision and helpful suggestions, and Dr. Davis, for guiding me through a TRL calibration until 6PM on the Friday night of Memorial Day weekend. Thank you, Dr. Jazi, for the knowledge I gained in your 5105 class, which was put to constant use throughout my research. Finally, I would like to thank you, Dr. Attiya, for the extra time and grateful contributions you have given throughout the course of this work. All of your help will not be forgotten anytime soon!

This thesis is dedicated to my parents, John and Gloria, and my fiancée, Anne, for their endless support and encouragement.

Table of Contents

List of Figures……………………………………………………...……vi
List of Tables…………………….......………………………….….…....ix

Chapter 1: Introduction 1

Chapter 2: Literature Review of Characterization Methods 4
2.1 Introduction 4
2.2 Dielectric Permittivity Overview 4
2.3 Dielectric Characterization Considerations 8
2.4 Commonly-Used Methods 9
2.4.1 Parallel-Plate Capacitor 10
2.4.2 Coaxial Cavity 12
2.4.3 Rectangular Metallic Waveguide.. 17
2.4.4 Resonators.. 19
2.4.5 Open-Ended Coaxial Probe... 29
2.4.6 Free Space Methods.. 31
2.5 ASTM Standards... 34

Chapter 3: Capacitor Dielectric Characterization 35
3.1 Introduction 35
3.2 Overview of Capacitance.. 35
3.3 The Guarded Electrode 38
3.4 Sample Measurement... 41

Chapter 4: X-Band Waveguide Characterization of Thin Dielectric Sheets . 48
4.1 Introduction 48
4.2 Systematic Error.. 51
4.3 De-Embedding of Material S-parameters from Simulation 54
4.4 Theoretical S-parameters 64
4.5 Comparison of Theoretical and Simulated S-parameters............. 70
4.6 Inverse Solution 73
4.7 Sensitivity Analysis.. 80
4.8 Material Measurement 85
4.8.1 VNA TRL Calibration 86
4.8.2 Sample Preparation 87
4.8.3 8510C Measurement.. 90
4.8.4 Measurement Data... 90
4.8.5 Measurement Solution 94

Chapter 5: Conclusion **99**
Summary……………………………………………………………..…**99**
Recommended Future Work……………………………………………**100**
Conclusions………………………………..……………………..…..**102**

References……………………………………………………………..**103**

List of Figures

Figure 2-1: Diagram of atom in absence and presence of applied electric field……5
Figure 2-2: Parallel-plate capacitor in the presence of an applied electric field……6
Figure 2-3: The unguarded parallel-plate capacitor configuration………………….11
Figure 2-4: The guarded parallel-plate capacitor configuration…………………… 12
Figure 2-5: The coaxial in-line measurement setup………………………………...13
Figure 2-6: Setup for terminating cavity and through cavity measurements……….13
Figure 2-7: The coaxial terminating-cavity configuration………………………….15
Figure 2-8: The coaxial through-cavity configuration……………………………...16
Figure 2-9: The slotted waveguide measurement configuration……………………19
Figure 2-10: The dielectric stripline line resonator configuration………………….23
Figure 2-11: The dielectric stripline ring resonator configuration………………….25
Figure 2-12: The open-ended coaxial probe configuration…………………………30
Figure 2-13: The free-space measurement configuration………………………….. 32

Figure 3-1: Conceptual diagram of the parallel-plate capacitor…………………… 37
Figure 3-2: The guarded electrode parallel-plate configuration…………………… 39
Figure 3-3: Diagram of the four-terminal pair measurement architecture………… 39
Figure 3-4: Unguarded parallel-plate capacitor measurement conceptualization…. 40
Figure 3-5: Guarded parallel-plate capacitor measurement conceptualization……. 41
Figure 3-6: Picture of the HP 4192A low-frequency impedance analyzer…………42
Figure 3-7: Picture of the HP 16451B dielectric test fixture……………………….42
Figure 3-8: Guarded electrode dimensions for HP 16451B fixture………………...43
Figure 3-9: Picture of capacitive measurement setup with Teflon sample…………44
Figure 3-10: Experimental permittivity results from HP 16451B measurement
of Teflon sample….. 45
Figure 3-11: Expected error when using the HP 16451B test fixture………………46

Figure 3-12: Comparison of capacitive measurement techniques using
the HP 16451B test fixture……………………………………………….47

Figure 4-1: The dielectric waveguide measurement setup………………………… 50
Figure 4-2: Flow chart for verification of 3D electromagnetic
waveguide simulations………………………………………….........54
Figure 4-3: Component breakdown for the waveguide measurement setup………. 56
Figure 4-4: The S-parameter signal flow diagram of the cascaded
waveguide configuration…………………………………………………57
Figure 4-5: Side view of the asymmetrical sample holder……………………… 63
Figure 4-6: Theoretical bounce diagram for dielectric inserted between
two air-filled waveguide sections……………………………………….. 66
Figure 4-7: Bounce diagram expanded to include the extra
sample-holder length……………………………………………………..68
Figure 4-8: Conceptual side-view of the sample holder…………………………… 69
Figure 4-9: Comparison of s_{11} magnitude and phase for Teflon
sample measured in closed waveguide setup………………………………71
Figure 4-10: Comparison of s_{11} magnitude and phase for Teflon
sample measured in closed waveguide setup………………………………72
Figure 4-11: Flow diagram of the optimization routine used
in the inverse solution algorithm…………………………………………78
Figure 4-12: Dielectric constant solution using unknown simulation case………... 79
Figure 4-13: Loss tangent solution using unknown simulation case………………80
Figure 4-14: Dielectric constant sensitivity for low-loss dielectrics………………. 81
Figure 4-15: Dielectric constant sensitivity for high-loss dielectrics……………… 82
Figure 4-16: Loss tangent sensitivity for low-ε_r dielectrics……………………….. 83
Figure 4-17: Loss tangent sensitivity for high-ε_r dielectrics………………………..84
Figure 4-18: Picture of the HP 8510C VNA used for waveguide measurements…. 85
Figure 4-19: Collage of pictures outlining the basic TRL calibration process……..87
Figure 4-20: Collage of pictures of forward and reverse-isolation measurements…87
Figure 4-21: Side view of the material-filled sample holder………………………89

Figure 4-22: s_{11} magnitude from waveguide measurement of Teflon sample…….. 90
Figure 4-23: s_{11} phase from waveguide measurement of Teflon sample………….. 91
Figure 4-24: s_{21} magnitude from waveguide measurement of Teflon sample…….. 91
Figure 4-25: s_{21} phase from waveguide measurement of Teflon sample………….. 92
Figure 4-26: s_{21} magnitude from direct connection of waveguide
launcher sections……………………………………………………………93
Figure 4-27: s_{21} phase from direct connection of waveguide launcher sections…... 93
Figure 4-28: Waveguide dielectric constant solution vs. frequency
for Teflon sample…………………………………………………………...94
Figure 4-29: Waveguide loss tangent solution vs. frequency
for Teflon sample…………………………………………………………...95
Figure 4-30: Waveguide dielectric constant solution vs. frequency for
Teflon sample on alternate setup with HP 11644 TRL calibration kit…….. 96
Figure 4-31: Waveguide loss tangent solution vs. frequency for
Teflon sample on alternate setup with HP 11644 TRL calibration kit…….. 96
Figure 4-32: Waveguide dielectric constant solution vs. frequency
for PCB sample……………………………………………………………..97
Figure 4-33: Waveguide loss tangent solution vs. frequency for PCB sample……. 97

List of Tables

Table 4-1: Guided wavelengths across frequency range of interest in the x-band… 61

Table 4-2: Table of material values used to construct 3-dimensional error library... 74

Chapter 1
Introduction

The characterization of dielectric materials has long been an area of intensive research interest. The permittivity, permeability, and conductivity of a given material are all of paramount interest in decisions of how a given material will be utilized. Even though many effective characterization methods have been developed, there is an ongoing effort to create newer, better techniques that produce higher precision results with higher efficiency. There are a number of reasons that the electrical properties of materials have remained an area of widespread significance:

- The concentration of the electric fields within any material is directly related to its complex permittivity.
- Wave propagation through material substrates is a critical parameter in the performance of high-speed circuits.
- Better manufacturing quality control can be achieved through careful measurement of produced materials [1].
- Accurate material measurement allows engineers and scientists to more effectively incorporate the material into its intended application [1].
- Recent advances in the industrial processing of foods, rubber, plastic, ceramics, and other materials have benefited from additional knowledge of their electrical properties [1].

Even though many different approaches have been devised to electrically characterize material properties, they all rely on the same underlying technique. By applying an excitation to a material and observing the resulting phase and magnitude response of the reflected and transmitted signals, the electrical material properties of a sample can be determined. Measurements are typically taken in the form of complex impedances or S-parameters with a vector impedance analyzer or vector network analyzer, respectively.

In this work, the main focus will be on the development and use of the rectangular waveguide in the X-band to characterize the complex permittivity of homogeneous, isotropic, linear, time-invariant materials. However, an alternative method will first be employed, in which an HP capacitor test fixture will be used to obtain a baseline value of the material properties at low frequencies. By first using a separate method, a low-frequency estimation of the sample material's properties can be obtained, and can be useful when analyzing the results that are later obtained through the waveguide approach. Obtaining confidence in and providing support for the results is an essential process if a method is to gain widespread acceptance in the field of dielectric characterization.

One of the primary difficulties faced when attempting to characterize the unknown properties of a material is in the theoretical calculation of the electromagnetic fields pertaining to the geometry in which the material is being measured. If the distribution of fields is not known with any level of certainty, then there will always be a corresponding level of uncertainty in the calculation of the permittivity from the measured data. This thesis begins exploration into a method which could potentially relax the requirement that the theoretically fields be strictly derived. By using a simulated field solution rather than strict theoretical analysis, more complex structures may become useful for the characterization of unknown electrical properties. The assistance of readily available electromagnetic field simulation results is appealing for multiple reasons:

- A number of geometries are readily constructed, but due to their complexity, have been deemed unacceptable due to the complexity of their electromagnetic field distribution
- Material properties can be measured in the same geometry that they will eventually be incorporated into.
- For configurations in which a theoretical field solution is already available, the simulation can provide supplementary correction of unexplained systematic errors.

Chapter 2 gives a quick overview of material permittivity and a comprehensive review of currently used methods in the field of dielectric characterization. Chapter 3

reviews the theory allowing the use of capacitors to characterize material properties, then presents measurement results taken with a parallel-plate capacitor test fixture. Chapter 4 presents a material characterization technique, utilizing rectangular metallic waveguides, which makes use of a 3D simulated error-library to reduce the effects of systematic error upon the calculated complex permittivity. Finally, conclusions and recommendations for future work are discussed in chapter 5.

Chapter 2

Literature Review of Dielectric Characterization Methods

2.1 Introduction

In order to fully characterize a material, numerous methods should be used to verify the results and cover the entire desired frequency range. The complex permittivity of a material is partially dependent upon frequency, and methods covering a large span of frequencies are necessary to fully and effectively characterize the material.

A large amount of research has been conducted involving the interaction of electromagnetic waves with a medium. By observing the response of a material under test to an electromagnetic excitation, the data can then be compared to the predicted theoretical response, which is given by the application of Maxwell's equations to the geometry of interest. From this comparison, the electrical properties can be determined.

This thesis deals only with the characterization of the complex permittivity of a material and assumes the material is non-magnetic with a relative permeability μ_r of 1. The real part of the permittivity is most directly related to the propagation velocity of waves in a material, while the imaginary part is directly linked to the losses incurred as electromagnetic waves travel through a medium. It is assumed that the material is homogeneous, isotropic, linear, and time-invariant.

2.2 Dielectric Permittivity Overview

The permittivity of a dielectric material is best explained by viewing the electrical response of the material at a microscopic level. Dielectrics are defined as materials in which the primary charges in the atoms and molecules are bound charges held in place by atomic and molecular forces [2]. Since the bound charges are constrained to a given region within the material, they are not able to conduct freely, as are free charges within a conductor. Rather, the electrons shift slightly in response to applied electrical fields. This phenomenon creates a large number of electric dipoles within the material.

Figure 2-1 shows the atomic behavior of an atom in the absence and presence of an applied electric field. Under the applied field, the charges within the atom align themselves to the electric field in a process known as orientational polarization. A dipole moment is created, since the positive and negative charges are separated in space by a finite distance. Note that in the case of free charges, there are no restraining forces to retain the charges within a given region, so they will continue to move in opposite directions. This dipole moment can be compared to the stretching of a rubber band, in which potential energy is stored. In the case of polar molecules, potential energy is stored in the process of rotational alignment. To analyze the material on a macroscopic level, the total polarization vector *P* can be approximately quantified as the product of the material volume by the estimated number of dipoles per unit volume.

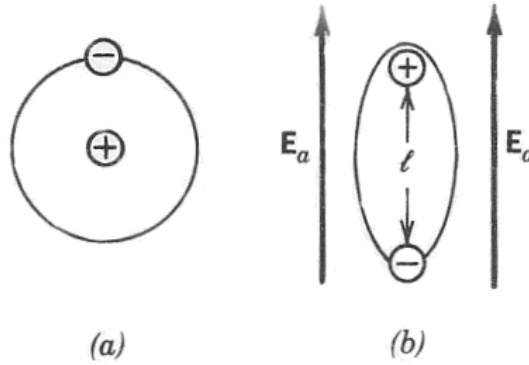

Figure 2-1. Typical atom in (a) the absence of and (b) under an applied field [2].

To further explain the idea of bound charge, we now observe the effects of a partially-dielectric-filled parallel-plate capacitor in the presence of a finite voltage potential difference between the capacitor plates. A Voltage source is applied to the capacitor as shown in Figure 2-2. In the area containing free space as the medium, the electric field is constant between the plates and its magnitude is represented by V/d, where d is the distance separating the plates. In the area containing the dielectric medium, the majority of the dipoles in the material align to the electric field, while the oppositely charged adjacent bound charges cancel one another out. This leaves a certain amount of bound charge on each plate, which is neutralized by the free charges on the capacitor plates. The voltage on the plates, however, must remain constant, which leads to the introduction of additional free charges on the capacitor plates.

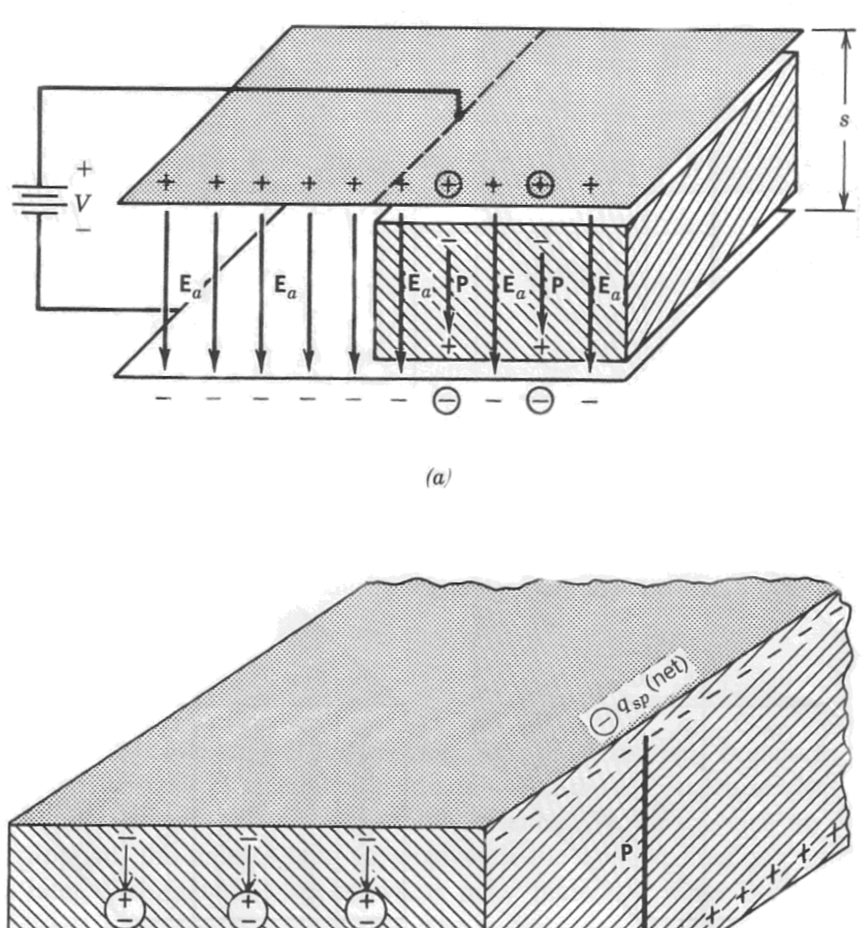

Figure 2-2. Dielectric slab subjected to an applied electric field E_a [2]. (a) Total charge. (b) Net charge.

The net result is a polarization vector P in the same direction as the applied electric field E_a. In the free space area of the capacitor the electric flux density D_o is related to the applied electric field E_a as follows:

$$D_o = \varepsilon_o E_a \tag{2.1}$$

In the medium-filled region, the polarization and electric field vectors can be added together to give the internal electric flux density D, where

$$D = \varepsilon_o E_a + P \tag{2.2}$$

The polarization vector P can be related to E_a by

$$P = \varepsilon_o \chi_e E_a \tag{2.3}$$

where χ_e is a quantity known as the electric susceptibility. By combining (2.2) and (2.3), the expression

$$D = \varepsilon_o (1 + \chi_e) E_a = \varepsilon_s E_a \tag{2.4}$$

is obtained, where ε_s is called the static permittivity of the material. The relative permittivity ε_r of a material, which is also commonly known as the dielectric constant, is given by the relation

$$\varepsilon_r = \frac{\varepsilon_s}{\varepsilon_o} = 1 + \chi_e \tag{2.5}$$

The dielectric constant, therefore, relates the charge-storage capabilities of a material to that of free-space. It must be noted that ε_r is, in general, complex and is sometimes variant with frequency. It is generally expressed as

$$\varepsilon^* = \varepsilon' - j\varepsilon'' \tag{2.6}$$

where

ε^* = complex permittivity

ε' = dielectric constant

ε'' = dielectric loss factor

To facilitate easier observation of the loss factor, an the loss tangent, tan(δ), is defined as

$$\tan\delta = \frac{\varepsilon''}{\varepsilon'} \tag{2.7}$$

The frequency-dependence of the permittivity and losses within the material is explained by Debye's relaxation time, which refers to the time it takes for the bound charges within the material to return to their equilibrium state following the removal of the applied electric field. The correlation between the frequency dependence of ε' and ε'' is quantified by the Kramers-Kronig dispersion relations [3].

2.3 Dielectric Characterization Considerations

There are many different methods of material characterization, and many considerations that must be taken into account before deciding which method to use. Some factors of consideration are as follows:

- Degree of accuracy required
- Frequency the material is intended for
- Homogeneity
- Linearity
- Time-variance
- Temperature-Dependence
    - Care should be taken to measure sample thickness and conduct the measurement all at the same laboratory temperature
- Surface Roughness
- Field orientation (some cases)
- Lossy vs. lossless materials
- Anisotropy
    - Requires both in-plane and normal-to-plane material measurements of ε', since they will differ based on field orientation. This usually requires two completely different techniques. For most materials, ε'' is not as dependent upon field orientation and only one measurement is required

Each of these factors is critically important in the field of dielectric measurement. For example, there are important differences between propagation in lossy materials versus propagation in lossless materials, such as dispersion, which becomes more prevalent as the material becomes lossy. As a result, the most suitable measurement method for a given situation may vary depending upon the configuration of the material.

2.4 Commonly-Used Methods

The following review gives an overview of the frequency and time-domain techniques used to characterize dielectric materials. It is not intended to be a complete summary of the methods used to characterize the electrical properties of materials. Instead, it highlights a number of widely-used methods and concepts, so the reader may become more familiar with the basic methods used to characterize dielectric materials. The advantages, disadvantages, and limitations of each of these methods will be compared to the methods proposed in this thesis.

Time-domain techniques are applicable to broadband measurements, but with relatively low resolution, while frequency-domain techniques are more applicable to narrowband situations, and can achieve much higher measurement resolution within these narrow frequency bands, especially as the frequency increases.

Frequency-domain analysis

By exciting the material under test with a steady-state input signal of known frequency, the steady-state response of the material to the excitation is observed. From this response, an algorithm is utilized to calculate the complex permittivity of the material.

Time-domain analysis

The material typically is excited by either a pulse or step of energy with a very short rise time. Using the modern techniques of time-domain reflectometry, the reflection from the sample is observed and sampled. By performing an inverse Fourier Transform on the received data, the frequency response is acquired. A solution algorithm is then run to determine the permittivity and dielectric loss tangent.

Although frequency and time-domain characterization techniques are both widely used, the methods used in this thesis rely solely upon frequency-domain analysis to determine the complex permittivity. In the future, a time-domain approach might be considered to not only provide verification of the frequency-domain techniques, but also possibly lead to better characterization of the errors given by the solution method.

The following list presents a small sample of some commonly-measured materials in the growing field of dielectric measurement.

- **Printed circuit board (PCB) substrates**. This is important to know for the purpose of circuit design, since the capacitance, characteristic impedance, and losses of traces are highly-dependent upon the complex permittivity of the circuit board.
- **Biological-tissue samples**. The state or health of tissue can be analyzed by determining its electrical properties.
- **Building materials**. The integrity of the material can be tested and determined by measuring the electrical properties.
- **Reflective or absorbing materials**. The design of these materials is greatly enhanced by knowing the dielectric properties.

2.4.1 Parallel-Plate Capacitor

Parallel-plate capacitor characterization methods are among the simplest, quickest procedures used for determining the dielectric constant of a material, and are also among the most accurate. The theory involved is extremely simple, as the capacitance C of a parallel-plate capacitor is found from [4] to be:

$$C = \frac{\varepsilon A}{d} \tag{2.8}$$

where

A = The surface area of the electrodes

ε = the complex permittivity of the material under test in between the electrodes

d = the separation of the plates

A sample is placed in between two electrodes as shown in Figure 2-3, and an LCR meter or low-frequency network analyzer is used to measure the capacitance and dissipation factor of the test fixture. Then, by rearranging (2.8), the complex permittivity is directly calculated. Capacitive methods are useful only at low frequencies, which typically range from fractions of a hertz up to 15MHz. As the frequency extends above this range, delays in the material and the possible existence of surface waves hinder the measurement to the point that the method eventually becomes unusable.

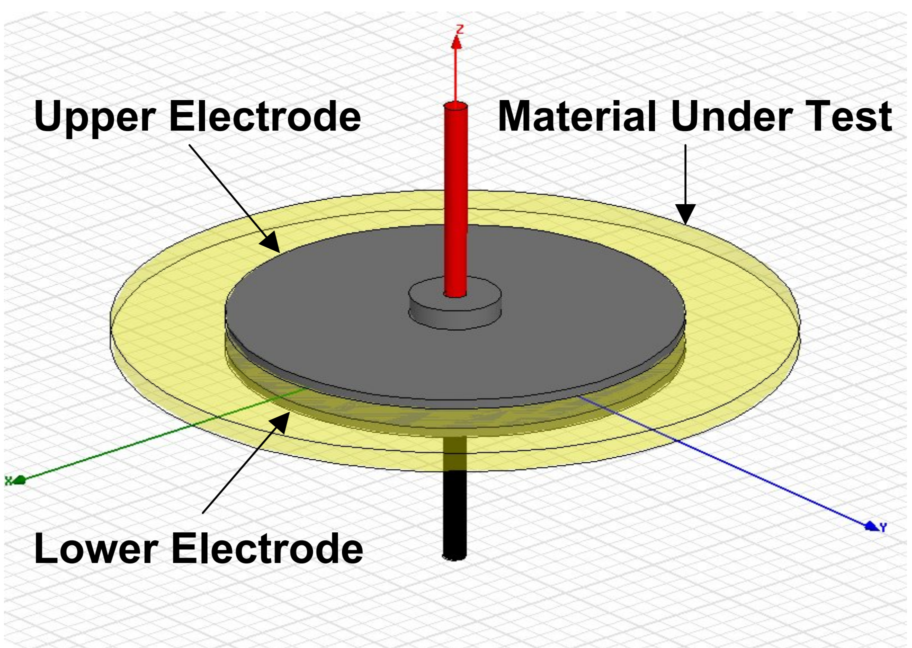

Figure 2-3. The unguarded parallel-plate capacitor configuration.

Two primary problems are encountered when using capacitive techniques. First, the electric field at the edge of the capacitor creates a fringing pattern, which makes the capacitance appear larger than it actually is. This fringing effect is countered either by introducing an approximate empirical area adjustment term to the parallel-plate capacitor equation or by adding guard rings to the capacitor fixture, as shown in Figure 2-4.

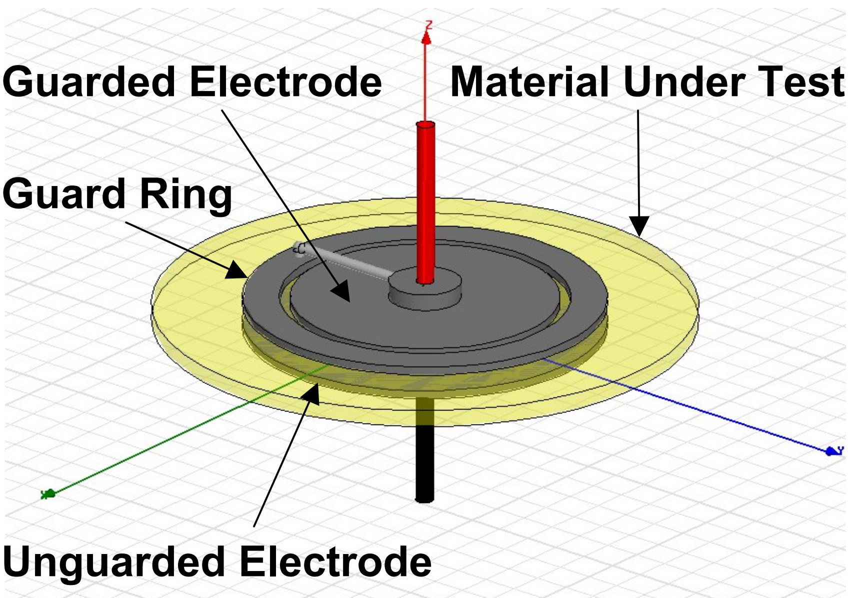

Figure 2-4. The guarded parallel-plate capacitor configuration. The capacitance between the guarded electrode and guard ring is negligible, since they are kept at the same voltage potential.

The second problem dealt with in using capacitive methods is the presence of air gaps, which can significantly influence the value of measured capacitance. Air gaps and at the electrode-material interface or between layered sheets of material have been shown to cause large errors in the measured capacitance [5]. Consideration must also be given to the diffusion that sometimes occurs when a material is brought into contact with metal.

2.4.2 Coaxial Cavity

Whenever a sample is required to be placed inside of a structure, regardless of whether it is coaxial or rectangular, problems can arise. First, the likelihood of having small air gaps between the sample and walls of the guide is increased. Even small pockets of air can have a significant effect on the measured value of complex permittivity. Second, unless extreme care is taken in the sample-preparation stage, the rough edges of the sample can scratch the interior of the sample holder, thus degrading its electrical performance. Since the sample holder is usually an expensive precision-machined component, this can be a significant problem. Lastly, the insertion of the sample into the line makes it difficult to know the exact reference plane of the sample, which can make calibration and the removal of systematic errors a problematic process.

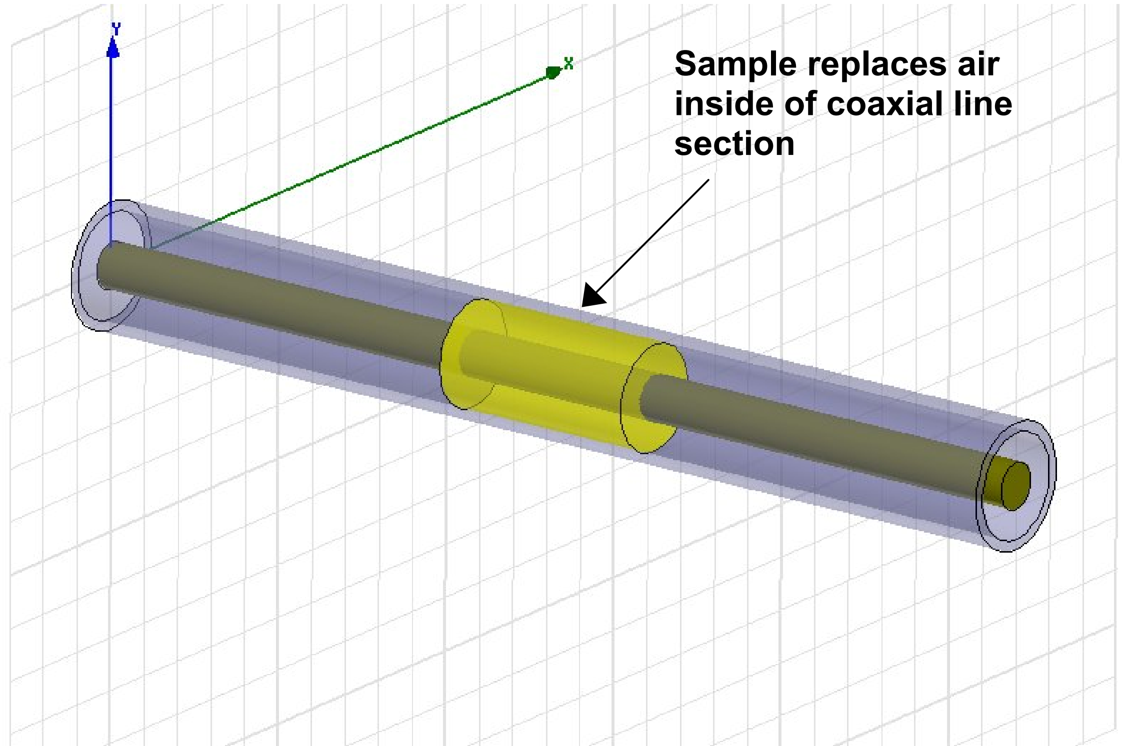

Figure 2-5. The coaxial line configuration.

In [6], Saed, Riad, and Elshabini-Riad present a pair of techniques that utilize a wide-band cavity mated to precision coaxial air lines. In each configuration, time-domain techniques were used to measure the S-parameters. Using the setup shown in Figure 2-6, the reflected and transmitted waves are sampled and then deconvolved [7] to obtain the reflection and transmission coefficients.

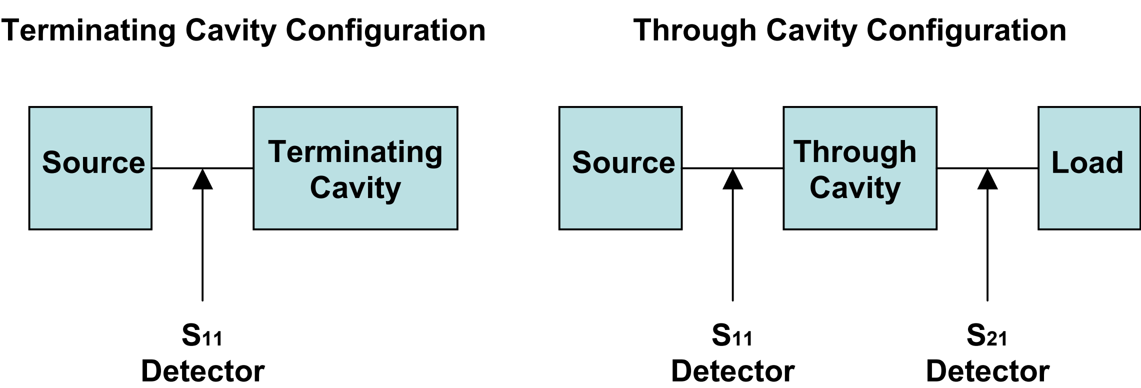

Figure 2-6. The coaxial line setup presented in [6]. Measurements may be taken in the time domain or the frequency domain.

2.4.2.1 The Terminating Cavity Configuration

In the terminating cavity configuration, the sample is directly adapted to the end of the air line. The measured reflection coefficient is used to compute the complex permittivity of the sample. To prepare the sample, it is first cut into a cylindrical shape. The cavity is then formed by depositing metal to the cylindrical sample to form the cavity walls and backing. This method is well-suited to precise dielectric characterization, since the metallization-process eliminates the presence of air gaps. Diffusion can still occur at the material-metal interface. Note that the center conductor of the air line does not continue through the sample, and the sample-containing cavity contains only the material under test (MUT).

The terminating cavity is effective for the measurement of all types of materials, including thick-film materials, which cannot support themselves freely. To prepare a sample of this type, the thick-film dielectric layer and surrounding metallization are printed on a ceramic substrate. Since the deposited metal isolates the thick-film layer, the substrate acts only as a physical support and has no role in the electrical performance of the cavity.

Due to the nature of electromagnetic waves in a cylindrical configuration, the cavity will resonate at the radial resonance frequency, which depends primarily upon the radius of the sample. The sample and cavity are usually made with a diameter small enough such that the resonance frequency falls well above the intended measurement frequency range.

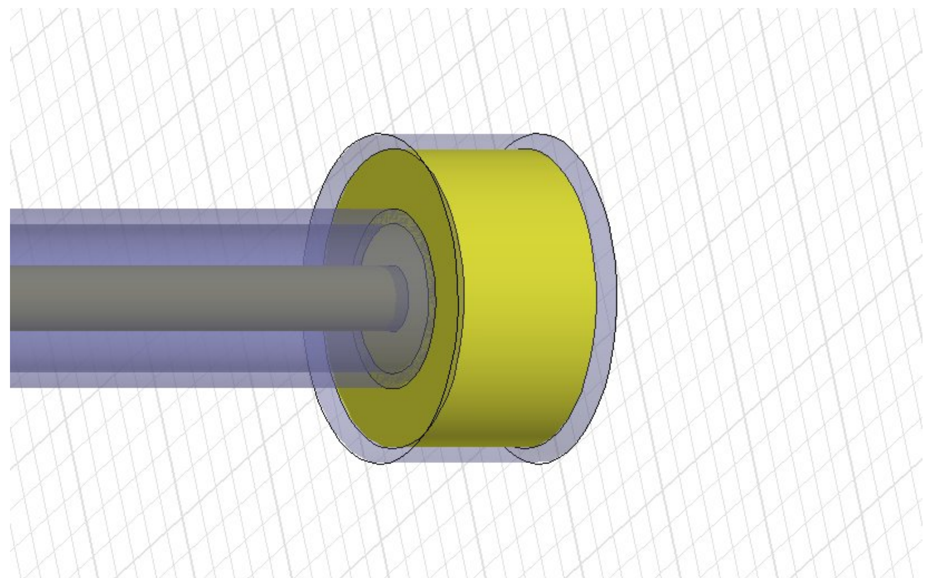

Figure 2-7. The coaxial terminating-cavity configuration.

To obtain the permittivity from the measured S-parameters, a relationship is made to link the theoretical and experimental results. This analysis is performed by carrying out a full-field analysis of the cavity structure using the method of moments [8]. As with most complex dielectric characterization problems, the solution is found by using an inverse-solution algorithm, which is performed by finding the complex permittivity of the sample given the measured scattering parameters. Since the equations are very difficult to solve analytically, the solution is obtained using a numerical solver with optimization techniques.

As the mathematical framework was already in place to create the inverse solution, a method was produced to determine the S-parameters given the complex permittivity and sample thickness. By conducting forward analysis of the solution, sensitivity analysis can be conducted, in which the sensitivity of the scattering parameters to variations in ε', ε'', sample thickness, and sample radius can be observed.

Since the phase of the reflection coefficient is highly sensitive to variations in the dielectric constant, the real part of the permittivity can be accurately predicted. The loss tangent of the sample is primarily dependent upon the magnitude of s_{11}, and is much more sensitive for high-loss materials. Therefore, extreme care must be taken when the loss of a low-less material is being measured.

The sample thickness is much more critical to the results than the diameter of the sample. However, errors due to variations in the sample thickness diminish as the frequency approaches the radial resonance frequency.

2.4.2.2 The Through-Cavity Configuration

In this configuration, the sample is placed between two precision air lines. As with the terminating cavity, this method is appealing due to the fact that the reference plane of the measurement is well known. The high-bandwidth capability of this configuration holds promise for the future, as characterization of materials in the millimeter wave region becomes of more interest.

As with the terminating cavity, the through cavity has a resonance frequency that is primarily influenced by the radius of the sample. Therefore, the sample should be made small enough that the radial resonance frequency falls outside of the measurement bandwidth.

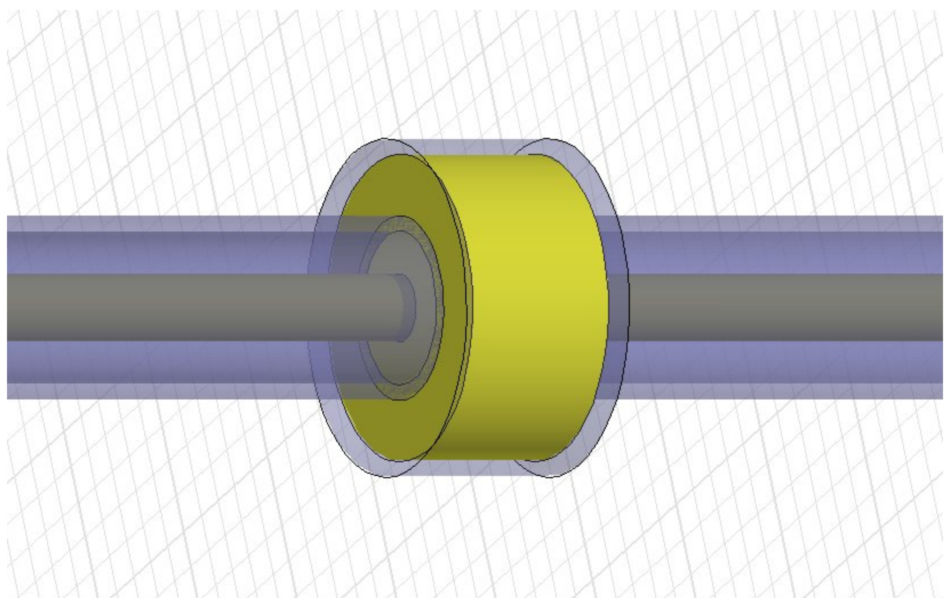

Figure 2-8. The coaxial through-cavity configuration.

Sensitivity analysis of the through-cavity configuration shows that the magnitude and phase of s_{11} and s_{21} change considerably as the thickness is varied. Therefore, the thickness of the sample must be precisely known in order to effectively estimate the

permittivity. The effect of variations in the other parameters, however, was found to be similar to that of the terminating cavity.

One advantage the through-cavity configuration has over the terminating cavity configuration is that two independent sets of data, s_{11} and s_{21}, are available to separately solve for the permittivity. They can be solved in parallel; then their solutions can be compared to analyze the validity of the solution, or they can both be combined into an optimization routine to obtain an optimal numerical solution.

2.4.3 Rectangular Metallic Waveguide

The waveguide is a particularly effective dielectric characterization method. The waveguide can be either rectangular or cylindrically-shaped, depending upon the specific methodology being used. Waveguide methods are generally categorized as transmission line methods, although the resonant behavior of a waveguide cavity can also be included in the dielectric measurement process.

Using traditional rectangular waveguide methods, only the dominant TE_{10} mode is assumed to propagate. Higher-order modes do typically exist at discontinuities of waveguide cross-sections, and evanescent waves are created near the material-air interface [9].

2.4.3.1 Sample-in-Waveguide

For the reflection and transmission coefficients s_{11} and s_{21}, if the waveguide conductivity is suitably high, only the phase of s_{11} is significantly affected by the exact location of the sample. This allows for computation of the dielectric permittivity even if the exact location of the sample within the guide is known. The thickness of the sample, however, is critically important to the computed permittivity and is usually one of the largest contributors to the measurement error.

Olmi, Tedesco, Riminesi and Ignesti [10] have presented a rectangular waveguide method that is independent of the sample thickness. The thickness of the sample is treated as an unknown and is solved for in the solution process. To allow for easy insertion and removal of the sample, a narrow slot is cut into the narrow wall of the waveguide. The removal of the narrow wall was chosen over the broad wall, since the

electric field in the TE_{10} mode of operation is primarily present along the middle of the broad wall of the waveguide. This does lead, however, to a discontinuity in the electrical currents along the waveguide wall. The extra length of waveguide is added to filter out the effects of higher-order evanescent modes.

The reflection coefficient is first measured with a short-circuit termination, then with a broadband matched termination. Using a method proposed in [11], the following equation can be used to describe the theoretical reflection coefficient with a broadband matching load:

$$\Gamma_b(\varepsilon,d)=\frac{k_{z0}(k_{z\varepsilon}+jk_{z0}\tan k_{z\varepsilon}d)-k_{z\varepsilon}(k_{z0}+jk_{z\varepsilon}\tan k_{z0}d)}{k_{z0}(k_{z\varepsilon}+jk_{z0}\tan k_{z\varepsilon}d)+k_{z\varepsilon}(k_{z0}+jk_{z\varepsilon}\tan k_{z0}d)} \tag{2.9}$$

where k_{z0} is the propagation constant in the air-filled waveguide and

$$k_{z\varepsilon}=\sqrt{\varepsilon k_0^{\,2}-k_c^{\,2}} \tag{2.10}$$

is the complex propagation constant in the region containing the unknown dielectric material.

The short-circuit reflection coefficient is described by

$$\Gamma_s(\varepsilon,d)=\frac{k_{z0}(jk_{z\varepsilon}\tan k_{z0}D+jk_{z0}\tan k_{z\varepsilon}d)-k_{z\varepsilon}(k_{z0}-k_{z\varepsilon}\tan k_{z0}D\tan k_{z\varepsilon}d)}{k_{z0}(jk_{z\varepsilon}\tan k_{z0}D+jk_{z0}\tan k_{z\varepsilon}d)+k_{z\varepsilon}(k_{z0}-k_{z\varepsilon}\tan k_{z0}D\tan k_{z\varepsilon}d)} \tag{2.11}$$

where D is the length of the short-circuited waveguide. Each of the above equations can be solved numerically for ε, but uncertainty in the material thickness produces large errors in both the dielectric constant and loss tangent of the material under test.

When the measured and theoretical reflection coefficients for each measurement are equated, the solution set is multi-valued, since a change in thickness can be balanced out by a corresponding change in the permittivity. Therefore, (2.9) and (2.11) are combined using a genetic algorithm to find a unique intersection, which is taken as the solution [12], [13].

2.4.3.2 Slotted Waveguide

Another waveguide method useful for thin samples is the slot-in-waveguide method. The sample is inserted into a narrow slot cut in the broadside wall of the rectangular guide as illustrated in Figure 2-9. Since the material sample is oriented parallel to the electric field, the error due to air gap effects is minimal.

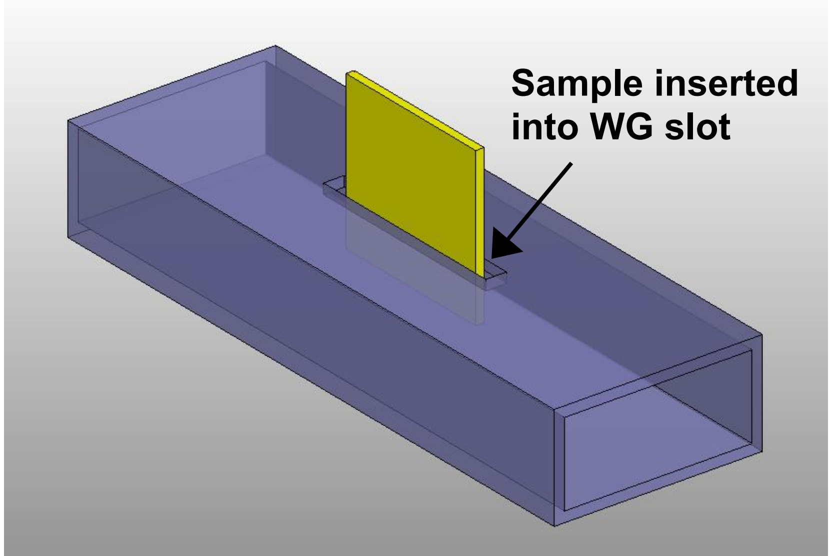

Figure 2-9. The slotted waveguide configuration.

An obvious problem with this method is radiation leakage, which can become a problem if the slot is milled too wide. Therefore, the gap should be kept as narrow as possible. The method is useful for both low and high-loss materials, and is very appealing since the measurement is non-destructive and can be quickly performed. The error is typically higher, however, than other comparable high-precision techniques, such as cavity perturbation.

2.4.4 Resonators

Despite the continual advent of new transmission methods, resonator methods have continued to remain popular, due to their superior sensitivity to variations in the material under test [14]. The method is also appealing, since very small samples can be precisely characterized.

All resonator methods rely on the fact that a structure will resonate at a certain frequency, which shifts when a material under test is added to the configuration. As the material is inserted, the sharpness of the resonance, commonly known as the quality factor Q, can be related to the dielectric loss.

$$Q = \omega \frac{stored_energy}{dissipated_power} = \omega \frac{W_e + W_m}{P_d} \tag{2.12}$$

Where

W_e = Stored electric energy
W_e = Stored magnetic energy
P_d = Dissipated power

The total dissipated power is found by adding all of the power that is dissipated along the walls of the resonator, with consideration given to losses in the microwave source and measurement probes.

The coupled-stripline resonator is one of the most commonly used configurations in the measurement of dielectric substrates. The resonator circuits can be fabricated using standard circuit board fabrication techniques, and results of high-accuracy for the complex permittivity ε^* can be consistently obtained. Although the production of stripline is more involved than for microstrip, it is generally preferred for dielectric characterization, since the electromagnetic fields have no edge effects and are not free to radiate, and the loss tangent can more accurately be estimated. As with most resonators, the dielectric resonator allows material property determination only at the resonance frequencies, rather over a continuous range of frequencies.

Line resonators and ring resonators are two of the most common resonator types built in the stripline geometry, and both have distinct advantages and disadvantages. They both work under the premise that a suspended PCB trace resonates when excited by frequencies with a corresponding guided wavelength that is an integral multiple of the

length of the resonator strip. Then, by observing the resonance frequency and quality factor of that resonance, the complex permittivity is calculated.

The coupling gap, across which the waves couple from the feeding circuit to the resonator, presents problems due to the fringing of fields across the gap. This creates an uncertainty with regard to the effective length of the resonator section. The main design complication lies in deciding the proper width of the gap. Creating a gap that is too wide prevents a sufficient amount of signal from being coupled to the resonator, making it difficult to effectively view the resonances. A gap that is too narrow, however, causes a loading effect on the resonator, which reduces the quality (Q) factor of the resonances.

Su, Riad, and Elshabini-Riad [15] point out many of the shortcomings with the stripline-resonator geometry and present ways to overcome the problems. Since the response of the resonator is highly sensitive to the physical dimensions, the geometry must be known in painstaking detail to effectively estimate the material properties. Errors can sometimes be caused due to etching limitations and the imprecise measurement of fine lines.

Stripline Line Resonator

A dielectric line resonator is shown in Figure 2-10. It consists of a suspended resonator placed between two feed lines, and is capable of material characterization at very high frequencies into the millimeter-wave range.

Since waves propagate in the TEM mode on a stripline transmission line, the guided wavelength λ_g is related to the free-space wavelength λ_o as follows:

$$\lambda_g = \frac{\lambda_o}{\sqrt{\varepsilon_r}} \tag{2.13}$$

When the input frequency approaches a value at which the length of the line resonator is an integer multiple of $\lambda_g/2$, the line will resonate.

$$l = n\frac{\lambda_g}{2} \tag{2.14}$$

where n = 1, 2, 3, …

At first glance, the method appears simple, but the fringing fields at the end of each line create ambiguity as to the exact value of the length. Since the fringing fields at the discontinuity increase the effective length of the resonator section and throw off the calculated permittivity, their effects must be accounted for. The l is replaced by the effective length l' in (2.14) to account for this error.

$$l' = l + 2\Delta l \tag{2.15}$$

The modified length, l', is used to represent the effective length of the resonator due to the field extension on each end of the resonator. It is found by modeling the coupling gap as a pi-network of capacitances, from which the incremental length Δl is computed. It is seen from (2.15) that the error due to the fringing fields can be reduced by making the length l very long in comparison to Δl, which makes l' less sensitive to variations in the gap configuration.

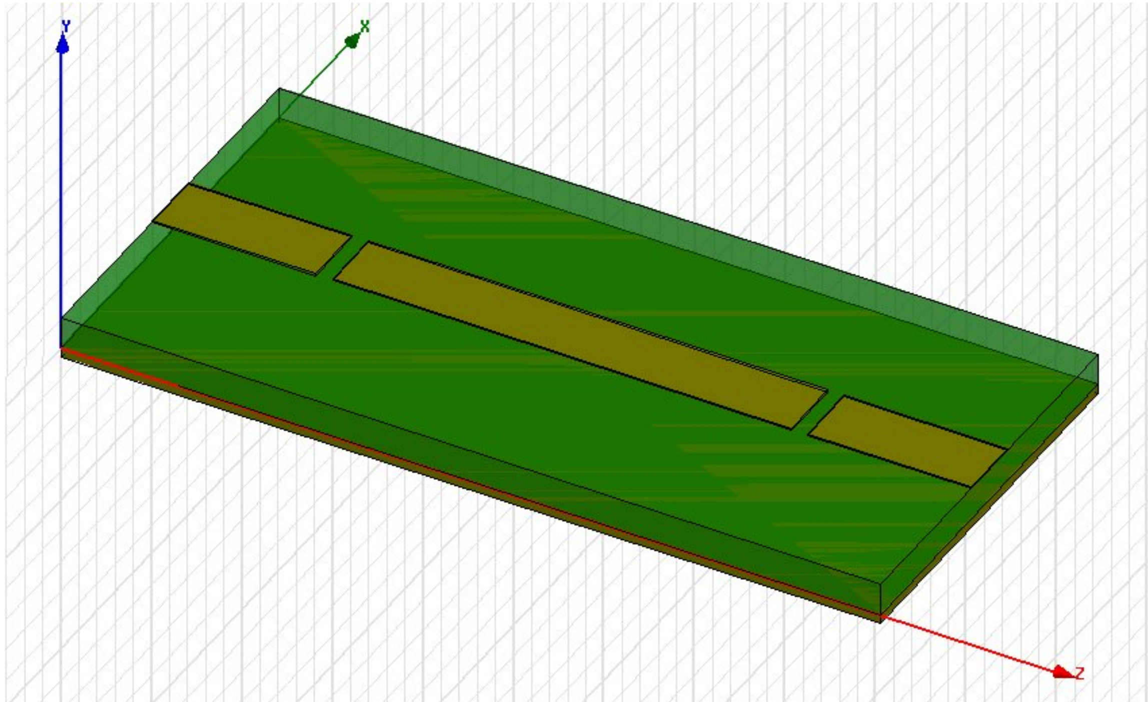

Figure 2-10. The dielectric stripline line resonator. The upper substrate and ground plane are not shown in the diagram for improved visibility of the traces.

The overall quality factor, Q_o, of the resonator is solved by the following relation:

$$\frac{1}{Q_o} = \frac{1}{Q_c} + \frac{1}{Q_d} + \frac{1}{Q_r} \tag{2.16}$$

Q_c is related to losses in the conductors along the line, Q_d is related to losses in the dielectric material under test, while Q_r is related to radiation losses suffered. Since the stripline geometry prevents losses due to radiation, (2.16) simplifies to

$$\frac{1}{Q_o} = \frac{1}{Q_c} + \frac{1}{Q_d} \tag{2.17}$$

The loss tangent can be related to the dielectric quality factor as

$$\tan\delta = \frac{1}{Q_d} \tag{2.18}$$

In [15], an equation was developed to relate the conductor loss term to a function, *g(b,t,w)*, which is determined by the physical dimensions of the structure, and is given by

$$\frac{1}{Q_o} = \frac{1.5911}{\sqrt{\sigma f}} g(b,t,w) + \tan\delta \tag{2.19}$$

with *tan(δ)* as the only unknown, the loss of the material is calculated.

Stripline Ring Resonator

A ring resonator is very similar in operation to the straight-line resonator, but the geometry is changed by forming the stripline resonator into the shape of an isolated circle. The signal is coupled to the resonator in the same way as it is with the straight-line resonator, but the ring resonator has an inherent advantage over the line resonator, in that the circular resonator has no edge effects to consider. A PCD layout of a ring resonator is shown in Figure 2-11.

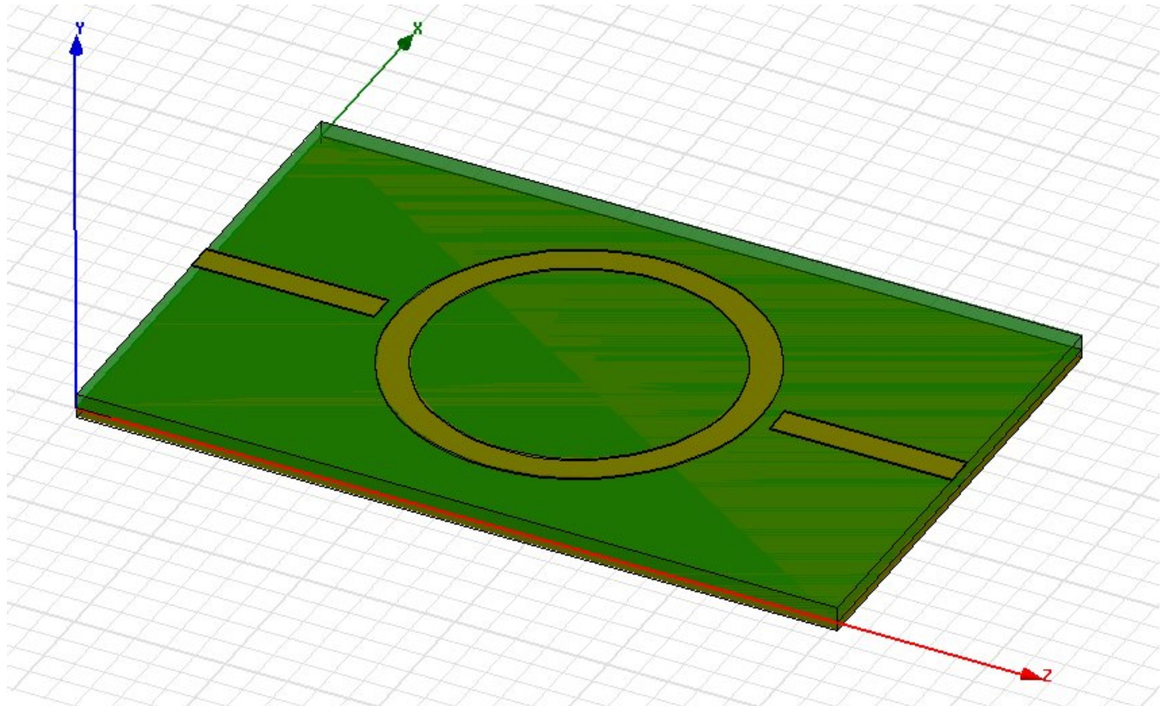

Figure 2-11. The dielectric stripline ring resonator. The upper substrate and ground plane are not shown in the diagram for improved visibility of the traces.

The ring resonates at frequencies which have a value of λ_g equal to the circumference C of the circle. This relation is expressed as

$$C = n\lambda_g \tag{2.20}$$

where n = 1, 2, 3, …

The main cause of uncertainty in the ring resonator is in the determination of the circumference of the resonator. Since the circular trace is of finite width, the circumference of the circle varies as the diameter is changed. The mean radius of the circle is not always the most suitable choice. This can become a significant problem when using low characteristic impedance lines, which are inherently wide and have an unclearly-defined circumference.

To overcome these effects, a magnetic wall model is used [15]. The model, which takes the curvature effect into account, models the resonator as a resonating cavity with electric walls on the top and bottom, and magnetic walls on the sides. The fields in

the modeled cavity region can then be computed, from which the relative permittivity of the substrate material can be derived.

Cavity Resonators

Cavity perturbation can be used to measure complex material properties by observing the changes in cavity resonances and Q-factor due to the insertion and removal of the material under test. Due to the strong interactions between cavity fields and an inserted sample, resonant cavity techniques such as perturbation typically yield the lowest error of any dielectric characterization methods. Using perturbation, the cavity fields are perturbed by a small sample small enough that the disruption of the electromagnetic fields within the cavity is negligible.

Perhaps the most commonly used technique relies on a cylindrical cavity resonating in TM_{0n0} modes. This setup usually requires the sample to be shaped into the form of a thin cylindrical rod, which is placed along the coaxial axis of the cavity. The sample is placed at the post of the reentrant cavity such that it is aligned in parallel with the electric field.

The change of the complex eigen frequency $\Delta \bar{f}$ due to the insertion of a material of volume V_s is [16]

$$\frac{\Delta \bar{f}}{f_o} = -\frac{\int_{Vs} (\Delta\varepsilon E \cdot E_o^* + \Delta\mu H \cdot H_o^*) d\tau}{\int_{Vc} (\Delta\varepsilon E \cdot E_o^* + \mu H \cdot H_o^*) d\tau} \tag{2.21}$$

Where E and H represent the fields in the cavity with the sample, while E_o and H_o represent the fields in the cavity without the sample. If we assume the material to be nonmagnetic, the change in permeability is zero, and the second term in the numerator disappears. Since the sample size is small, E and H are approximated by setting them equal to E_o and H_o**,** respectively, in the region containing the sample. If we write the value of E inside the sample as E_{int}, we can write [16]:

$$\frac{\Delta \overline{f}}{f_o} = -\frac{\int_{Vs} (\Delta\varepsilon E_{\text{int}} \cdot E_o^*) d\tau}{\int_{Vc} \varepsilon |E_o|^2 d\tau} \tag{2.22}$$

The change in the complex frequency is related to the shift in resonance frequency and Q-factor by the relation

$$\frac{\Delta \overline{f}}{f_o} = \frac{\Delta f}{f_o} + j\frac{1}{2}\left(\frac{1}{Q} - \frac{1}{Q_o}\right) \tag{2.23}$$

where Q and Q_o are the resonance quality factors with and without the sample, respectively. Plugging in the complex value of permittivity, we obtain the relation

$$\frac{\Delta \overline{f}}{f_o} \cong -\frac{\int_{Vs} (\varepsilon' - 1 - j\varepsilon'') E_{\text{int}} \cdot E_o^*) d\tau}{2\int_{Vc} |E_o|^2 \, d\tau} = \frac{\int_{Vs} (\varepsilon' - 1) E_{\text{int}} \cdot E_o^*) d\tau}{2\int_{Vc} |E_o|^2 \, d\tau} + j\frac{\int_{Vs} \varepsilon'' E_{\text{int}} \cdot E_o^*) d\tau}{2\int_{Vc} |E_o|^2 \, d\tau} \tag{2.24}$$

Comparing (2.23) and (2.24), an expression is obtained for the real and imaginary parts of the complex permittivity.

$$\varepsilon' \,\square\, 1 - 2C_{conv} \frac{\Delta f}{f_o} \tag{2.25}$$

and

$$\varepsilon'' \approx C_{conv}\left(\frac{1}{Q}-\frac{1}{Q_o}\right) \tag{2.26}$$

where [16]

$$C_{conv} = \frac{\int_{Vc} |E_o|^2 d\tau}{\int_{Vs} \mathbf{E}_{\text{int}} \cdot \mathbf{E}_o^* d\tau} \tag{2.27}$$

C_{conv} can then be computed for the given geometry. If the sample shape is wisely chosen, the solution can be greatly simplified. For a circular cavity of radius *a* resonating in the TM_{0n0} mode, with a cylinder-shaped rod of radius *b*, and a cavity of height *d*, C_{conv} is then solved in [17] as

$$C_{conv} = \frac{\int_0^a J_o^2(k_n r) r dr}{\int_0^b J_o^2(k_n r) r dr} \tag{2.28}$$

where, if x_{on} is the nth zero of the Bessel function J_o,

$$f_n = \frac{c x_{on}}{2\pi a} \tag{2.29}$$

$$k_n = 2\pi f_n \sqrt{\varepsilon_o \mu_o} \tag{2.30}$$

The above development is not an exact solution, since the field within the sample has been assumed to be the same as without the sample and distributed uniformly throughout the sample.

The perturbation method is a very promising method, since samples of any size or shape can be measured, as long as the fields can be theoretically derived in the region of the sample. As the sample size deviates from standard geometries, however, the complexity of the electromagnetic fields greatly increases and the solution is much more involved.

The traditional perturbation method is not without drawbacks, however. The permittivity calculation is highly sensitive to the sample size, volume and location within the cavity, so any measurement errors usually translate directly to the value of measured permittivity and permeability. One other thing to consider is that the results and error get significantly worse as the relative permittivity of the sample increases. Also, for any sample characterization, two measurements must be taken on the sample. Finally, depending on the exact method being used, the sample must sometimes be shaped into a size that is difficult for the given material type being measured.

Several variations on the classic perturbation techniques have been presented in the literature to overcome some of the existing difficulties. Parkash, Vaid and Mansingh [18] have generalized the theoretical development involving the insertion of dielectric rods into cavities operating in the TM_{010} mode to allow cylindrically-shaped samples with a length less than that of the cavity height. Sen, Saha, and Nag [19] developed a new perturbation technique for low-loss dielectrics in which (1) the sample area is not used in the calculations, (2) only the frequency shift of two samples of the same area and differing thickness is relevant to the solution, and (3) the measurement system does not need to be calibrated with a known dielectric.

2.4.5 Open-Ended Coaxial Probe

The open-ended coaxial probe has been widely researched over the years as a way to effectively and quickly characterize material properties. It is a very appealing characterization method, since the setup time for a measurement is very short and the measurement is non-destructive to the material. It has also recently received special

interest due to the capability of conducting measurements in-vivo [20]. The probe is nothing more than a precision coaxial line that opens into a flanged open-circuit. To measure a material, the probe is placed flush on the surface of the MUT (see Figure 2-12) and the reflection coefficient is measured.

The coaxial line is operated in the TEM mode, making it suitable as a broadband characterization mechanism. The fields at the end of the probe, however, typically consist of TEM and higher order evanescent modes. The fields at end of the coaxial probe fringe into the sample, creating an effect which is a similar to the fringing at the edge of a parallel plate capacitor. Since the electric field has components in the ρ and z directions, the air gap between the probe and the sample becomes critically important to the measured value of permittivity. It is desired to have the smallest possible air gap between the probe and MUT. For this reason, the method is typically preferred for the measurement of liquids and semi-solid materials, rather than solid materials. The method can also be applied to solid materials, but the surface must be extremely smooth and flat to produce accurate results.

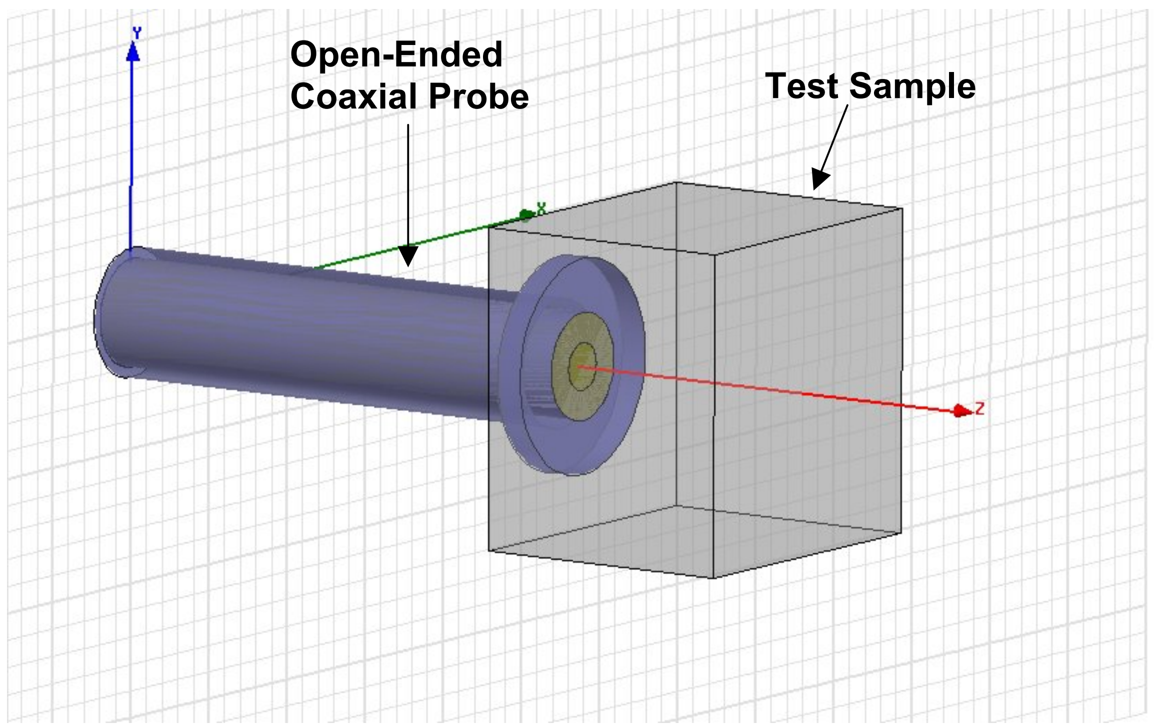

Figure 2-12. The open-ended coaxial probe.

Baker-Jarvis and Janezic [21] present the full-wave solution to this problem with special attention given to the influence that the air gap has on dielectric measurement. This is an important topic, since the air gap is the greatest cause of error in the open-ended coaxial configuration. The air gap may even be desirable in some situations, since non-contact testing may be necessary. The following three cases are presented in [21]:

(1) The sample infinitely extends in the axial direction

(2) The sample is backed by a well-characterized material

(3) The sample is backed by a short-circuit termination

All of the analysis is performed under the assumption that the sample is infinitely large in the radial direction. The air gap is included in all of the analysis, but by setting the gap size to zero, Baker-Jarvis' and Janezic's results show very good numerical agreement with other published results. The field penetration into the material and resulting precision increase as the coaxial probe is made larger and also as the measurement frequency increases.

In 1992, HP introduced a commercial version of the open-ended probe, the HP 85070M. The small probe was useful for quick measurements, but suffered greatly from air gap effects. Since the fringing fields do not penetrate very far into the sample at lower frequencies and the probe is relatively small, the sensitivity of the reflection coefficient to changes in ε' is small at lower frequencies, which leads to a sub-5GHz error exceeding 10% for some values of permittivity. As a result, the error remains fairly large until the frequency is high enough to cause sufficient penetration into the sample.

2.4.6 Free Space Methods

Free-space dielectric characterization methods are highly appealing for many situations, since they are non-destructive, non-contact methods that can be used for broadband measurements from 50MHz-30GHz [3]. Free space methods are some of the best methods for low-loss materials, and due to the non-contact nature of the measurement process, free-space techniques can also be conducted at much higher temperatures than other comparable methods. The theoretical analysis is generally similar to that of transmission methods, and is usually greatly simplified by making the assumption that the radiated wave front is in the form of a plane wave.

To measure the complex permittivity of a sample in a typical free-space setup, a sheet of the material under test is mounted directly between two directional antennas, such as the waveguide horn antenna, as shown in Figure 2-13, and the experimental transmission and reflection coefficients are used to solve for the material properties. The sample mounting device is usually constructed of foam, or another material that has a permittivity close to that of air [3]. The quality of the measurement is enhanced by placing absorptive panels around the room in which the material is measured.

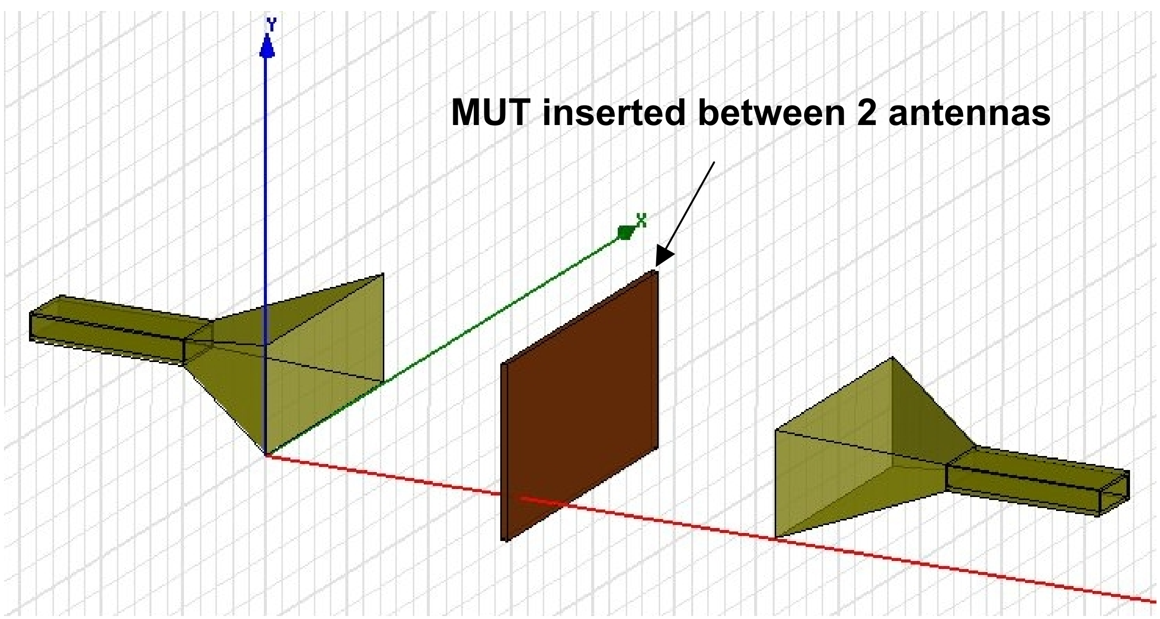

Figure 2-13. The free-space configuration.

Two standard calibration techniques, TRM (Thru-Reflect-Match) and TRL (Thru-Reflect-Line), each suffer from drawbacks in the calibration of a free-space setup. In a TRM calibration, it is very difficult to obtain a broadband match standard for use in the calibration procedure. Imperfections in the broadband absorption lead to the appearance of undesirable residual errors in later measurements. A standard TRL calibration in the free-space setup is also troublesome, since one of the two antennas must be moved for the reflection and line standard measurements. Expensive positioning equipment is needed to precisely move the antenna, and even still, it is difficult to completely eliminate the error due to imperfect positioning.

As a result, a popular calibration procedure used for this type of measurement, GRL, or "Gate-Reflect-Line", is commonly used to simplify the calibration process. GRL, which is closely related to the widely-used TRL technique, is a hybrid time and frequency-domain calibration [22] that does not require either antenna to be repositioned. Using a gated time-domain measurement, the s_{11} of the GRL error adapter can be found, eliminating the need to move either antenna [22]. This is done by applying a time-domain gate to only the portion of the reflected waveform pertaining to the transmitting antenna. Then, by measuring the reflection and line standards in the frequency-domain, all of the terms in the GRL error adapter are solved for and the calibrated reference plane is moved to the plane of the material under test.

Free-space methods are highly effective, but do have a set of drawbacks. Using this method, it is sometimes difficult to clearly determine the loss tangent of the material, since it is difficult to determine whether loss is the result of radiation or loss within the sample. Also, when free-space methods are used, the problem becomes essentially unbounded, multiple reflections become a large problem, and diffraction from the edge of the sample can all lead to extra loss and ambiguity [23] .

The measurement usually takes place within a small area to avoid excessive radiation, but it also takes a significant distance for the waves to become plane waves. This can be a problem, since all of the theoretical development used to determine the complex permittivity is conducted under the assumption that the waves are propagating as plane waves. As the frequency becomes lower, the distance from the antennae to the launcher must increase, which leads to larger required sample sizes that are sometimes troublesome to fabricate.

2.5 ASTM Standards

Over time, specific methods have gained recognition as being particularly suitable for certain types of thin-sample measurements. These have been recognized as standards by ASTM (American Society of Testing and Materials [24]. This list was released in 1990, however, and does not include some of the more recently developed methods.

Chapter 3
Capacitor Dielectric Characterization

3.1 Introduction

The parallel-plate capacitor technique is a simple, effective method of characterizing the properties of dielectric materials at low frequencies. Even though a material may not be intended for use at low frequencies, the capacitor technique is a highly useful way to establish baseline values for the materials, which can then be compared to results obtained from other characterization methods. It is a simple technique, with relatively low error, and if a good match between methods is achieved in the overlapping frequencies of differing material measurement methods, an added level of confidence is achieved.

3.2 Overview of Capacitance

Before proceeding, it is helpful to understand the basic idea of capacitance. When any two conductors are separated in space by a finite distance, a capacitance is formed between the two structures [4]. The exact value of that capacitance C is determined by the material in the region containing the electric field linking the two conductors, and is given by the following relationship:

$$C = \frac{Q}{V} \tag{3.1}$$

where V is the voltage potential between the two conductors with charge $+Q$ and $-Q$. Therefore, if the capacitance of a structure, as well as the theoretical relation between the capacitance and the complex permittivity, are well-known, then the complex material properties can be explicitly calculated. Note that the capacitance is independent of the electric field.

Out of all capacitive structures, the most commonly-used configuration for dielectric measurement is the parallel-plate capacitor. The parallel-plate geometry is

formed by placing a dielectric constant between two parallel-situated conducting plates, and is typically selected for the following reasons:

- The theoretical capacitance formula is simple to derive and understand compared to other capacitive structures
- High capacitances values can be achieved, which diminishes the effect of measurement errors
- The structure is easily constructed
- For this geometry, guard electrodes are effective in the elimination of stray and fringing capacitances

The underlying theory for the parallel-capacitor is demonstrated by deriving the capacitance of a general parallel-plate capacitor. The basic parallel-plate capacitor is shown in Figure 3-1. The bottom plate is situated in the *x*-*y* plane at z=0 and contains a charge $-Q$, while the top plate is situated in the same plane offset by $z=d$ and contains the same amount of charge with the opposite sign $+Q$ [4]. Each of the two conductors is assumed to be equipotential with $\rho_s = Q/A$. The electric field is therefore directed in the downward direction and is described in rectangular coordinates as

$$\mathbf{E} = -\hat{\mathbf{z}}E \tag{3.2}$$

In reality, there will be some fringing of the electric field at the edge of the conductor plates, but these effects are small as long as the area of the plates remains much larger than the separation between them [4]. The fringing is ignored for this derivation and will be addressed later.

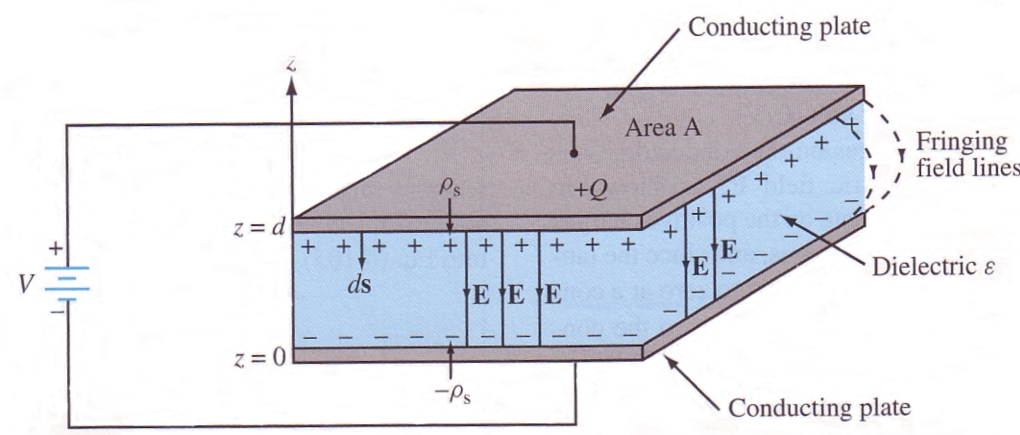

Figure 3-1. The parallel-plate capacitor configuration.

Maxwell's equations require that the electric field at a conductor's boundary is only situated in the direction normal to the boundary, while the tangential component is zero. The magnitude of the normal E-field component is given by

$$E_n = \hat{n} \cdot E = \frac{\rho_s}{\varepsilon} = \frac{Q}{\varepsilon A} \tag{3.3}$$

In general, the voltage potential between two conductors is found by integrating the field between them.

$$V = V_{12} = -\int_{P_2}^{P_1} E \cdot dl \tag{3.4}$$

The voltage difference between the plates can therefore be found as

$$V = -\int_0^d E \cdot dl = -\int_0^d (-\hat{z}E) \cdot \hat{z}dz = Ed \tag{3.5}$$

Going back to the definition of capacitance, and substituting (3.5) into (3.3), the capacitance is found [4] as

$$C = \frac{Q}{V} = \frac{Q}{Ed} = \frac{\varepsilon A}{d} \tag{3.6}$$

By re-arranging (3.6), the permittivity of the medium between the plates can be solved for.

$$\varepsilon = \frac{Cd}{A} \tag{3.7}$$

3.3 The Guarded Electrode

It is clearly seen from the preceding analysis that if the capacitance of a structure is well-known and the physical geometry is carefully measured, the permittivity can also be solved for. While the previously mentioned fringing fields may be neglected for some engineering applications, their effects upon the permittivity solution are too large to ignore in this case. The fringing fields have the effect of increasing the effective area of the plates, thus making the permittivity appear small than it actually is. Since the dielectric constant is directly linked to the area, any ambiguity in the area translates directly to ambiguity in the determination of the dielectric constant.

This dilemma is overcome by adding a guard ring to the capacitor structure, as shown in Figure 3-2. By keeping the guard ring at the same potential as the guarded electrode, but not allowing any of the measurement current to flow through the guard ring by connecting it to the shield, the capacitance due to the fringing fields is removed from the measurement [25], and (3.6) becomes more suitable since the assumptions are better satisfied.

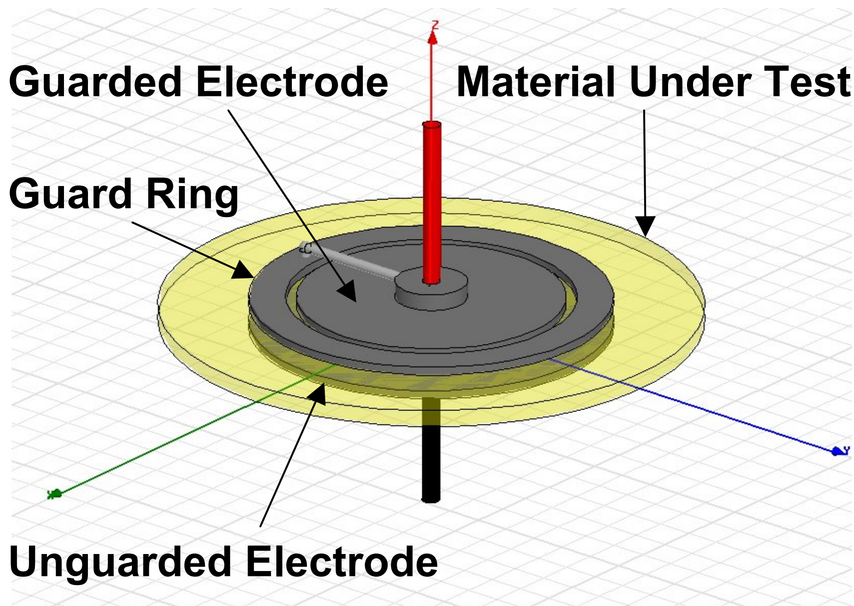

Figure 3-2. The guarded parallel-plate capacitor configuration.

The guard ring configuration is allowed by using the four-terminal pair measurement configuration. As Figure 3-3 shows, the four terminals are designated as High Current (H_{CUR}), High Potential (H_{POT}), Low Current (L_{CUR}), and Low Potential (L_{POT}). The two H terminals, as well as the two L terminals, are connected together, while the outer shield of all four terminals is connected together. The current terminals force current through the unknown impedance, while the potential terminals detect the voltage drop across the same quantity [26]. The ratio of the two is then taken to give the unknown impedance.

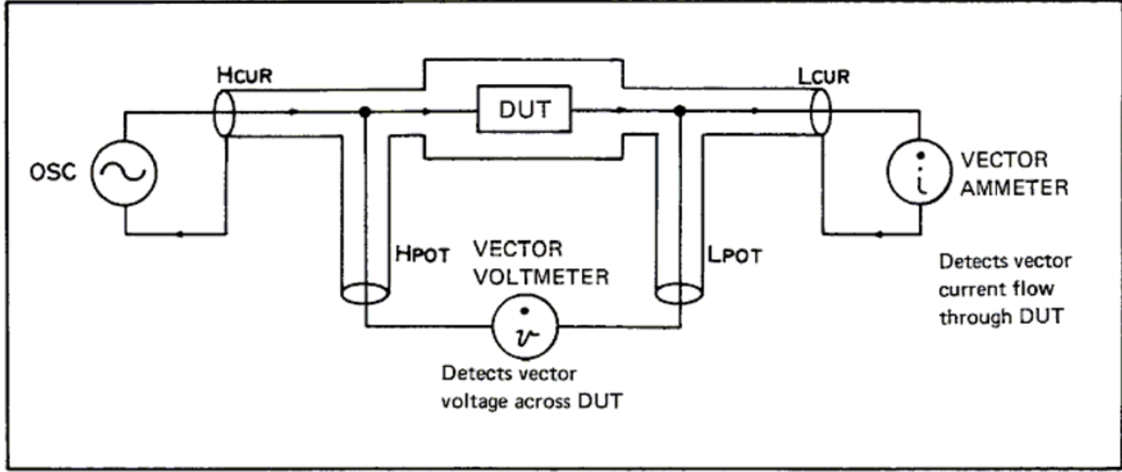

Figure 3-3. The four-terminal pair measurement architecture [26]. Copyright 2000 by Agilent Technologies. Reproduced with permission.

The four-terminal pair is particularly effective for high-frequency impedance measurements, where stray capacitances and residual impedances in the test leads can adversely affect the results. The distinguishing feature of the four-terminal pair configuration is that the outer shield carries the return current for the measurement signal. Since the same current flows in opposite direction through the center conductor and outer shield of each test lead, the external magnetic fields cancel out, vastly reducing the presence of any self or mutual-inductance [26].

In the 4192A LF impedance analyzer, the shield potential is held close to that of the low potential terminal. This allows the guard ring to be connected to the shield terminal, with its potential the same as that of the guarded electrode, but not to the L_{CUR} terminal. Since there is no measurement current flowing through the guard ring, its capacitance is not included in the overall measured capacitance.

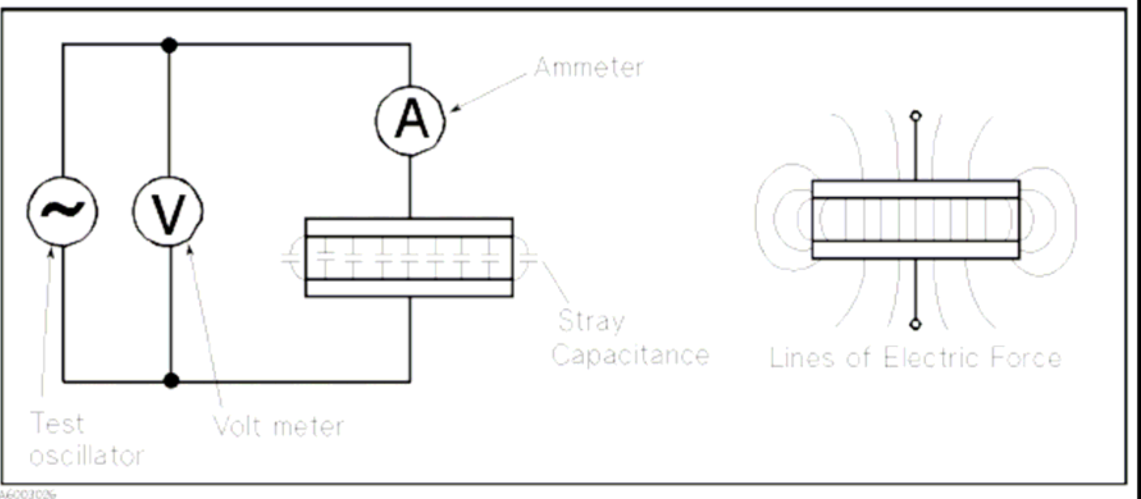

Figure 3-4. Unguarded parallel-plate capacitor configuration [25]. The fringing electric field at the edge of the capacitor creates ambiguity as to the effective area of the capacitor plates. Copyright 2000 by Agilent Technologies. Reproduced with permission.

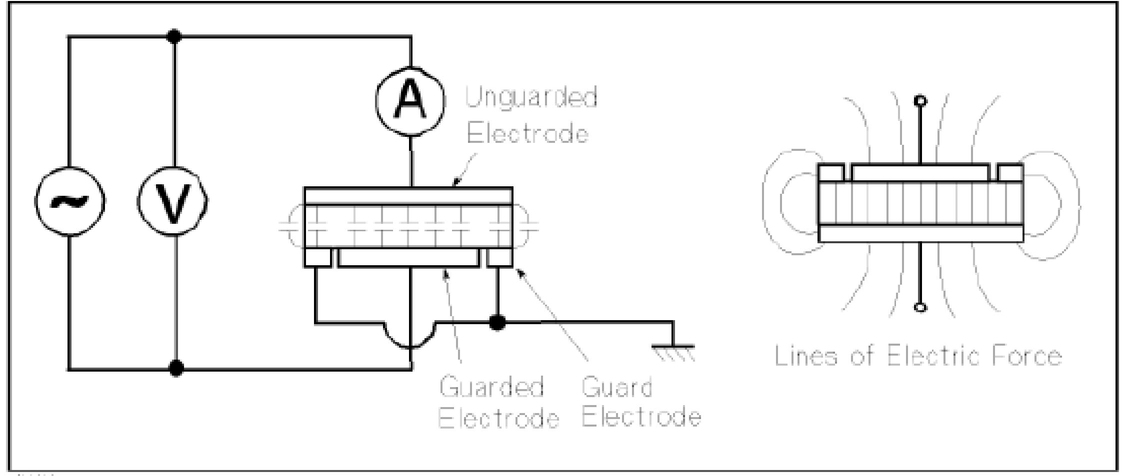

Figure 3-5. Guarded parallel-plate capacitor configuration [25]. The stray capacitance due to the fringing electric field is eliminated by the guard ring. Copyright 2000 by Agilent Technologies. Reproduced with permission.

3.4 Sample Measurement

For this thesis, the HP 4192A Low Frequency Impedance Analyzer and HP 16451B dielectric capacitor test fixture have been used to conduct the measurement of a 34-mil thick Teflon sample. Using the previously outlined method, the capacitance is measured, then used to solve for the unknown dielectric constant of the material. The dissipation factor D is read directly from the 4192A Analyzer, and is equal to the unknown *tan(δ)* of the material.

Figure 3-6. The HP4192A LF impedance analyzer.

Figure 3-7. The HP16451B dielectric test fixture. The guarded electrode configuration greatly reduces the fringing of the electric field at the edge of the parallel-plate structure.

The dimensions of the guarded electrode structure used are given in Figure 3-8. The large 38mm diameter of the guarded electrode is large enough to attain high capacitance values, which help reduce the severity of residual measurement errors.

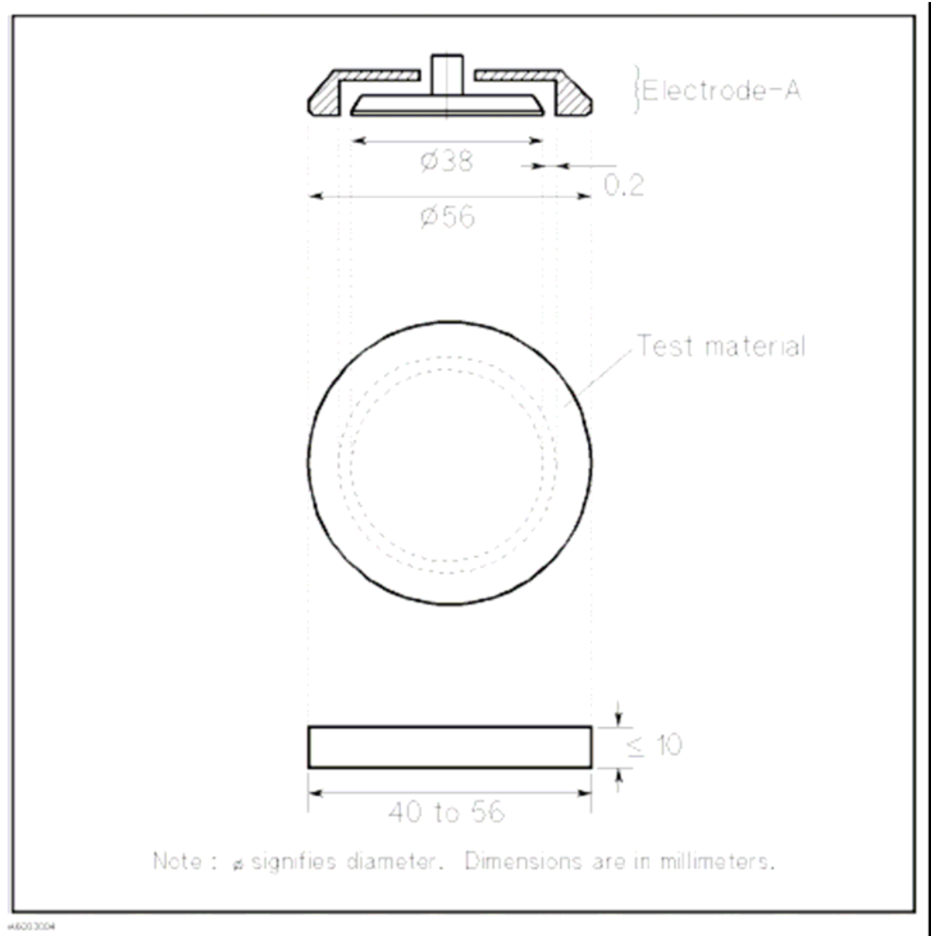

Figure 3-8. Dimensions of the guarded electrode structure for the HP 16451B dielectric test fixture [25]. Copyright 2000 by Agilent Technologies. Reproduced with permission.

Figure 3-9. The capacitive measurement setup with Teflon sample. 1m cable compensation is provided by the 4192 to reduce the effects of the test fixture leads.

By measuring the Teflon sample with ten steps per decade over the range of 1kHz-10MHz, the results shown in Figure 3-10 were obtained. As the results show, the dielectric constant remains constant at a value of 1.92. This is roughly 5% below the expected value of 2.0-2.1. A very slight air gap was observed in the Teflon sample as the measurement was being taken, which is thought to be the primary reason for the discrepancy.

As the frequency rises to 930kHz, the loss tangent suddenly shifts to a negative value. The negative dissipation factor from the measurement data is obviously not a realistic solution. The HP4192A provides *open*/*short* error correction, which is utilized by the *open*/*short* adapter plate in the HP test fixture kit, but does not provide the utility for *load* correction, which is required to eliminate the negative dissipation factor.

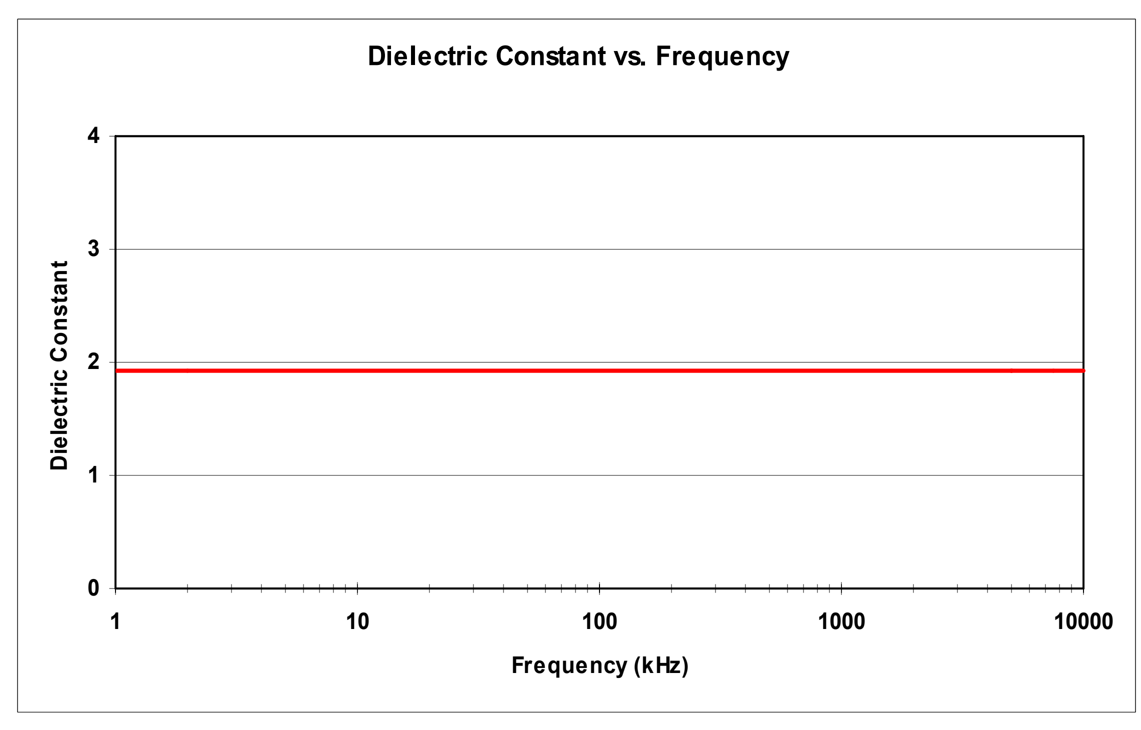

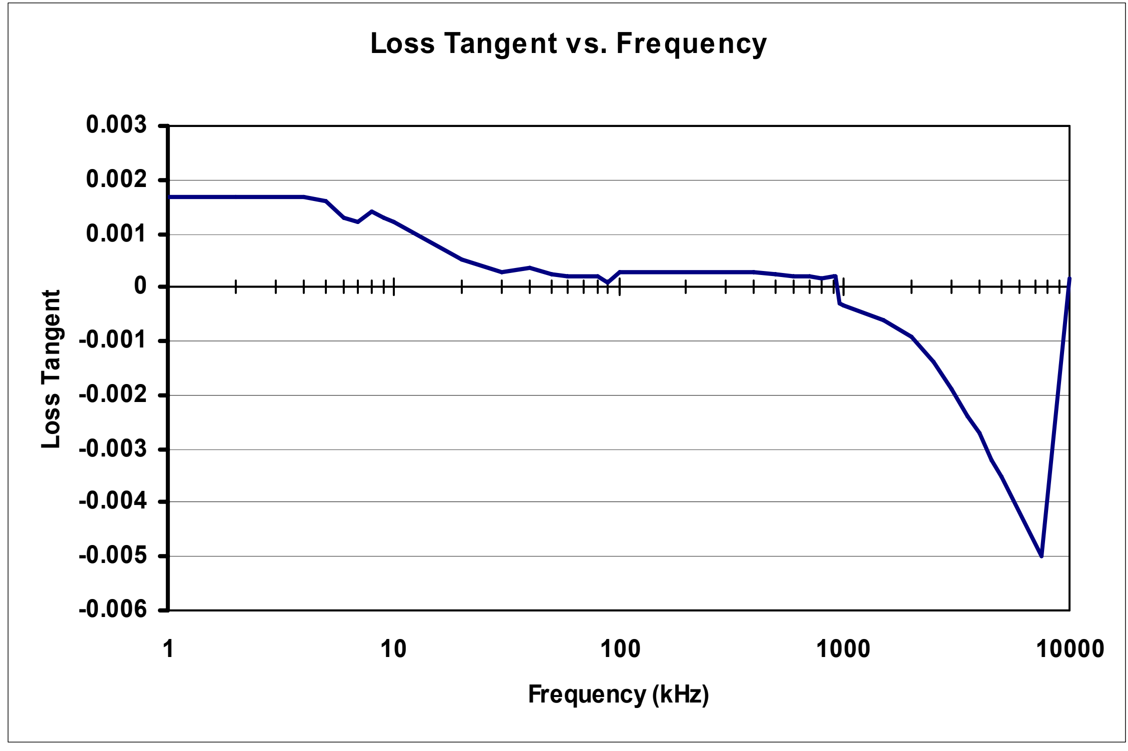

Figure 3-10. Experimental results from the HP16451B dielectric test fixture. The capacitance and dissipation factor of a Teflon sample were measured to obtain the low frequency complex permittivity of the sample.

The loss tangent is clearly much less stable over the measurement frequency range than the dielectric constant. This comes as no surprise, however, as the expected

tan(δ) error for a 1mm sample is given in the HP 16451B users manual as almost 0.01 across the entire spectrum (see Figure 3-11). Since the expected value of Teflon is usually less than 0.005, precise results should not be expected. Higher loss materials would likely fare much better in this measurement, since 0.01 of error in *tan(δ)* is better tolerated in lossy materials than low-loss materials.

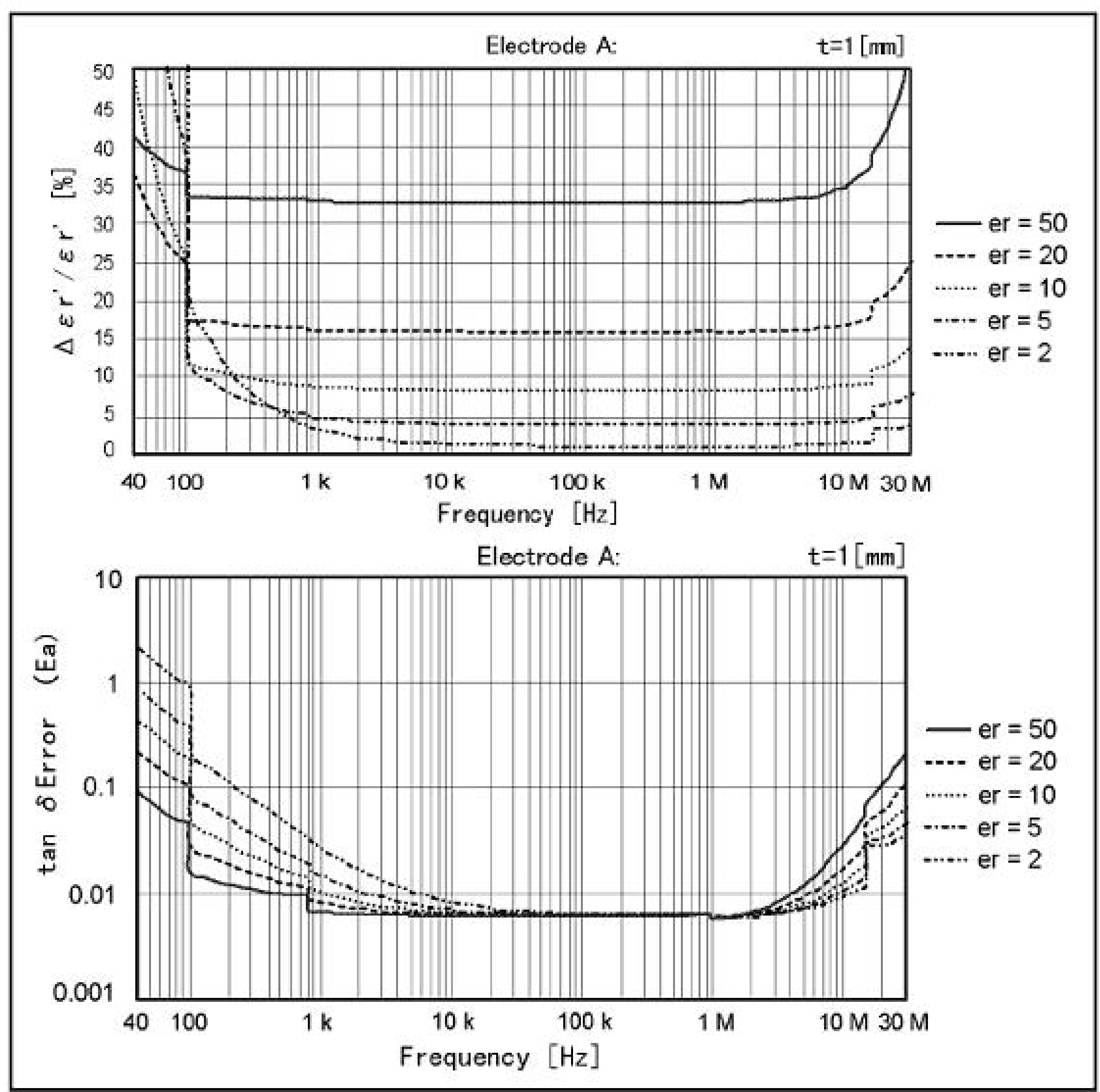

Figure 3-11. Expected error using the HP16451B dielectric test fixture with 38-mm diameter guarded electrode. Copyright 2000 by Agilent Technologies. Reproduced with permission.

In this measurement setup, air gaps between the electrodes and material under test are the single biggest contributor to permittivity error. These air gap effects may be

further reduced by applying direct metallization to the material under test, then using the additional HP thin-film electrodes, as seen in Figure 3-12, to conduct the measurement.

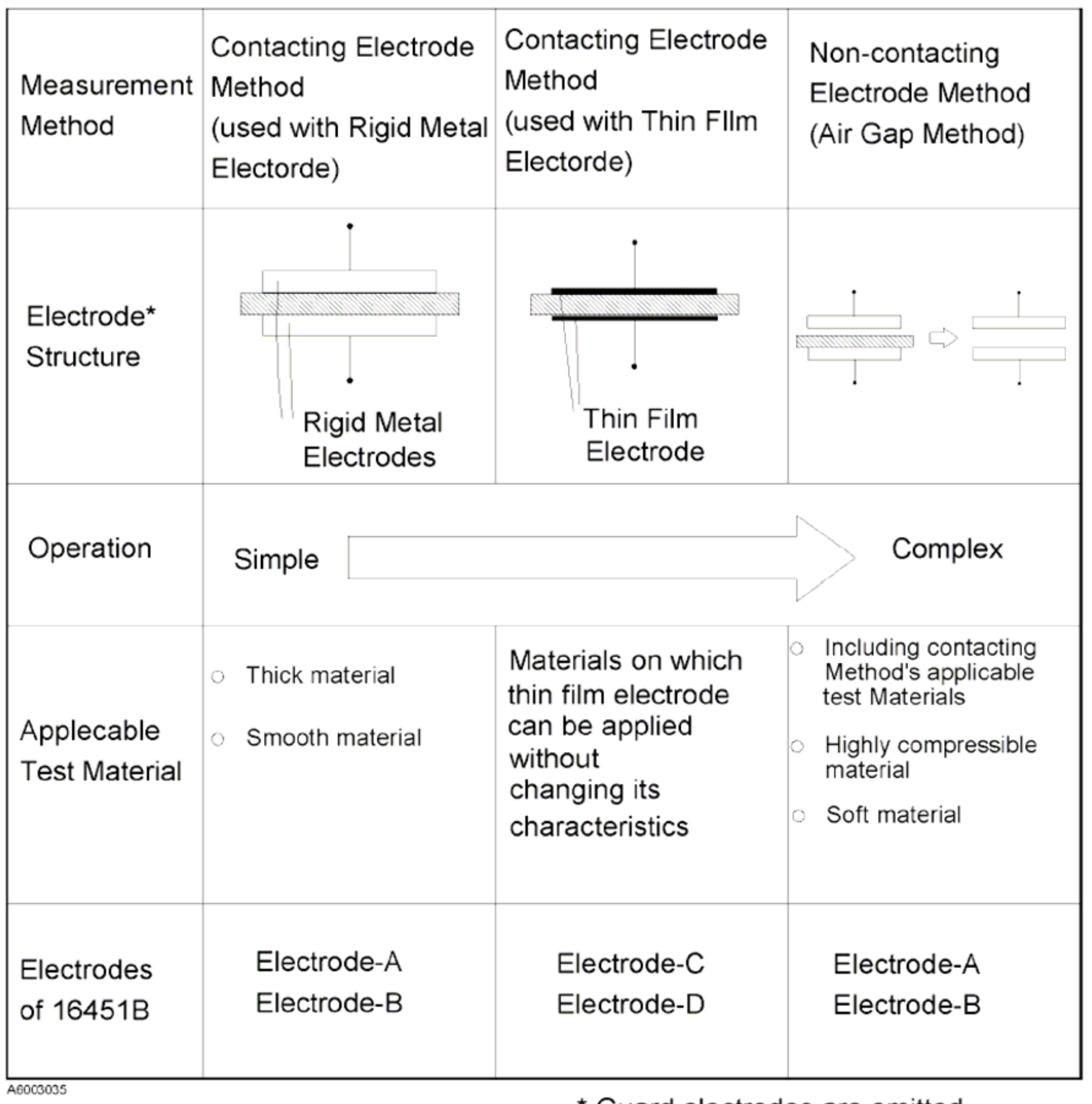

Measurement Method	Contacting Electrode Method (used with Rigid Metal Electorde)	Contacting Electrode Method (used with Thin FIlm Electorde)	Non-contacting Electrode Method (Air Gap Method)
Electrode* Structure	Rigid Metal Electrodes	Thin Film Electrode	
Operation	Simple	→	Complex
Applecable Test Material	○ Thick material ○ Smooth material	Materials on which thin film electrode can be applied without changing its characteristics	○ Including contacting Method's applicable test Materials ○ Highly compressible material ○ Soft material
Electrodes of 16451B	Electrode-A Electrode-B	Electrode-C Electrode-D	Electrode-A Electrode-B

A6003035

* Guard electrodes are omitted

Figure 3-12. Comparison of capacitive measurement techniques using the HP 16451B test fixture [25]. Copyright 2000 by Agilent Technologies. Reproduced with permission.

Chapter 4
X-Band Waveguide Characterization of Thin Dielectric Sheets

4.1 Introduction

Due to the enticing geometry and availability of reflection and transmission coefficients, rectangular waveguides are an effective way of characterizing the electrical properties of materials. Since multiple S-parameters are accessible, a high level of precision and error-checking can be achieved. Many different methods have been devised for use with the rectangular waveguide geometry, but this work focuses primarily upon the measurement of thin sheets of material.

A recent topic of interest is the measurement of RF and microwave-absorbing fabrics, which are useful in a broad range of applications, such as radiation safety and radar detection avoidance. While solids and semisolids can be inserted into a sample-holder or placed inside of a waveguide transmission line, flexible fabrics introduce an additional problem, in that they are sometimes not rigid enough to support themselves without further bracing, which, when added, can inhibit the measurement process. This is important, because if the inserted fabric is not placed strictly in the cross-section of the waveguide, significant errors are likely to occur.

Much of the previous research work using waveguide techniques, while effective, does suffer from a number of drawbacks. Waveguide resonating cavity techniques and other methods requiring that the material be firmly inserted into the waveguide have a series of disadvantages:

- The time required to take a measurement can be extensive, since sample preparation is a very involved process
- The surface of the cavity walls can eventually become scratched or deformed, due to repeated insertion and removal of the sample.
- The material must be machined to fit exactly inside the cavity. The presence of air gaps around the inner wall of the cavity introduces an error, which can be quite large in some situations.

- Unless special care is taken, the material can become compressed as it is inserted into the waveguide. This typically leads to a change in the electrical properties of the material.
- The material must support itself when placed inside of the waveguide.
- The placement of the material must be extremely precise, or else unexpected results may occur.

This chapter of the thesis focuses on the use of rectangular waveguides in the 8.2-12.4 GHz range to measure the dielectric properties of materials. To eliminate the requirement that a sheet of material be radically altered or formed to fit inside of the waveguide, the sample can be securely placed between two waveguide sections, as shown in Figure 4-1. This introduces the problem of radiation leakage, however, as well as the possible formation of additional modes [27], at the interface of the material, which cause problems when solving for the complex permittivity. The eventual goal of this research is to overcome these problems, but significant development is needed before these problems can be directly addressed. Therefore, this chapter develops the basic theory, inverse solution algorithm, and processes for the simpler case of the material placed inside of a waveguide extension section, and then briefly explores the more complex situation in which the material is placed directly at the measurement reference plane between the two waveguide openings.

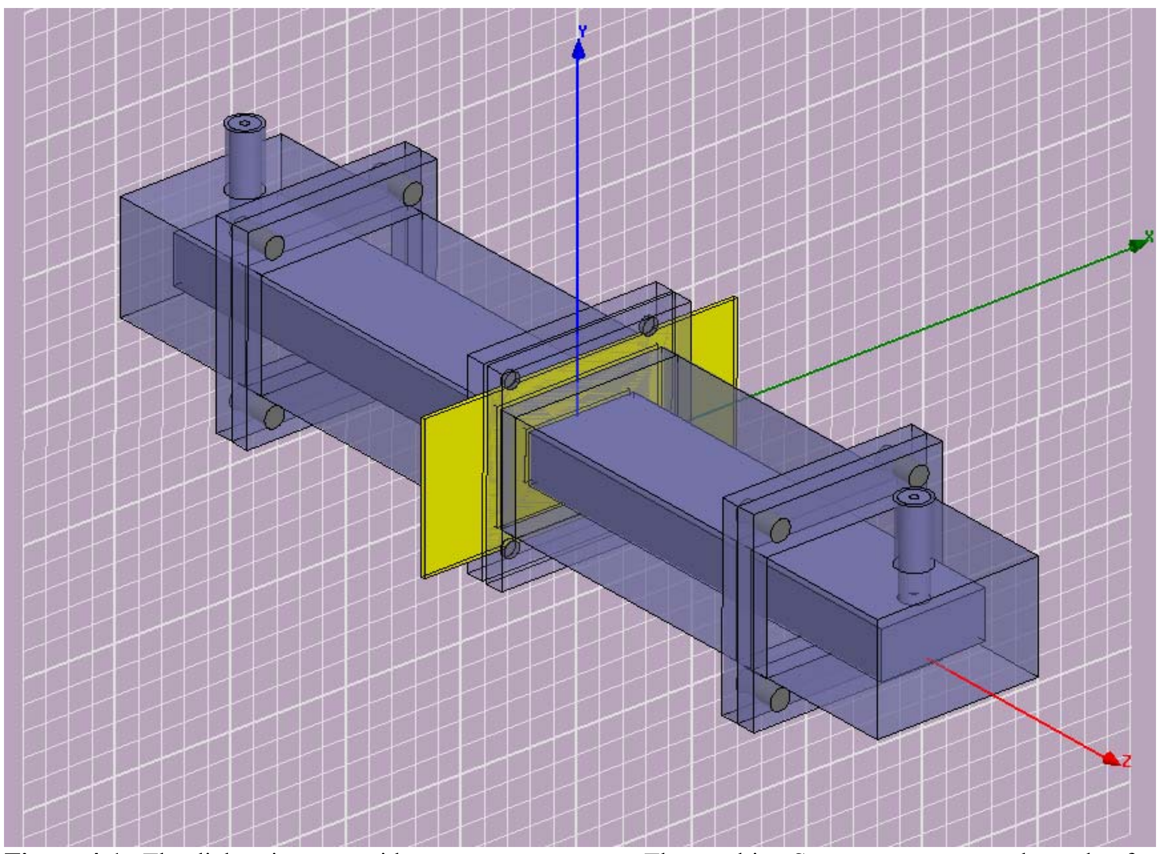

Figure 4-1. The dielectric waveguide measurement setup. The resulting S-parameters are used to solve for the unknown material properties of the sample.

The X-band, which consists of the 8.2-12.4GHz frequency range, is an important frequency band because the permittivity of materials in this range is of widespread interest. With the advent of broadband communication systems, wideband characterization of materials is essential. Also, many modern radar systems, as well as satellite and communication systems, rely heavily upon this frequency range. Therefore, studies of such topics as radar absorption require precise determination of complex material properties within this frequency range.

Since this method combines transmission and reflection techniques, rather than using a reflection-only technique, three complex independent measurement quantities are available, due to the complex nature of s_{11}, s_{22}, and s_{21}. s_{21} and s_{12} are equivalent since the sample is a passive reciprocal network. Since the scope of this research work has been limited to the determination of complex permittivity, which consists of only one complex quantity, the problem is overstated. The solution to the problem can therefore be further enhanced through the use of a direct-search optimization routine, which is covered at the

end of this chapter. The recommended future work, however, suggests expanding the solution to include as unknowns the sample thickness or the complex permeability of the sample, which will facilitate the measurement of magnetic quantities.

The waveguide sections placed between the material under test and coaxial-waveguide adapters are an essential component of the measurement setup, since higher-order modes normally exist in the vicinity of the coaxial-waveguide adapters. Since the cross-sectional dimensions of the waveguide prevent these higher-order modes from propagating, they are referred to as evanescent modes and are typically attenuated over the distance of the waveguide extension sections. All of the waveguide analysis in this chapter is done assuming only the TE_{10} mode of propagation, and higher-order modes are undesirable, since they add uncertainty. Hence, these sections are referred to as mode filters, since they prevent the higher-order evanescent modes from reaching the sample region and corrupting the measured data.

4.2 Systematic Error

One of the main factors differentiating the following work from previous work is the manner in which the systematic error is dealt with. A database of 3-dimensional electromagnetic simulation error matrices will be used to mitigate the effects of the error and produce satisfactory results. The handling of systematic errors in the experimental environment is extremely important and plays a major role in the legitimacy of the solution. With the ability to produce simulated results from essentially any desired case, a large database of error data is produced, from which the influence of variables upon the systematic error can be effectively characterized. Such variables include waveguide conductor type, material thickness, and complex permittivity.

Even though the presented error-removal method is applied to the rectangular waveguide geometry in this thesis, the idea of error removal through the use of a simulated error library can be expanded to include many other configurations. The approach holds massive potential for the future of dielectric characterization, as material properties can ideally be found in any situation where the fields can be accurately and precisely modeled. In fact, it may even be possible to extrapolate material properties from cases in which no previous theoretical analysis has been conducted. Due to

exorbitant advances in computing power, ultra-detailed simulations are now much more plausible than they were ten years ago. As a result, much smaller changes in dielectric constant and loss tangent can be resolved from the simulated and measured data.

Systematic Error

When measurements are taken, there are two possible causes of error. These error types are commonly known as random error and systematic error. The differentiation between these error types lies in the fact that systematic errors are somewhat repeatable for a given system, while random errors are unrepeatable, and the errors are dealt with in completely different ways. Random errors are dealt with statistically, since they can be reduced by applying clever averaging techniques. Systematic errors, on the other hand, must be specifically characterized for the given system. While random errors are largely unexplainable and unrepeatable, systematic errors result from human factors or instrument biases.

Measured data will perpetually contain unavoidable errors. Some of these errors are:

- 8510C TRL calibration error [28]
  - Imperfect calibration standards
  - Imperfect mating of flanged WG sections
- Compression and/or stretching of material as it is squeezed by waveguide flanges
- Ambiguity in exact material thickness
- If material is a threaded/meshed fabric, thickness is not uniform, and can therefore not be given an exact value.

Outside of the material thickness, the source of a systematic error is irrelevant, as long as it remains repeatable. All of the error is grouped together as a systematic error, which the inverse solution algorithm has been designed to handle.

Since the systematic error is dependent upon both the dielectric constant and loss tangent of the material, finding its dependence upon the complex permittivity is a complex task. If the electrical properties of enough materials were known, the systematic error could be well characterized by physically measuring a large sample set, then

extrapolating the systematic error. Unfortunately, there are only a few materials in existence for which the electrical properties are well-known. Due to the unpredictable nature of the error, a large range of samples in the (ε', ε'') space is needed, which makes this approach very difficult to implement. Since the systematic error can also depend upon the sample thickness, a sample measurement for each thickness at each (ε', ε'') point would also be necessary to effectively characterize it. Unless special care was taken during the measurement of each sample, random errors would begin to factor in to the systematic error removal process.

The preceding approach is obviously not a practical way to characterize the systematic error, so another approach must be taken. In this thesis, a 3-dimensional electromagnetic simulation approach is employed to characterize the error. Since the material properties can be set to any desired values in the simulator, a large matrix of simulations can be run. Then, the simulated systematic error is found by taking the difference between the simulated and theoretical S-parameters. By performing this action for a large spectrum of ε', ε'', and thickness values, a robust error library can be produced. Then, when an unknown sample is measured and the direct search solution algorithm is employed, the systematic error can be accounted for by using the simulated systematic error from a simulated case with similar permittivity and thickness values.

In order for this approach to be successful, a couple of assumptions must be made.

- The systematic error trend for experimental cases must match that of the simulated cases. In other words, the simulator must give trustworthy results.
- The systematic error must stay relatively constant between simulated points. To produce an acceptable solution, the inverse solution algorithm interpolates the error from surrounding "known" cases. If there is a large gradient in the error between consecutive points, the interpolated error will not be reliable.

It is worth noting that the errors being discussed here pertain only to measurement errors and have nothing to do with calculation discrepancies. Any errors involved in the actual solution process and calculations are omitted from this discussion. As will be seen, the problem at hand is overstated, meaning there are more independent equations

than unknown variables. As a result, a least-squares optimization scheme is used. Since multiple solutions exist for all of the equations, the solution is somewhat of a compromise.

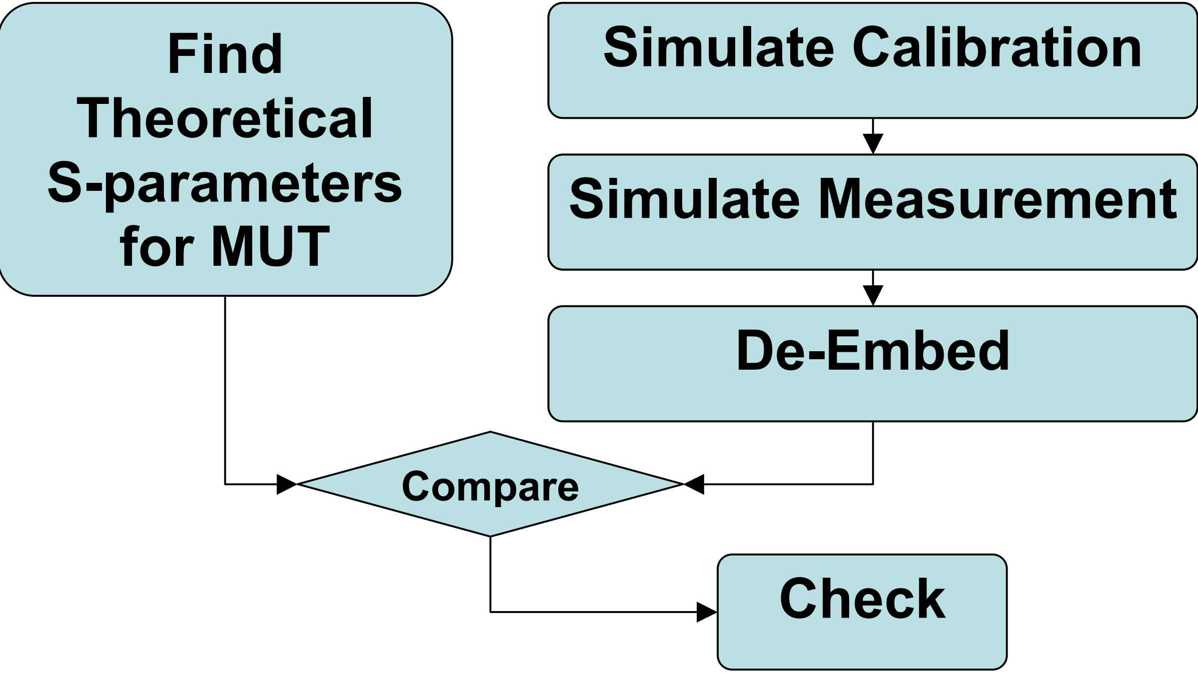

Figure 4-2. Flow chart of simulated waveguide verification. The chart presents the analysis necessary to check the precision of the 3D EM waveguide simulations.

4.3 De-Embedding of Material S-parameters from Simulation

In order to compare the results from the electromagnetic simulator to both the theoretical and measured S-parameters, it is necessary to de-embed the S-parameters of the material under test (MUT). This is not a simple task, since the characteristic impedance changes throughout the system, and a calibration at the plane of the material within the 3D EM simulator is a very involved process. Therefore, a method of moving the reference plane and removing the effects of the waveguide adapters is required in order to directly examine the response of the material under excitation [29].

Regardless of the component(s) being measured, the system, or network, can be broken down into individual parts, each of which is represented by a matrix, detailing it's response to a stimulus. This matrix, known as the S-parameter matrix, is sufficient to fully quantify the electrical performance of the device or component. If the S-parameters

of each component within the system are known over the frequencies of interest, then the overall response can be found. There are various methods of finding the overall response of electrical networks.

Two effective methods of S-parameter simplification are signal flow diagrams and cascaded T-parameter matrices. Depending upon the purpose of the experiment or problem, one method may work better than the other. Both of the following methods give the same answer, but the simplicity varies depending upon which method is chosen.

A signal flow diagram is a system-level graph comprised of a number of nodes, each of which represents either an incoming or outgoing signal, depending on which component it is referenced to. The arrows between each node are labeled with a multiplier, which displays the amount of signal that is received at the node to which it points. By using a set of rules from control systems graph theory, the signal flow graph can be condensed to a very simple graph which shows the overall response.

A second effective method utilizes T-parameter matrices. Each S-parameter matrix can be transformed into a transmission matrix, or T-matrix, which is in a form that allows for the response of cascaded networks to be found by multiplying their T-matrices together. Once these matrices have been multiplied together, the resulting T-matrix can be transformed back into an S-parameter matrix, which gives the overall response of the network. Since T-parameter methods are more prone to numerical errors, cascaded S-parameters are used in this thesis.

$$\begin{pmatrix} s_{11} & s_{12} \\ s_{21} & s_{22} \end{pmatrix} = \begin{pmatrix} \frac{T_{12}}{T_{22}} & \frac{T_{11}T_{22} - T_{12}T_{21}}{T_{22}} \\ \frac{1}{T_{22}} & -\frac{T_{21}}{T_{22}} \end{pmatrix} \tag{4.1}$$

$$\begin{pmatrix} T_{11} & T_{12} \\ T_{21} & T_{22} \end{pmatrix} = \begin{pmatrix} -\frac{s_{11}s_{22} - s_{12}s_{21}}{s_{21}} & \frac{s_{11}}{s_{21}} \\ -\frac{s_{22}}{s_{21}} & \frac{1}{s_{21}} \end{pmatrix} \tag{4.2}$$

For this project, the S-parameters of the material are simulated with the Ansoft HFSS simulator. From the simulated results, the material S-parameters are de-embedded in order to observe the results and come to conclusions of the material properties.

To facilitate S-parameter de-embedding in this work, the coaxial-waveguide adapter and mode filter for each side are lumped together to form a single entity, as shown in Figure 4-3. This combination will be referred to as the **launcher section** from this point on.

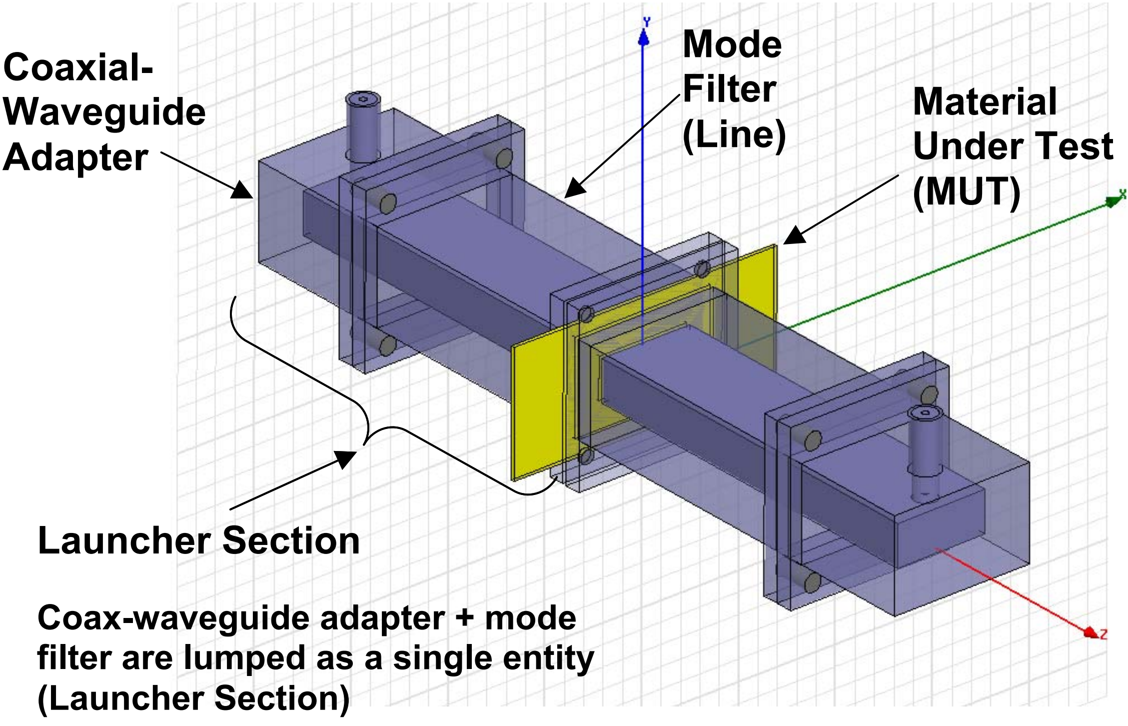

Figure 4-3. Components of the waveguide measurement setup. The effects of the launcher section must be removed before the material properties can be found.

As long as the S-parameters of the waveguide launcher section remain unknown, it is not possible to have knowledge of the response of the material to an excitation. Therefore, the first task involves figuring out the S-parameters of the waveguide launcher section. Then, its effects can be removed from the overall S-parameters given by the electromagnetic field simulator, which allows for direct comparison of the simulated S-parameters to the theoretical and physically measured S-parameters. Note that the 8510 network analyzer will be calibrated at the plane of the material test fixture, with ports 1 and 2 being located directly on either side. This TRL calibration removes the errors and

effects of the waveguide adapters and mode filters and allows for direct viewing and comparison of the S-parameters.

For each launcher section, the coaxial side of the coaxial-to-waveguide adapter is designated as port 1, while the rectangular waveguide opening of the mode filter is port 2. The four unknown quantities are s_{11LS}, s_{12LS}, s_{21LS}, and s_{22LS}, with the subscript "LS" representing the phrase "Launcher Section". Due to the reciprocity of the passive network, s_{12LS} is equal to s_{21LS}.

To simplify the de-embedding of the material S-parameters, only the symmetrical material-filled portion of the test fixture is simulated, and it is represented by the s-parameter matrix

$$\begin{pmatrix} s_{11M} & s_{12M} \\ s_{21M} & s_{22M} \end{pmatrix} = \begin{pmatrix} s_{11M} & s_{21M} \\ s_{21M} & s_{11M} \end{pmatrix}$$

After the s-parameters of the material-filled section have been simulated and de-embedded, simple theoretical analysis is used to add the effects of the additional air-filled portion of the test fixture. The preceding two-step process greatly simplifies the de-embedding the S-parameters of the asymmetrical test fixture.

The signal-flow graph of the measurement network is shown in Figure 4-4, with each of the components represented by a set of S-parameters, where

$s_{11M} = s_{11}$ of the material-filled portion of the sample holder
$s_{21M} = s_{21}$ of the material-filled portion of the sample holder

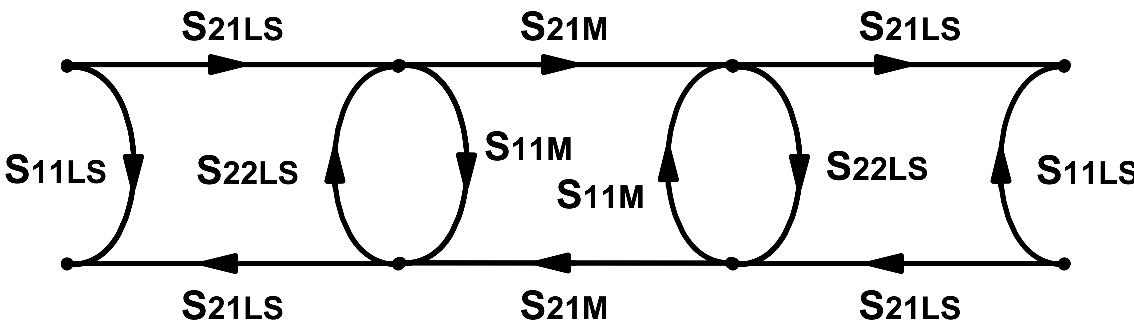

Figure 4-4. The S-parameter signal flow diagram of the cascaded waveguide configuration. Using signal-flow reduction techniques, the cascaded S-parameters can be found.

Note that the parameters of the two launcher sections are identical, but the directions are reversed, since a voltage wave traveling through the system sees them as being turned in opposite directions. The S-parameter matrix of the material under test is symmetrical, since the material is assumed to be a linear, homogeneous, isotropic, time-invariant medium. The effects of the additional material-filled portion of the sample holder will be added after the de-embedding of the symmetrical portion is complete.

When the internal reference impedances of the ports are different than that of the outer port impedances, the simplification of the cascaded S-parameters to a single matrix is still a perfectly valid operation. This is due to the fact that the S-parameters of each port are reliant upon the impedances that they are connected to, and this dependence is taken into account in the definition of the S-parameters.

Using the techniques of signal flow graph reduction [30], the overall signal flow graph is reduced to a simplified graph, from which the overall s_{11} and s_{21} can be read directly. The quantity Δs_M is now defined as

$$\Delta s_M = s_{11M}^2 - s_{21M}^2 \tag{4.3}$$

Using the previously outlined procedure and signal flow reduction techniques, the overall cascaded S-parameters of the network are found as

$$s_{11} = s_{22} = s_{11LS} + \frac{s_{21LS}^2 (s_{11M} - \Delta s_M s_{22LS})}{1 - 2 s_{22LS} s_{11M} + \Delta s_M s_{22LS}^2} \tag{4.4}$$

$$s_{21} = s_{12} = \frac{s_{21LS}^2 s_{21M}}{1 - 2 s_{22LS} s_{11M} + \Delta s_M s_{22LS}^2} \tag{4.5}$$

Only s_{11} and s_{21} need to be found, since the setup is symmetrical with

$$s_{22} = s_{11} \tag{4.6}$$

and

$$s_{12} = s_{21} \tag{4.7}$$

From (4.4) and (4.5), it is the aim to solve for s_{11M} and s_{21M}, which have been defined as the S-parameters of the material-filled section of the sample holder.

There are three unknown quantities, s_{11LS}, s_{22LS}, and s_{21LS}, for which three independent equations are needed to solve. By connecting the two launcher sections directly together, two independent equations are obtained, one for the overall reflection s_{11D} and one for the overall transmission s_{21D}, with the subscript D representing a direct connection of the adapters. To obtain a third equation, an original attempt was made to utilize a single adapter with a short-circuit termination, which is very easily constructed in the rectangular waveguide geometry. It was quickly realized, however, that the equation obtained for s_{11SC}, the reflection coefficient with a short-circuit termination on port 2 of the launcher section, is a linear combination of the other two equations, and therefore does not give the ability to independently solve for each of the three unknowns. As a result, a technique commonly used by a standard TRL, or *Thru-Reflect-Line*, calibration is employed. A short waveguide *line* extension, for which the S-parameters are known [31] to be

$$\begin{pmatrix} s_{11L} & s_{21L} \\ s_{21L} & s_{11L} \end{pmatrix} = \begin{pmatrix} 0 & e^{-j\beta l} \\ e^{-j\beta l} & 0 \end{pmatrix} \tag{4.8}$$

is placed in between the two waveguide adapters. The length of the *line* section must be such that it does not equal $\lambda_G/2$ at any frequency of interest. From transmission line theory [31],

$$Z_{in} = Z_O \frac{Z_L + jZ_O \tan \beta l}{Z_O + jZ_L \tan \beta l} \tag{4.9}$$

where

Z_O = The characteristic impedance of the line extension

Z_L = The input impedance looking into the end of the line extension.

In the special case when $l = \lambda_G/2$, (4.9) simplifies to

$$Z_{in} = Z_L \tag{4.10}$$

which renders the *line* section essentially nonexistent, since the input impedance repeats at intervals of $\lambda_G/2$. Since this imitates the undesirable situation in which the waveguide launcher sections are connected directly to one another, a third independent equation is unobtainable at that frequency. This has the effect of invalidating the data for all frequencies at which the length of the *line* extension is close to a multiple of $\lambda g/2$. Table 4-1 gives the wavelengths of interest.

Table 4-1. Guided wavelengths across the frequencies of interest.

Freq (GHz)	Λo (cm)	λg (cm)	Λg/2 (cm)
6.0	5.0000	Cutoff	Cutoff
6.5	4.6154	Cutoff	Cutoff
7.0	4.286	12.236	6.118
7.5	4.000	8.235	4.118
8.0	3.750	6.542	3.271
8.5	3.529	5.543	2.771
9.0	3.333	4.863	2.432
9.5	3.158	4.361	2.181
10.0	3.000	3.971	1.985
10.5	2.857	3.656	1.828
11.0	2.727	3.394	1.697
11.5	2.609	3.173	1.587
12.0	2.500	2.983	1.492
12.5	2.400	2.817	1.409
13.0	2.308	2.671	1.335
13.5	2.222	2.541	1.270
14.0	2.143	2.424	1.212

Since WR90 waveguides are specified to be operable from 8.2-12.4GHz [31], the only concerns are the $\lambda_G/2$ values in this range, which is shaded in gray in Table 4-1. From Table 4-1, it is obvious that the length of the *line* extension must be less than 1.40cm (555 mils). Therefore, for the de-embedding of the simulated S-parameters, a 400 mil (1.016cm) *line* extension, for which the $\lambda g/2$ length criteria does not become a problem until the frequency reaches 16GHz, has been chosen. This is a wise choice, since 16GHz is well beyond the intended frequency range of this project.

Next, a simulation is run with the *line* extension in place. From the results of this simulator, a third independent equation is obtained, allowing all three of the unknown launcher section S-parameters to be solved for.

$$s_{22LS} = \frac{s_{11D} - s_{11X}}{s_{21D} - s_{21X} s_{21L}} \tag{4.11}$$

$$s_{21LS}^2 = s_{21D}\left(1 - s_{22LS}^2\right) \tag{4.12}$$

$$s_{11LS} = s_{11D} - \frac{s_{PLS} s_{22LS}}{(1 - s_{22LS}{}^2)} \quad (4.13)$$

where

S_{11LS} = S_{11} of the waveguide launcher section

S_{22LS} = S_{21} of the waveguide launcher section

S_{21LS} = S_{21} of the waveguide launcher section

S_{11D} = S_{11} of 3D EM simulation with direct connection of launchers

S_{21D} = S_{21} of 3D EM simulation with direct connection of launchers

S_{11X} = S_{11} of 3D EM simulation with waveguide line extension

S_{21X} = S_{21} of 3D EM simulation with waveguide line extension

S_{21L} = Theoretical S_{21} of waveguide line extension

Once the S-parameters of the waveguide launcher section are known, the S-parameters of the material can be computed. Then, from these parameters, the material properties are determined through the use of a direct search inverse solution algorithm. Using the symbolic solver from within MATLAB®, the solve() function is used to simultaneously symbolically solve (4.4) and (4.5) for the material S-parameters in terms of the launcher section S-parameters.

$$s_{11M} = \frac{-s_{21H}^2 s_{22LS} + s_{PLS} s_{11H} - s_{PLS} s_{11LS} + s_{11H}^2 s_{22LS} - 2 s_{11H} s_{22LS} s_{11LS} + s_{11LS}^2 s_{22LS}}{-s_{21H}^2 s_{22LS}^2 + s_{PLS}^2 + 2 s_{PLS} s_{11H} s_{22LS} - 2 s_{PLS} s_{11LS} s_{22LS} + s_{11H}^2 s_{22LS}^2 - 2 s_{11H} s_{22LS}^2 s_{11LS} + s_{11LS}^2 s_{22LS}^2} \quad (4.14)$$

$$s_{21M} = \frac{s_{21H} s_{PLS}}{-s_{21H}^2 s_{22LS}^2 + s_{PLS}^2 + 2 s_{PLS} s_{11H} s_{22LS} - 2 s_{PLS} s_{11LS} s_{22LS} + s_{11H}^2 s_{22LS}^2 - 2 s_{11H} s_{22LS}^2 s_{11LS} + s_{11LS}^2 s_{22LS}^2} \quad (4.15)$$

where

s_{11H} = s_{11} of the 3D EM simulation with the MUT

s_{21H} = s_{21} of the 3D EM simulation with the MUT

s_{11M} = s_{11} of the material under test

s_{21M} = s_{11} of the material under test

Since the sample is asymmetrically placed in the sample-holder, as illustrated in Figure 4-5, the effects of the air-filled sections of the test fixture must be added to allow for comparison with the measured data. The following adjustments are made to obtain the updated S-parameters, s_{11M}', s_{22M}', and s_{21M}', of the full sample holder:

$$s_{11M}^{'} = s_{11M} e^{-2(\alpha_o + j\beta_o) d_1} \tag{4.16}$$

$$s_{22M}^{'} = s_{22M} e^{-2(\alpha_o + j\beta_o) d_3} \tag{4.17}$$

$$s_{21M}^{'} = s_{21M} e^{-(\alpha_o + j\beta_o) d_1} e^{-(\alpha_o + j\beta_o) d_3} \tag{4.18}$$

where

α_o = The attenuation constant in the air-filled waveguide section

β_o = The propagation constant in the air-filled waveguide section

d_1 = Distance between port 1 and the material under test

d_3 = Distance between port 2 and the material under test

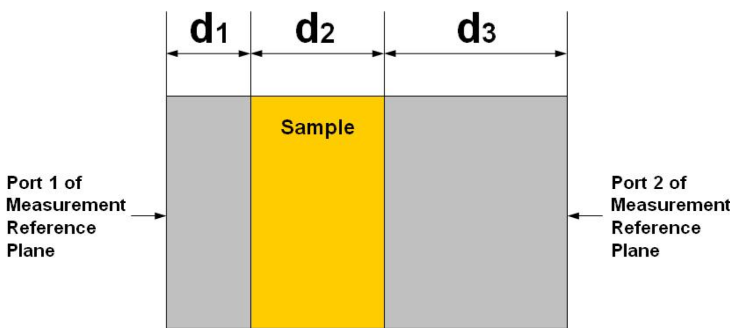

Figure 4-5. Side view of the asymmetrical sample holder.

It is worth mentioning that the previous analysis is performed over a large range of frequencies. The S-parameters of the waveguide launcher section must be found at every frequency for which the material properties are desired to be found. This task is greatly simplified, however, by using a MATLAB® loop to perform the analysis at each requested frequency. The following steps review the preceding process of determining the material S-parameters from 3D EM simulations:

(1) Pick a suitable length for the waveguide mode filters.
(2) Simulate a direct connection of the launcher sections.
(3) Simulate the 400-mil *line* section in between the waveguide launcher sections.
(4) Use the S-parameters from parts (2) and (3), along with (4.11), (4.12), and (4.13), to calculate the S-parameters of the launcher section.
(5) Simulate the setup with the material inserted between the launcher sections.
(6) Use (4.14) and (4.15) to calculate the S-parameters for the material.
(7) Add the effects of the air-filled sections of the sample holder.

4.4 Theoretical S-parameters

The theoretical analysis process involves a large number of steps, and is an essential step in the verification of the validity of the simulation results. After de-embedding the S-parameters of a known material from the field simulation, the results can then be compared to the theoretical values to determine the precision and accuracy of the field simulator. Also, as the later development shows, the theoretical S-parameters play a crucial role in the determination of the unknown complex permittivity of the sample being measured.

The theoretical S-parameters can be found in multiple ways, but perhaps the simplest method for this problem is through the use of a time-domain bounce diagram [31]. By summing the instantaneous reflected and transmitted components of an incident wave, the theoretical S-parameters are found. Since the propagation characteristics and characteristic impedance of the waveguide in the TE_{10} mode are well-known, the task is greatly simplified. Once the TE_{10} waveguide impedance of each waveguide section is

known, standard transmission line theory is used to conduct the analysis, and the angle of incidence is not a factor.

From each impedance discontinuity at the waveguide-material junction, the instantaneous reflection coefficient can be found as

$$\rho = \frac{Z_{o,m} - Z_o}{Z_{o,m} + Z_o} \tag{4.19}$$

where

Z_o = Characteristic impedance of the vacuum-filled waveguide

$Z_{o,m}$ = Characteristic impedance of the material-filled waveguide

The guided TE_{10} characteristic impedance of each rectangular metallic waveguide section is given in [31] as

$$Z_{TE} = \frac{k\eta}{\beta} \tag{4.20}$$

with

$$k = \omega\sqrt{\mu\varepsilon} \tag{4.21}$$

$$\eta = \sqrt{\frac{\mu_o}{\varepsilon_o\varepsilon_r}} \tag{4.22}$$

$$\beta = \sqrt{k^2 + k_c^2} \tag{4.23}$$

$$k_c = \frac{m\pi}{a} \tag{4.24}$$

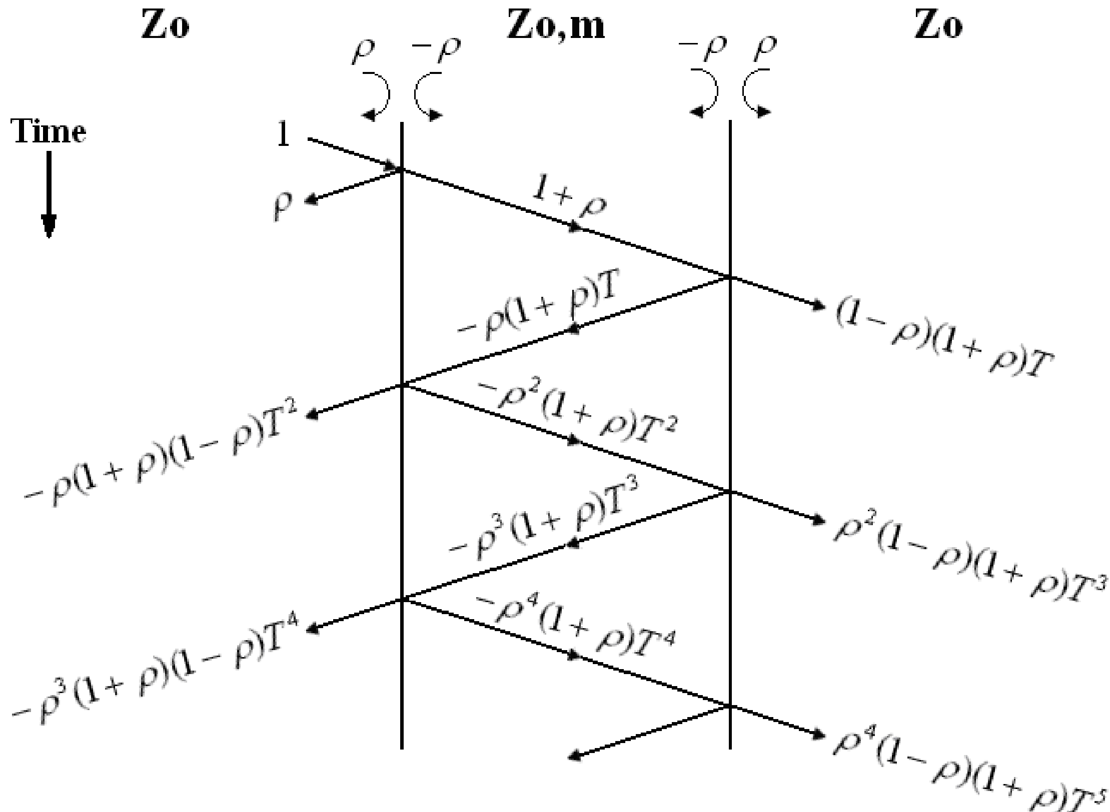

Figure 4-6. A theoretical bounce diagram. The reflected and transmitted waves are summed to give S_{11M} and S_{21M}, respectively.

With

$$\rho = \frac{Z_{o,m} - Z_o}{Z_{o,m} + Z_o} \tag{4.25}$$

and

$$T = e^{-\gamma l} = e^{-(\alpha + j\beta)l} \tag{4.26}$$

A guided wave propagating in the TE_{10} mode incurs attenuation due to the finite conductivity of the waveguide metal. The conductor losses, α_c, are represented in nepers per meter and grow exponentially as the cutoff frequency of the waveguide is approached from above. In the material-filled region, the dielectric losses are added to the conductor losses to represent the overall losses as α (Np/m) [31].

$$\alpha_c = \frac{R_s}{a^3 b \beta k \eta}(2b\pi^2 + a^3 k^2) \tag{4.27}$$

where R_s, the wall surface resistance, is given by [31]

$$R_s = \sqrt{\frac{\omega\mu}{2\sigma}} \tag{4.28}$$

and σ represents the waveguide metal conductivity.

Since the incident wave of unity amplitude imitates a calibrated reference plane, the sum of the reflected waves is equal to $s_{11M,Theoretical}$, while the sum of the transmitted waves is equal to $s_{21M,Theoretical}$.

$$s_{11M,Theoretical} = \rho - \rho(1+\rho)(1-\rho)T^2 - \rho^3(1-\rho)(1+\rho)T^5 - \ldots \tag{4.29}$$

$$s_{21M,Theoretical} = (1-\rho)(1+\rho)T + \rho^2(1-\rho)(1+\rho)T^3 + \rho^4(1-\rho)(1+\rho)T^5 + \ldots \tag{4.30}$$

As (4.29) and (4.30) show, an infinite series can be seen in the results. Using the geometric series simplification, the equations simplify to

$$s_{11M,Theoretical} = \rho - \frac{\rho(1-\rho^2)T^2}{1-(\rho T)^2} \tag{4.31}$$

and

$$S_{21M,Theoretical} = \frac{(1-\rho^2)T}{1-(\rho T)^2} \tag{4.32}$$

Since the waveguide line extension will not always be the same as the sample thickness, the facility to include an extra length of waveguide must be included. By summing the components from the expanded bounce diagram in Figure 4-7, it is seen that the extra line section does not have a dramatic effect on the resulting S-parameters:

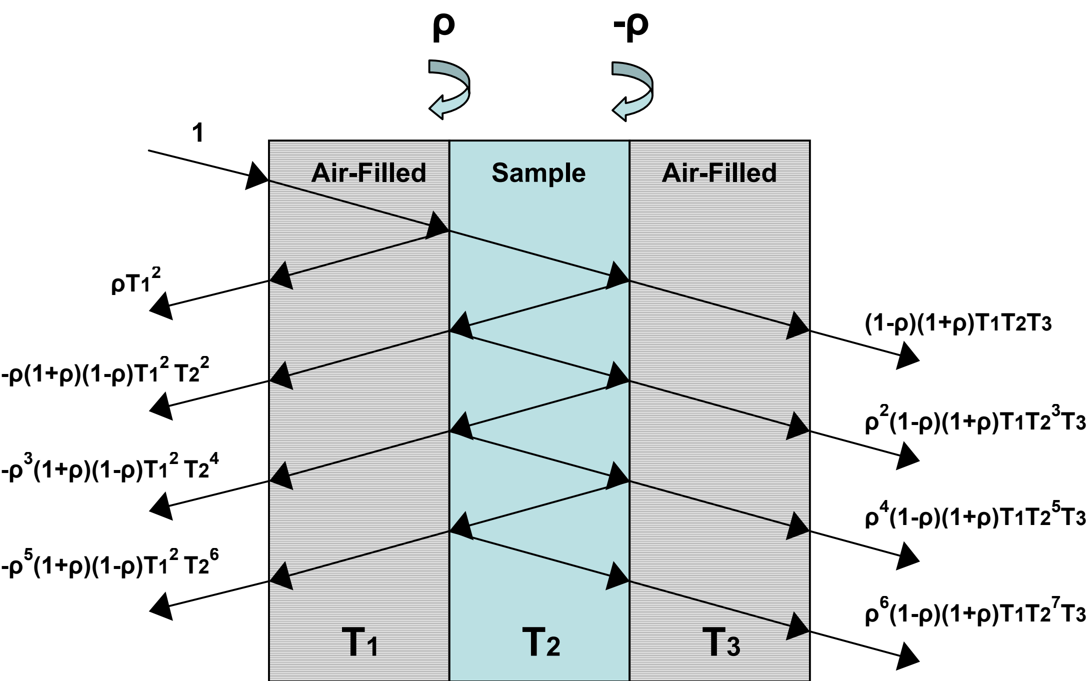

Figure 4-7. Bounce diagram expanded to include the extra length introduced by the sample holder.

$$T_1 = e^{-(\alpha_o + j\beta_o)d_1} \tag{4.33}$$

$$T_2 = e^{-(\alpha_m + j\beta_m)d_2} \tag{4.34}$$

$$T_3 = e^{-(\alpha_o + j\beta_o)d_3} \tag{4.35}$$

where

α_o = The attenuation constant in the air-filled waveguide section

β_o = The propagation constant in the air-filled waveguide section

α_m = The attenuation constant in the dielectric-filled waveguide section

β_m = The propagation constant in the dielectric-filled waveguide section

and the distances d_1, d_2, and d_3 are defined in Figure 4-8.

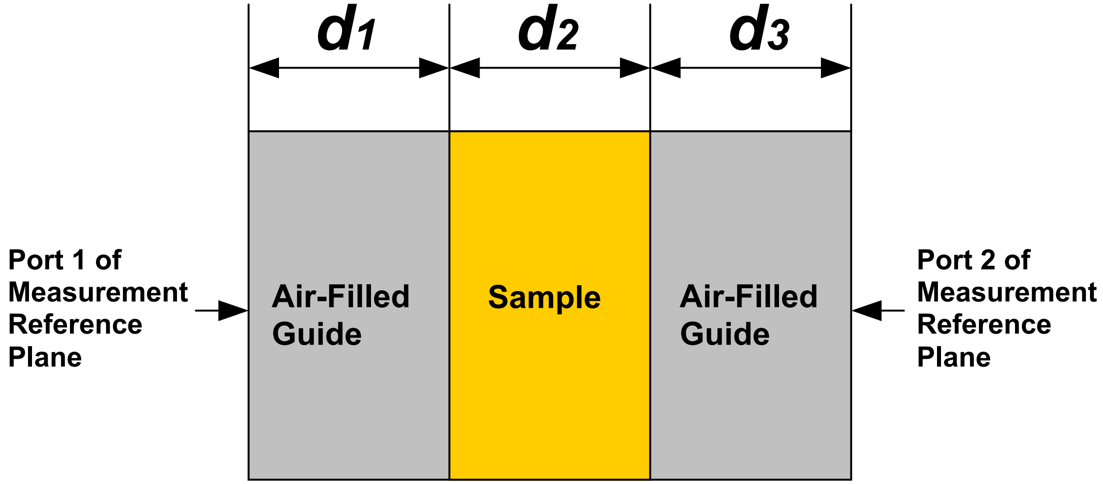

Figure 4-8. Side view of the sample holder. The distances d_1, d_2, and d_3 are used to solve in the solution of the theoretical S-parameters.

The updated theoretical S-parameters, $s_{11M,Theoretical,X}$, and $S_{21M,Theoretical,X}$, are obtained by summing the components from the bounce diagram:

$$s_{11M,Theoretical,X} = \rho T_1^2 - \frac{\rho(1-\rho^2)(T_1 T_2)^2}{1-(\rho T_1 T_2)^2} \tag{4.36}$$

and

$$S_{21M,Theoretical,X} = \frac{(1-\rho^2)(T_1 T_2 T_3)}{1-(\rho T_1 T_2 T_3)^2} \tag{4.37}$$

4.5 Comparison of Theoretical and Simulated S-parameters

Once the S-parameters have been de-embedded using the preceding analysis, the parallel results can then be compared to check the validity of the simulated results. Since the desired comparison involves ideal theoretical S-parameters, idealized preliminary simulations are necessary to determine the validity of the waveguide simulations. The following steps are taken to idealize the simulation model:

- The inner wall of the waveguide is made continuous across the waveguide-sample-waveguide junction, replicating a continuous waveguide with the sample inserted directly inside.
- Conductor losses are not taken into account. This step is performed by using a perfectly conducting material for all of the waveguide metallization.

Figures 4-9 and 4-10 show a comparison of the theoretical and simulated S-parameters s_{11} and s_{21}, respectively. It comes as no surprise that the S-parameters from the theoretical and simulated cases nearly match one another. Every simulation run is essentially a theoretical calculation. Maxwell's equations and the necessary boundary conditions are applied to a high-resolution mesh, and solved in individual regions using the finite element method. The mesh is refined until a specified accuracy is obtained. Increased accuracy comes largely at the expense of longer simulation times and the use of more computer resources.

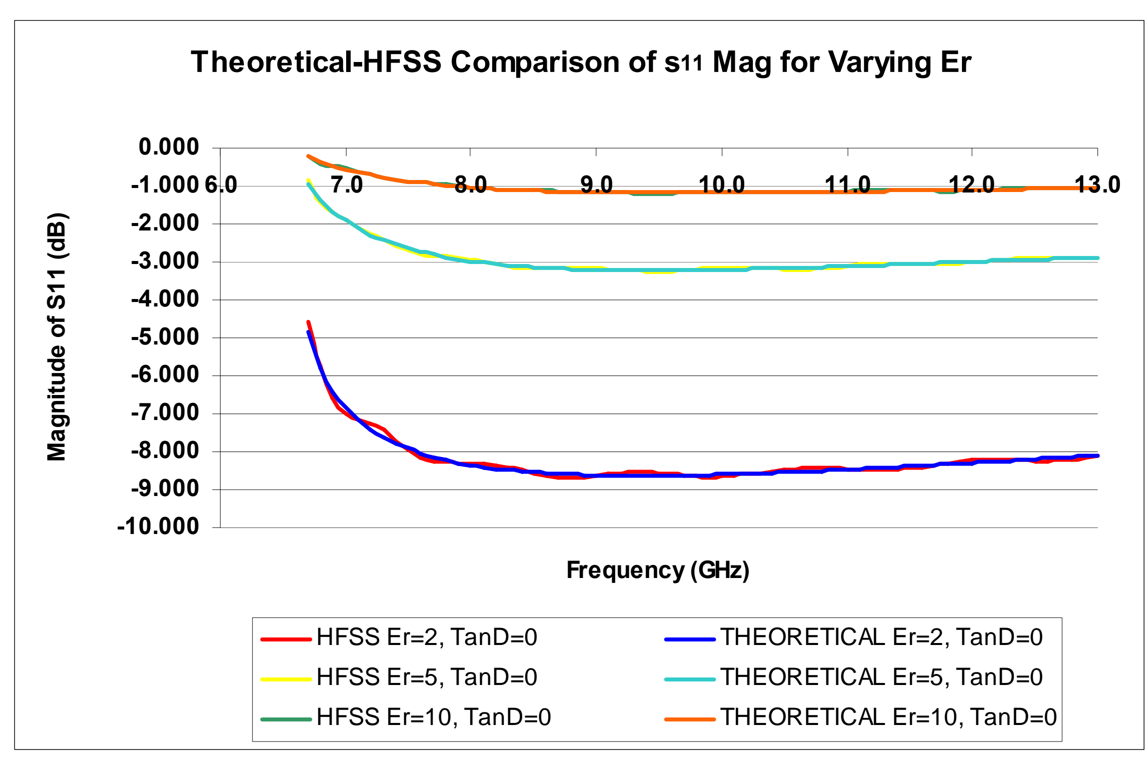

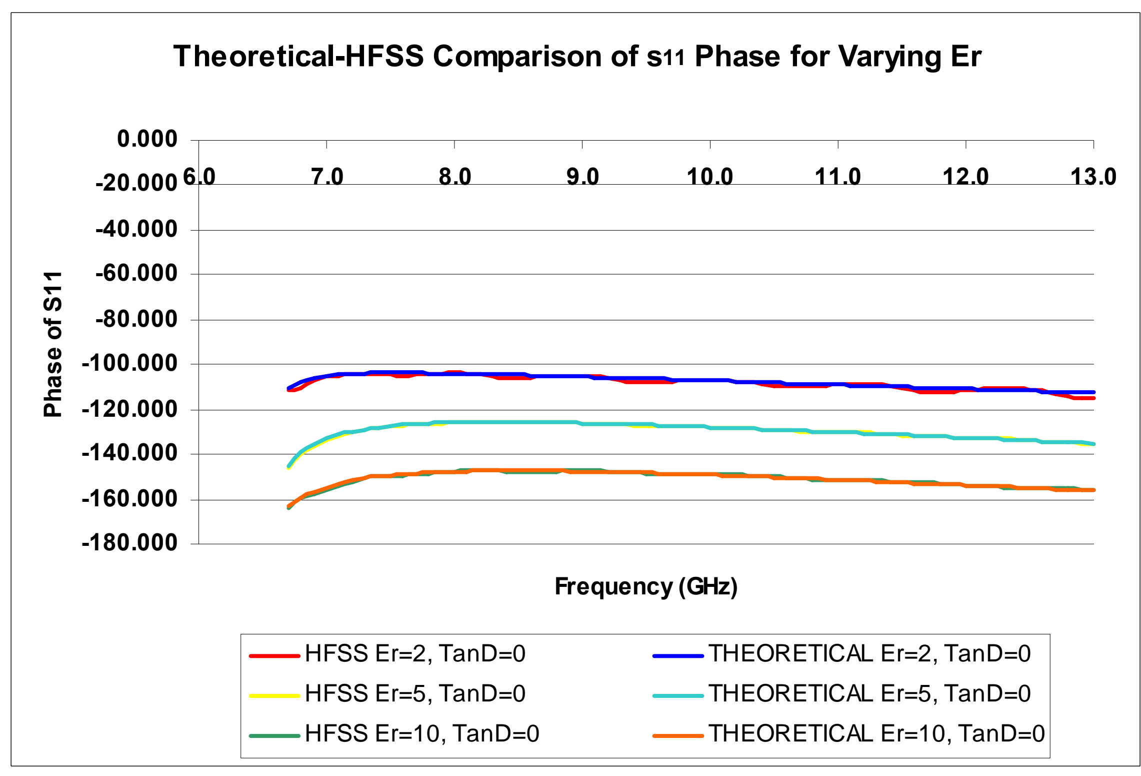

Figure 4-9. Comparison of s_{11} magnitude and phase. The excellent match between theoretical and simulated S-parameters allows confidence to be placed in the electromagnetic simulator.

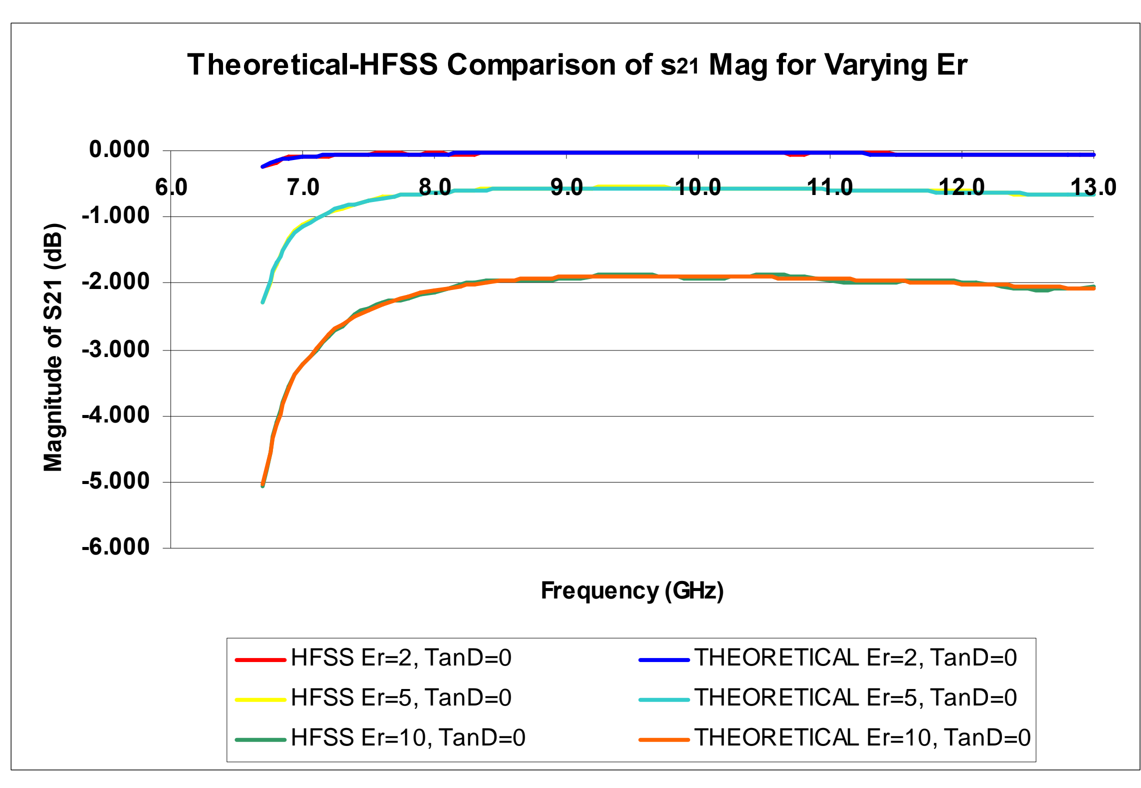

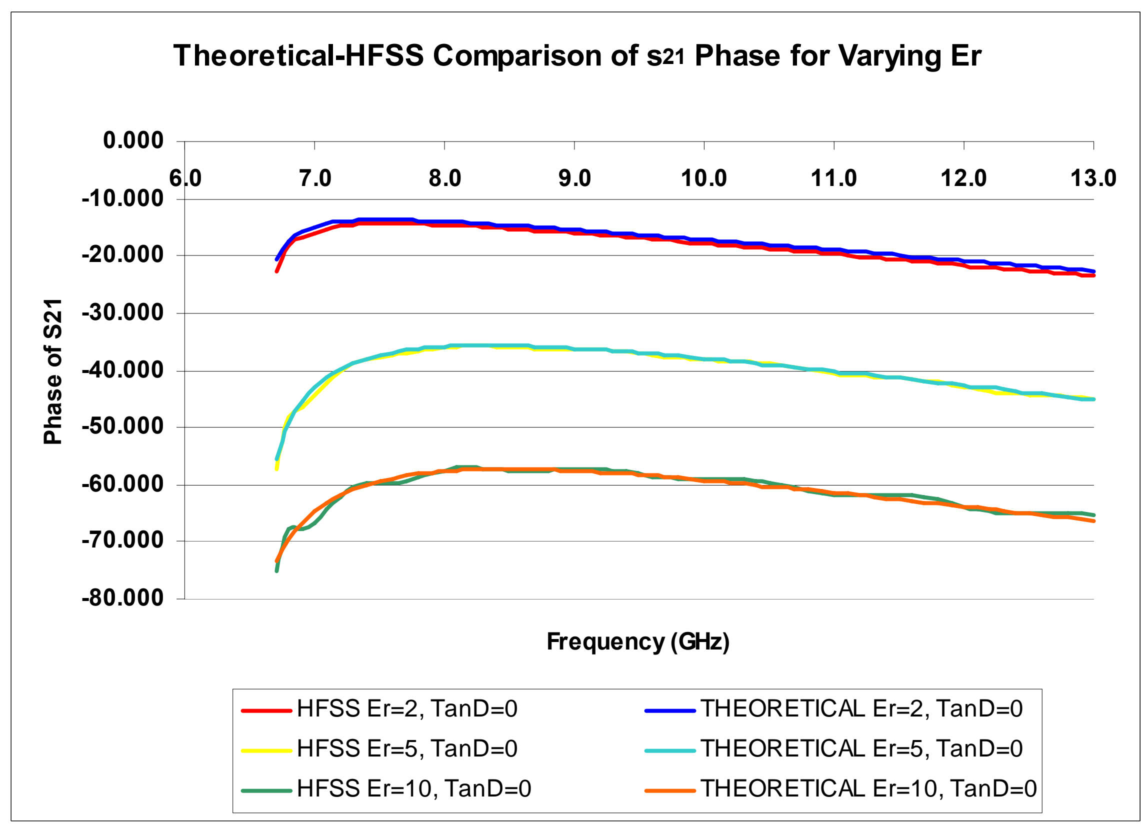

Figure 4-10. Comparison of s_{21} magnitude and phase. The excellent match between theoretical and simulated S-parameters allows confidence to be placed in the electromagnetic simulator.

As the results show, there is a very close match in each case. Having good confidence in the results of the metallic waveguide simulations, the next logical task is finding a precise solution for the ε' and ε'' of the material, based upon a comparison of the observed and theoretical S-parameters.

4.6 Inverse Solution

It is desired to find the ε' and ε'' that correspond to the phase and magnitude of the experimental S-parameters. The determination of these quantities is the primary reason time has been taken to conduct the preceding analysis in the first place, and all of the prior analysis is insignificant if the material values can not be successfully extracted. Therefore, a direct search inverse solution algorithm has been developed to solve for the complex permittivity of the sample.

The straight inverse solution is, essentially, solving the bouncing diagram equations, (4.36) and (4.37), for the ε' and $tan(\delta)$ values that cause the theoretical S-parameters to match the simulated S-parameters s_{11M} and s_{21M}. In other words, the theoretical S-parameter curve is adjusted until it lies on top of the simulated S-parameter curve. This is not exactly our aim, however, since there are inherent differences in the origin of the S-parameters for each case. Since the simulated and theoretical S-parameters do not exactly match one another for equivalent known values of ε' and $tan(\delta)$, these differences, which are generally referred to as systematic errors, must be characterized and removed during the solution process.

One may wonder why errors are considered in the purely theoretical and simulated cases, since error is generally associated with physical measurement discrepancies. The reason is that it does not matter where the error comes from, and it must be dealt with whether it is the result of experimental inaccuracy or simulated disparity.

Once a method has been devised to account for these systematic errors, it can be applied to any situation, whether it is the result of physical or simulated error. For any given situation, a large number of simulations must be run, so the systematic error can be continuously approximated with precision across the entire range of possible solutions.

To accurately and precisely model the systematic error, a large amount of simulations must be run. In this case, it is desired to characterize the error response due to the variation of a large number of variables, including the material thickness, the ε', dielectric loss tangent, sample size, and varying configurations of metallization surrounding the sample region. For each variable of interest, many cases are run, in which the variable of interest presumes a large range of practical values, while all other variables are held constant.

For the following reasons, it is much more convenient to run multiple cases in a 3D electromagnetic simulation environment, than to physically measure a range of materials:

- The exact complex permittivity is not known for a large range of physical materials
- The unavoidable, unrepeatable error resulting from the physical measurement of a large number of materials will be carried all the way through the calculations and adversely affect the final value of calculated complex permittivity.

The 3D EM simulator avoids these problems and has been utilized to run these cases and effectively characterize the systematic error. Every possible combination of the cases in Table 4-2 were run. T_{SAMPLE} represents the sample thickness, while *Conductor* represents the composition of the sample holder.

Table 4-2. Range of material values used to construct the error library.

ε_r'	$\tan(\delta)$	T_{SAMPLE}	*Conductor*
1	0	10mils	Copper
2	0.001	20mils	Brass
3	0.002	30mils	Bronze
4	0.005	40mils	
5	0.01	80mils	
6	0.02		
7	0.05		
8	0.1		
9	0.2		
10	0.5		

For each value in Table 4-2, a case is run with all possible combinations of the other three columns. The total number of cases needed to characterize the systematic error is then

$$N = (E_R)(TAN_D)(T_S)(C) \quad (4.38)$$

E_R = The number of ε_r' values

TAN_D = The number of *tan(δ)* values

T_S = The number of sample thickness values

C = The number of conductor metals

With a set of S-parameters, s_{11M}, s_{21M}, s_{12M}, and s_{22M}, either physically measured, or derived from the electromagnetic simulator, it is desired to determine the unknown scalar values of ε' and *tan(δ)* that correspond to an optimal solution. Since the system is very close to being symmetrical, much of the data for s_{11M} and s_{21M} is repetitive with s_{22M} and s_{12M}, respectively, and s_{22M} and s_{12M} can therefore be ignored in the inverse solution. Since each of the experimental S-parameters represent complex quantities, and the unknown ε' and *tan(δ)* each represent scalar quantities, the problem is thus overstated and there are four known values with only two unknown values. A numerical solver does not know how to handle this type of situation and an optimization routine is required to find the optimal solution. A basic direct search optimization algorithm has been formed to find an optimal solution for every frequency of interest.

The basic routine uses a simple technique to quickly scan the entire range of ε' and *tan(δ)* values for which simulations have been run. At each point the weighted least squares error E is found by applying (4.39),

$$E = E_{|S_{11}|}^2 + E_{\angle S_{11}}^2 + E_{|S_{21}|}^2 + E_{\angle S_{21}}^2 \quad (4.39)$$

where each E represents the normalized error of each S-parameter component. The solver then focuses on the area with the smallest least squares error and scans at a much

higher resolution to find the complex epsilon value that corresponds to an optimal solution.

The optimal solution differs depending on the weighting factor given to each individual error. The S-parameters are broken down into $|s_{11}|$, $|s_{21}|$, $\angle s_{11}$, and $\angle s_{21}$, and the error is calculated for each. Then, depending on the sensitivity of each quantity to changes in ε' and $tan(\delta)$, different weighting factors are applied to the least squares formula.

The specific weight given to each factor is a very complex topic which is only briefly explored in the following section, but a few basic considerations can greatly enhance the solution. For example, when measuring a material with a small expected dielectric constant, we expect the reflection coefficient, s_{11}, to be very small, since ρ decreases drastically with decreasing permittivity. Since the phase of s_{11} may be only slightly larger than the system noise floor of the network analyzer, it can be given a much smaller relative weight when computing the least squares error, thus minimizing its negative effect on the final solution.

The following list of steps outlines the pseudo-code for the solution algorithm used to solve for ε' and $tan(\delta)$:

Initial "Ballpark" Solution

for each frequency:

for each (ε_r' , $tan(\delta)$) point in the error matrix:

(1) Calculate theoretical S-parameters.

(2) Separate parameters into $|s_{11}|$, $|s_{21}|$, $\angle s_{11}$, and $\angle s_{21}$

(3) Apply systematic error to "correct" these S-parameter elements

(4) Calculate error between S-parameters of unknown material and "corrected" theoretical S-parameters for current point

(5) If error is the lowest of all points tested thus far, record it as the "ballpark" solution for the current frequency.

Solution Refinement

for each frequency:

create a modified higher resolution range of points to test in the vicinity of the "ballpark" solution.

for each (ε_r' , *tan(δ)*) in the modified range:

(1) Calculate theoretical S-parameters.

(2) Separate parameters into $|s_{11}|$, $|s_{21}|$, $\angle s_{11}$, and $\angle s_{21}$

(3) Apply **interpolated** systematic error to "correct" these S-parameter elements

(4) Calculate error between S-parameters of unknown material and "corrected" theoretical S-parameters for current point

(5) If error is the lowest of all points tested thus far, record it as the final solution for the current frequency.

Once the loop has finished running, the values of ε_r' and *tan(δ)* that produce the lowest error are taken as the final solution.

When the range of points tested for possible solutions is modified into a higher resolution range, there will be many points for which a simulation has not been run, and the systematic error at these points can not be precisely determined. Therefore, the technique of linear interpolation is utilized.

The interpolated systematic error of a given error matrix is created by averaging the errors of the four nearest points in the (ε' , ε'') error matrix in such a way that the closer points receive a larger weighting and the farther points receive a smaller weighting. The interpolation is linear and assumes that enough cases have been run to provide a good interpolated estimation of the systematic error at any given point.

This interpolation process is performed for the two error matrices corresponding to sample thicknesses on either side of the unknown sample's thickness. For example, consider a situation in which the material under test is 35 mils thick and error matrices exist only for samples with thicknesses of 20 mils and 40 mils. Since the systematic error changes as a result of the different sample thickness configuration and no error data exists for the case of a 35-mil thick sample, the error must once again be interpolated. The

interpolated errors of the two matrices are averaged together with the error from the 40-mil matrix receiving a larger weighting, since the 35 mil sample thickness is closer to 40 mils than 20 mils.

Figure 4-11 illustrates the optimization routine in graphical form:

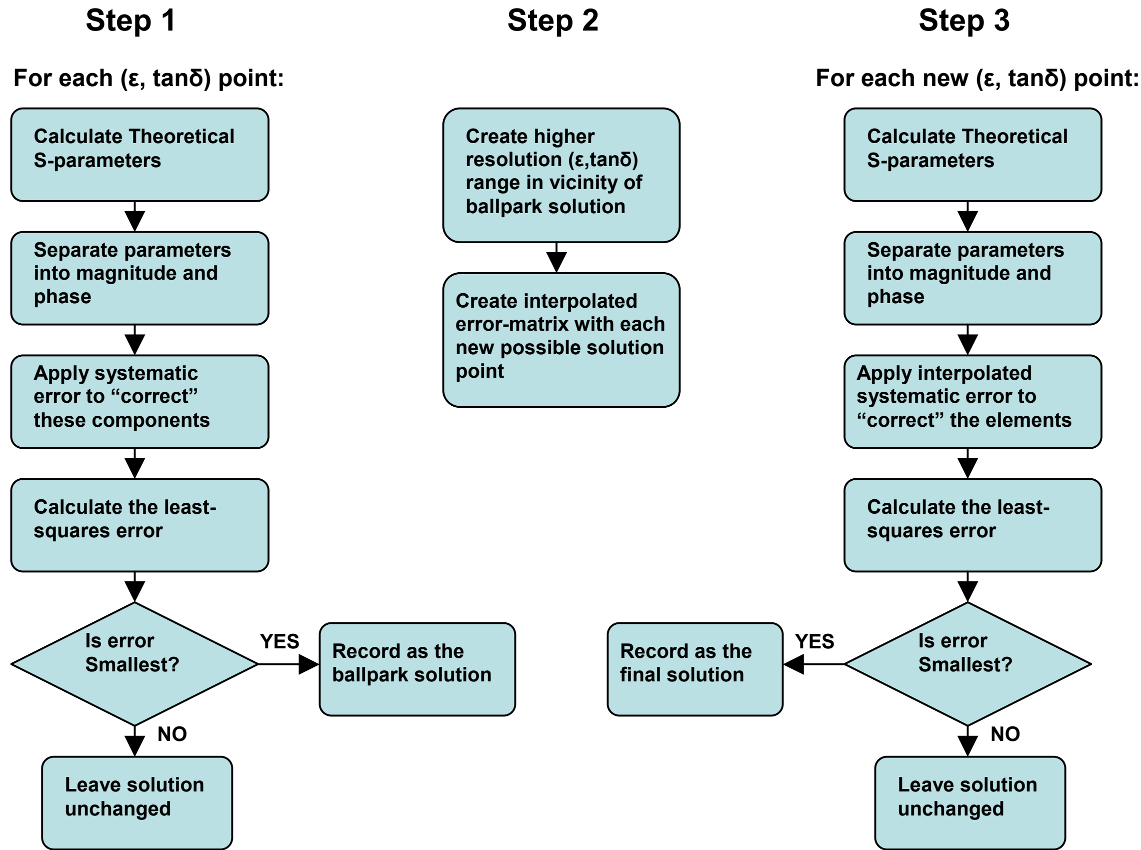

Figure 4-11. The optimization routine. Using the method presented in the flow chart, the inverse solution can be found.

The optimization routine can be tested by running a simulation with known epsilon and tan delta values and then analyzing the resulting S-parameters as if the dielectric constant and loss tangent are unknowns. By running a sufficient number of cases with this method, then comparing the solution to the original permittivity of the sample, the validity of the optimization method can be analyzed.

A sample case was run in the Ansoft HFSS high-frequency structure simulator by setting ε'=5.25 and $tan(\delta)$=0.017, then running a simulation. Next, the inverse solution

code was run in MATLAB®. Using the optimization routine with the resulting simulation data resulted in the solution shown in Figures 4-12 and 4-13. Once the measurement frequency is extended above the waveguide cutoff frequency of approximately 6.7GHz (data below the 6.7GHz cutoff frequency is not of concern), the resulting solution is extremely close to the expected value:

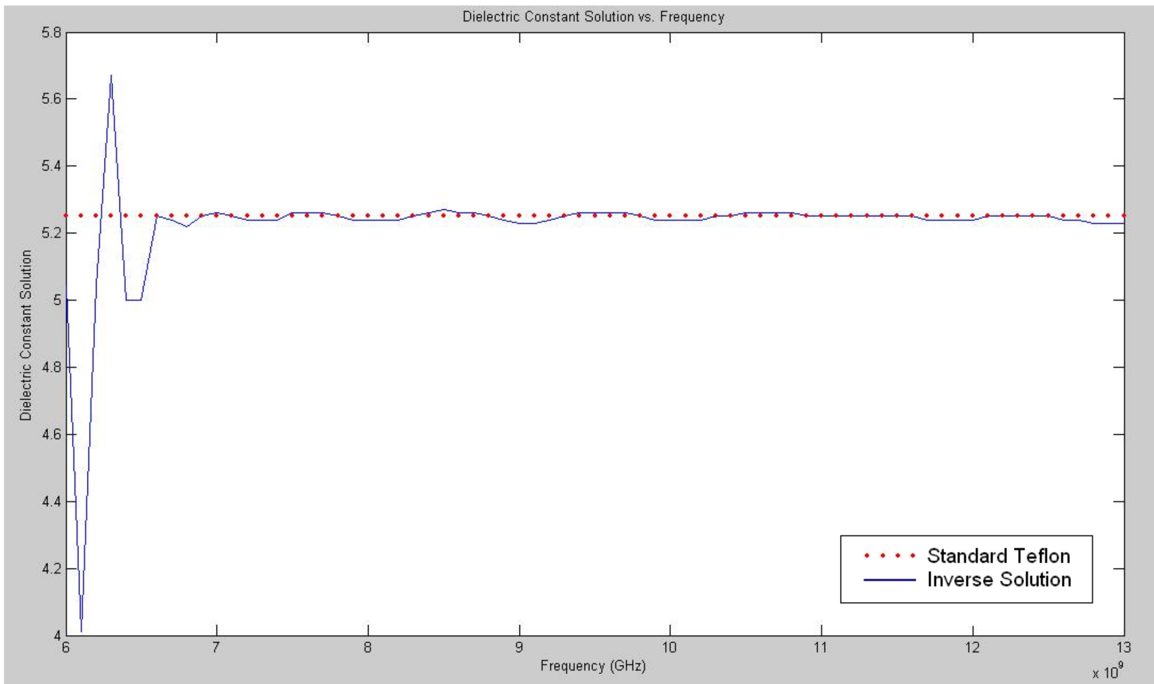

Figure 4-12. Results from produced by the inverse solution for the dielectric constant. When solving with the data from an unknown simulated case, the solution algorithm is highly effective.

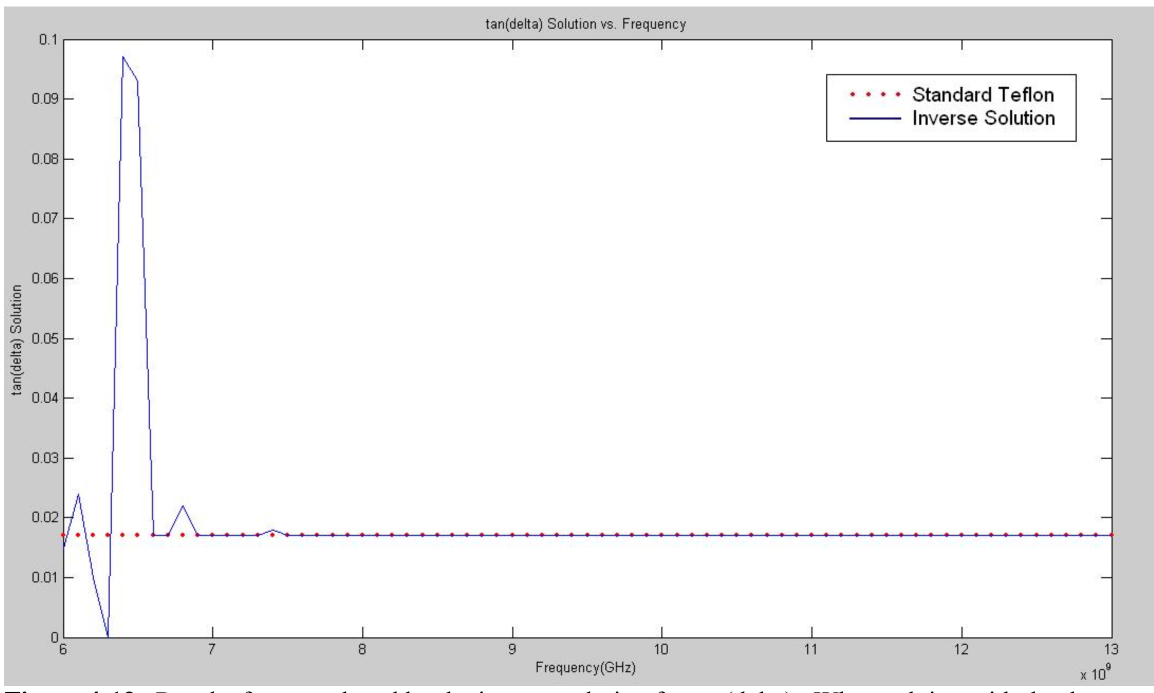

Figure 4-13. Results from produced by the inverse solution for tan(delta). When solving with the data from an unknown simulated case, the solution algorithm is highly effective.

As the results show, a very good match is obtained and the solution method is validated. Problems are encountered, however, when an actual material is measured, as is seen in the following sections.

4.7 Sensitivity Analysis

Attention is now focused on the effect that a slight change in material property has on each individual S-parameter component. This is done by conducting sensitivity analysis, which is a helpful practice in determining which S-parameter components are the most sensitive to changes in material properties under certain conditions. Once the more sensitive factors are known, they can be given more weight in the inverse solution process.

For this thesis, simple sensitivity analysis was carried out by observing the changes in S-parameters to slight variations in the complex permittivity. Figures 4-14 through 4-17 clarify this idea. For a range of permittivity values, with $tan(\delta)$ held at a constant value, the theoretical change in the magnitude and phase of the material S-parameters is observed for a 0.1 change in ε_r. This is performed for differing values of $tan(\delta)$, since the sensitivity will differ depending on material losses.

Next, the effect of small changes in *tan(δ)* are observed as the value of ε_r is held constant. As with the former case, the sensitivity is highly dependent upon the dielectric constant, so cases must be run for differing values of relative permittivity.

Sensitivity of *Δεr* = 0.1 with *tan(δ)* = 0.005, T=40mils

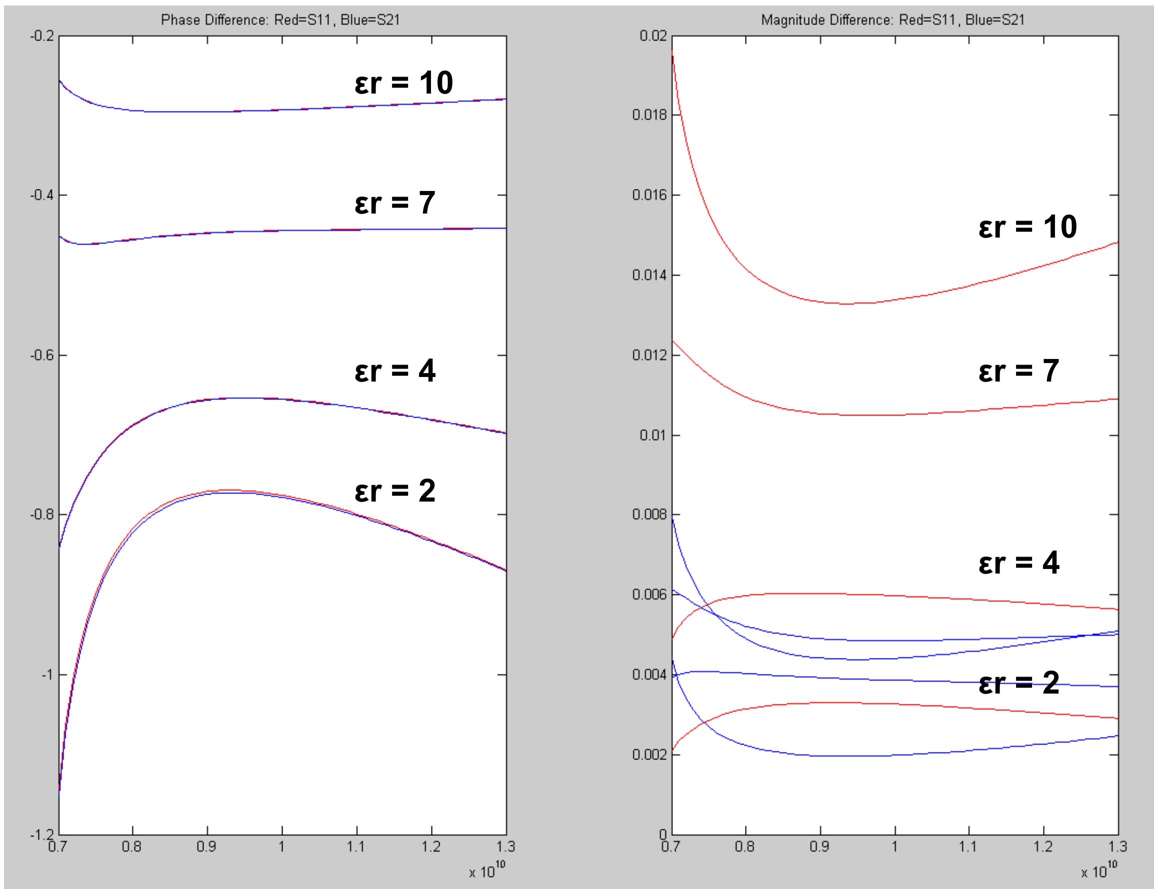

Figure 4-14. $\Delta\varepsilon r$ sensitivity for low-loss dielectrics.

For low-loss dielectrics, the phase of s_{11} and s_{21} are both equally sensitive to small changes in ε'. The magnitude of s_{11}, however is much more responsive to changes in ε' than s_{21}.

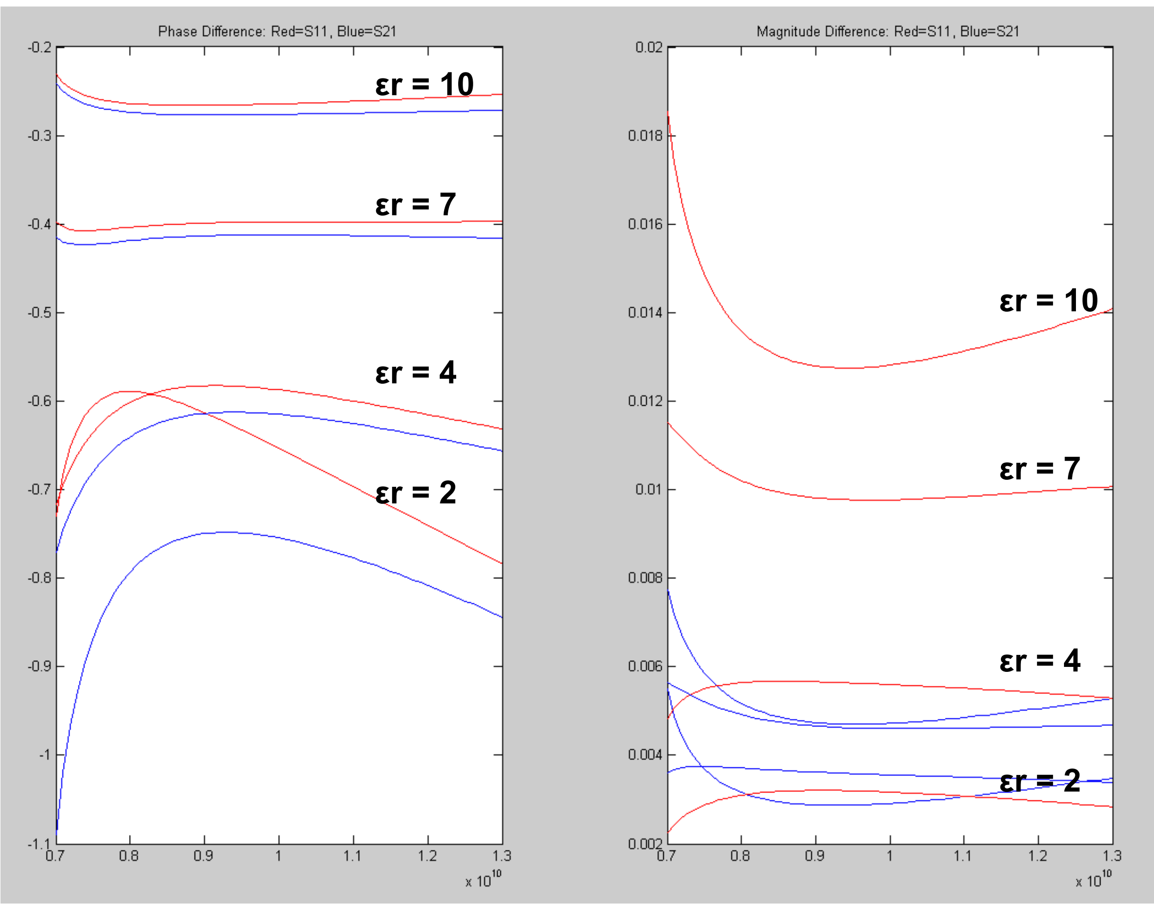

Figure 4-15. Δ*εr* sensitivity for high-loss dielectrics.

As the loss tangent of the dielectric changes, it is clear that the magnitude sensitivity of s_{11} and s_{21} stays constant with small changes in ε', and the use of the magnitude of s_{11} is still preferable to that of s_{21}. This can be seen by comparing Figures 4-14 and 4-15 and noting that the graphs maintain almost the exact same shape. The phase sensitivity of s_{11}, however, becomes less sensitive to ε' changes as the loss tangent increases, while that of s_{21} remains the same. Therefore, for ε' determination, it is usually better to weight the phase of s_{21} higher than s_{11}, regardless of the material properties.

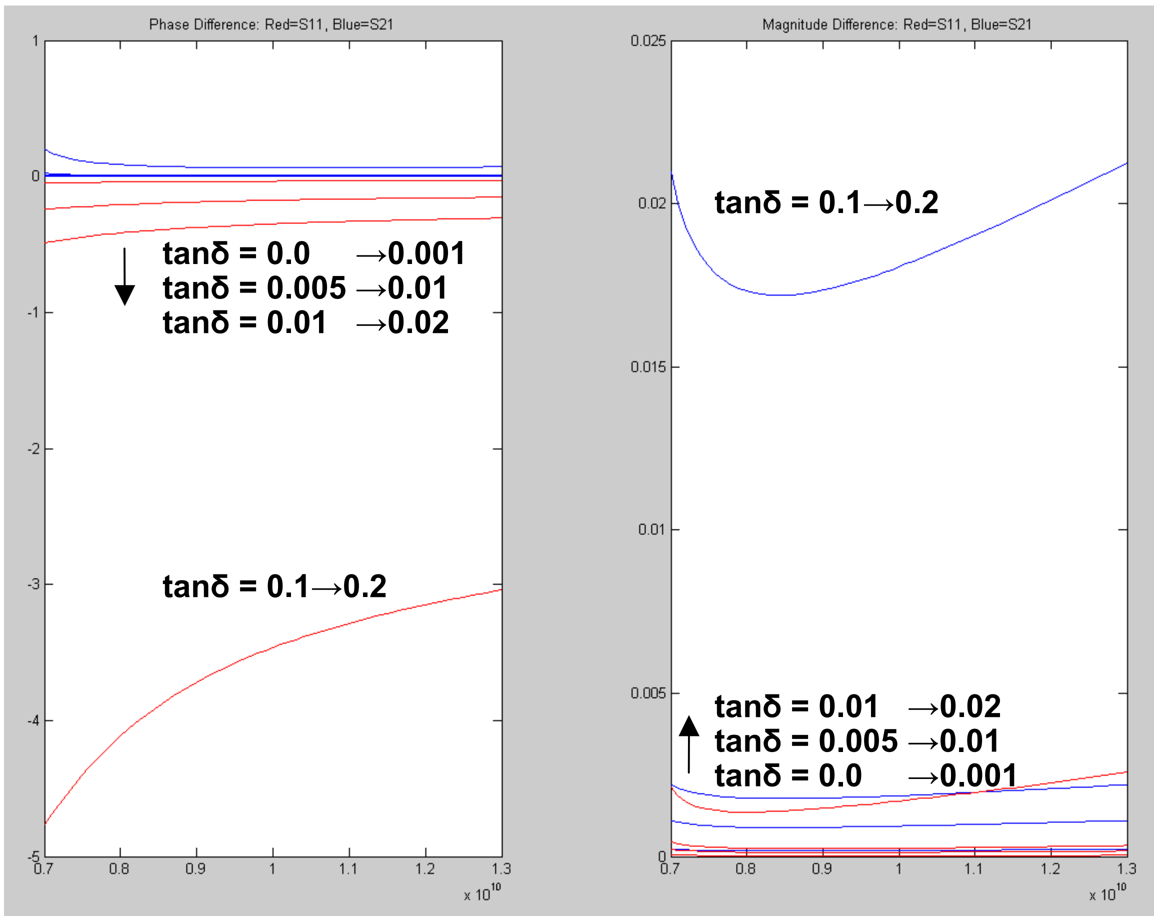

Figure 4-16. Δ*tan(δ)* sensitivity for low-*εr* dielectrics.

Next, the sensitivity of the dielectric loss tangent is examined. This case turns out to be almost the exact opposite of the $\Delta\varepsilon$ case, as Figures 4-16 and 4-17 show. For the case of a low- ε' dielectric, the phase of s_{11} is much more sensitive than that of s_{21}. The magnitude of s_{21} is affected more by subtle variations in *tan(δ)* than s_{11}. Note that the phase of s_{21} changes in the opposite direction as the phase of s_{11}. This fact may prove to be useful when attempting to find the optimal solution.

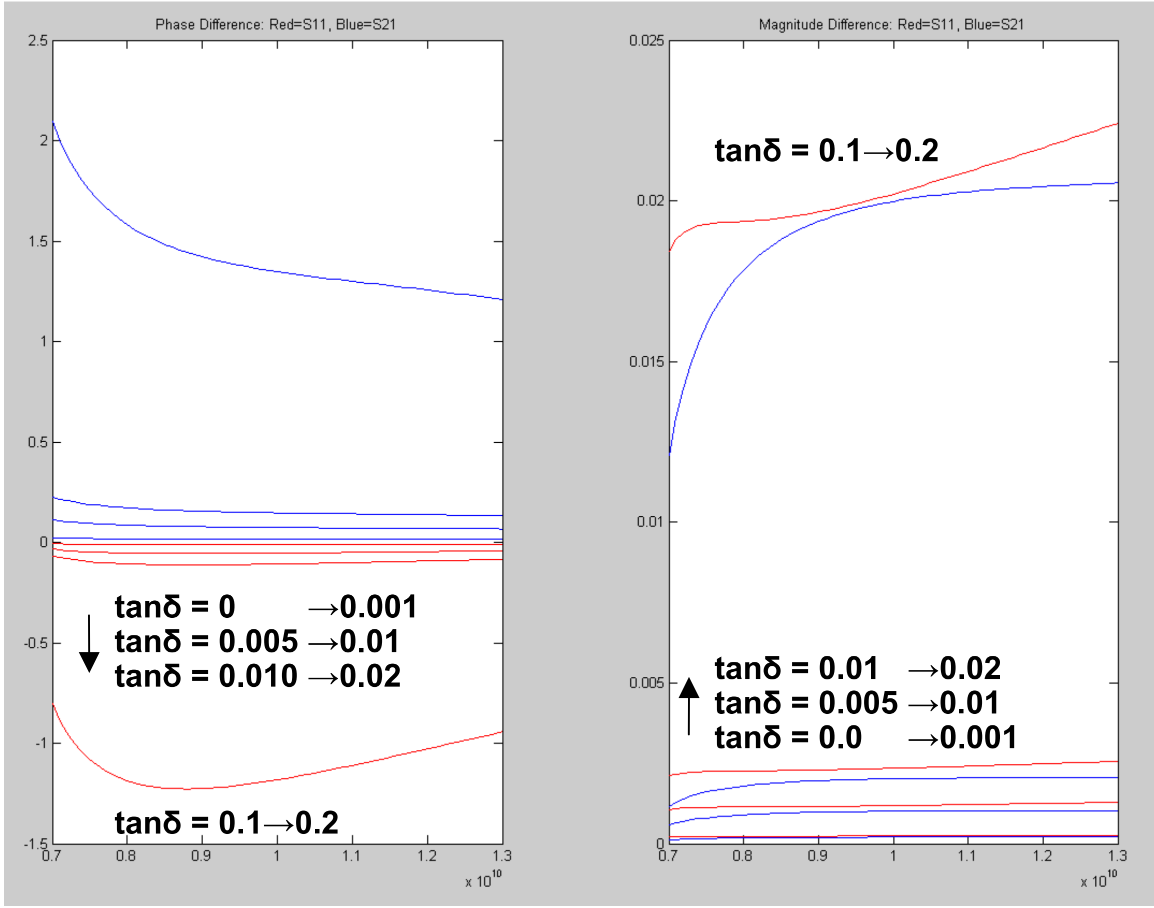

Figure 4-17. *Δtan(δ)* sensitivity for high-*εr* dielectrics.

As the dielectric constant of the material increases, the sensitivity of s_{11} and s_{21} begin to approach the same level. Therefore, it can be said that the choice between s_{11} and s_{21} becomes less significant in *tan(δ)* determination as the dielectric constant increases.

When materials are measured, the dielectric loss tangent is sometimes desired to be known to an accuracy of three or more decimal places. By monitoring the absolute change in the S-parameters corresponding to small changes in *tan(δ)*, however, it is seen why this accuracy becomes so difficult to achieve. Phase changes of a small fraction of a degree and trifling magnitude changes give poor dynamic range for *tan(δ)* measurements in low-loss dielectrics. Another problem sometimes encountered is that a high desired *tan(δ)* resolution can sometimes correspond to a sensitivity that is on the order of network analyzer calibration errors.

The next phase is the measurement and analysis of a sample with unknown electrical properties. After taking measurements on the sample, the measured results are compared to the theoretical and simulated cases.

4.8 Material Measurement

Up until this point, all of the work done was purely theoretical with only the 3D electromagnetic simulations to draw comparisons with. The next phase of the work involved using the 8510C vector network analyzer to test the method with a "real-world" material.

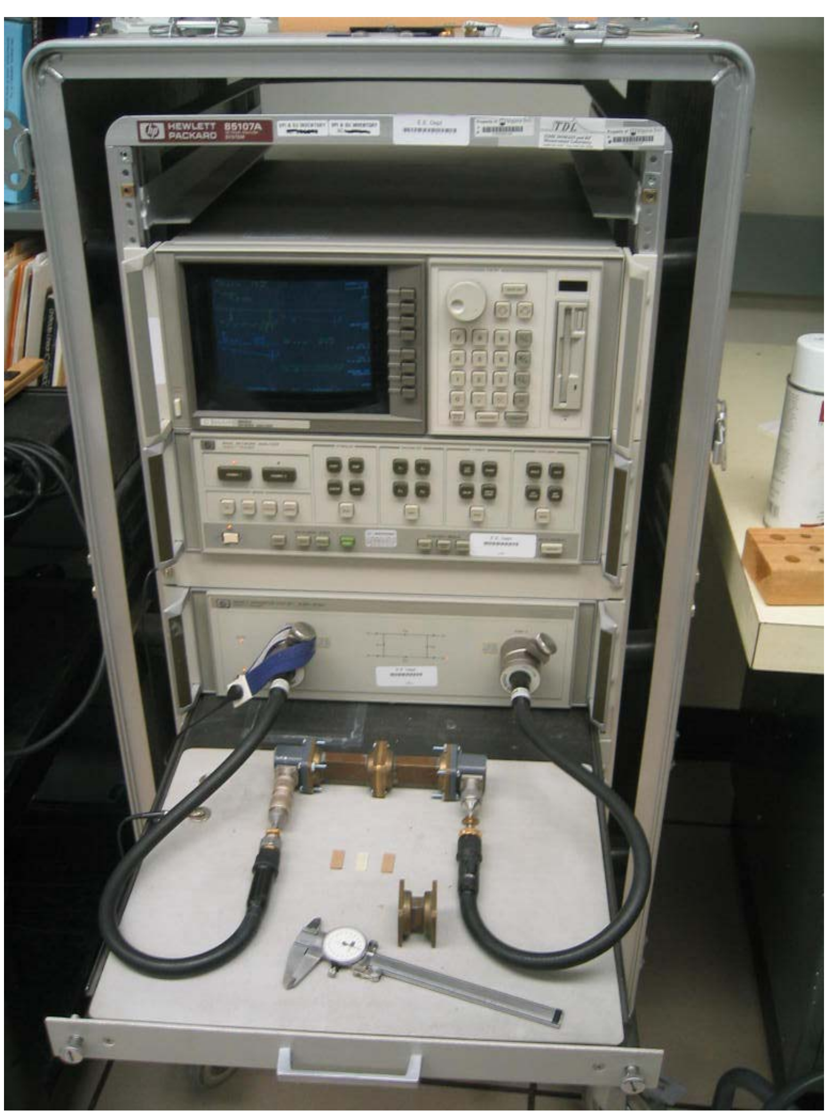

Figure 4-18. The HP 8510C Vector Network Analyzer (VNA). The measured S-parameters are transferred to a computer, where the matlab code is run to solve for the complex permittivity.

4.8.1 VNA TRL Calibration

In order to measure the S-parameters of the material under test, a calibration is required to relate the measured S-parameters to the actual S-parameters of the sample [32]. Many forms of calibration, including TRM, TRL, OSL, RTL, RL^2, response and isolation, and sliding load, are commonly used, all of which rely on the widely used 12-term error model [32]. The preferred method of calibration is highly-dependent upon the specific system topology and can vary greatly depending upon the application.

A broadband match is very difficult to achieve in the waveguide topology, making TRM calibrations very difficult. A line extension, on the other hand, is straightforward to implement. As a result, the TRL calibration is accepted as a very effective technique for rectangular waveguide applications, due to the well-defined reference plane, and has therefore been used for all waveguide measurements in this thesis.

When performing a TRL calibration, the exact impedance of the waveguide does not need to be specifically known, yet the waveguide impedance becomes the reference impedance of the system [32]. The reference plane at the waveguide flange is very well defined, allowing the exact location of the reference plane to be identified. In an application such as dielectric measurement, a well-defined reference plane is a critical feature, since minute unintentional adjustments in the reference plane can substantially affect the solution.

The TRL calibration is performed by taking a series of 2-port measurements:

- The *thru* standard is simply defined as a direction connection of the two measurement reference planes. The *thru* is assumed to be of zero length and typically defines the system reference plane.
- The *reflection* standard, which is usually in the form of an open or short-circuit termination, is measured separately on each port.
- The *line* standard is connected between the two reference planes. All data at frequencies for which the length of the *line* standard is within ±20 degrees of a multiple of $\lambda_g/2$ is typically discarded.

Figure 4-19. The TRL calibration process. After connecting the thru, reflect, line, and isolation standards, the network analyzer computes the 12 error coefficients for direct viewing of S-parameters.

Finally, forward and reverse isolation measurements are performed by placing a matched termination on ports 1 and 2, respectively. This eliminates measurement error due to the internal crosstalk between ports 1 and 2.

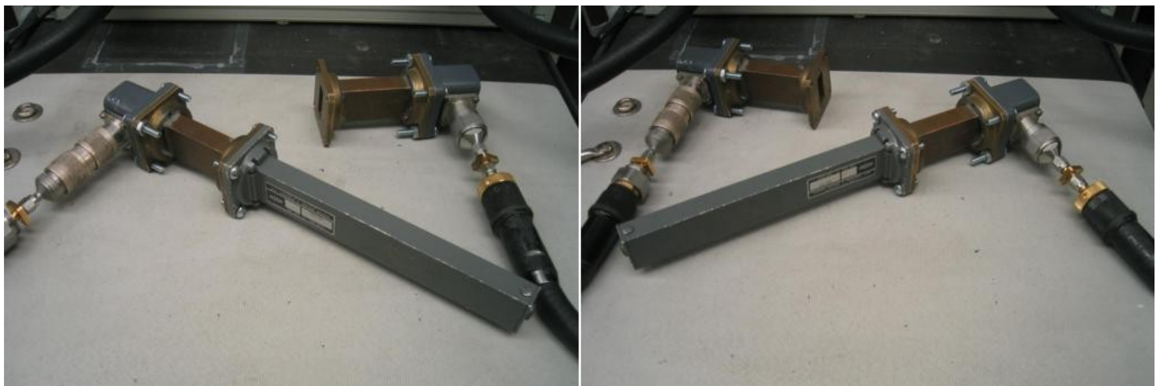

Figure 4-20. Forward and reverse-isolation measurements. The error due to internal crosstalk between ports 1 and 2 is removed by measuring channel isolation.

4.8.2 Sample Preparation

Extreme care must be taken as the sample is prepared by cutting it to fit firmly inside the cross-section of the waveguide sample-holder. The sample should not be so large that it compresses when inserted into the waveguide, but should also fit tight enough so that no air gaps exist between it and the broadside wall of the waveguide. As discussed previously, air gaps between the sample and broadside wall of the waveguide are extremely undesirable, since the electric field is strong in this region and is directed normal to the metal-material boundary.

After being carefully cut and shaved, the sample is lightly pressed into the sample holder, as shown in Figure 4-21. Out of the four measured S-parameters, only the phase

of s_{11} and s_{22} are significantly affected by the exact location of the sample in the sample-holder. The effect of sample location upon all of the other parameters is typically on the order of the network analyzer resolution, and can be neglected. Therefore, the phase of s_{11} and s_{22} can only be used if the location of the sample is known. A simple solution is to secure the sample in the sample-holder by pressing it to one side of the sample-holder.

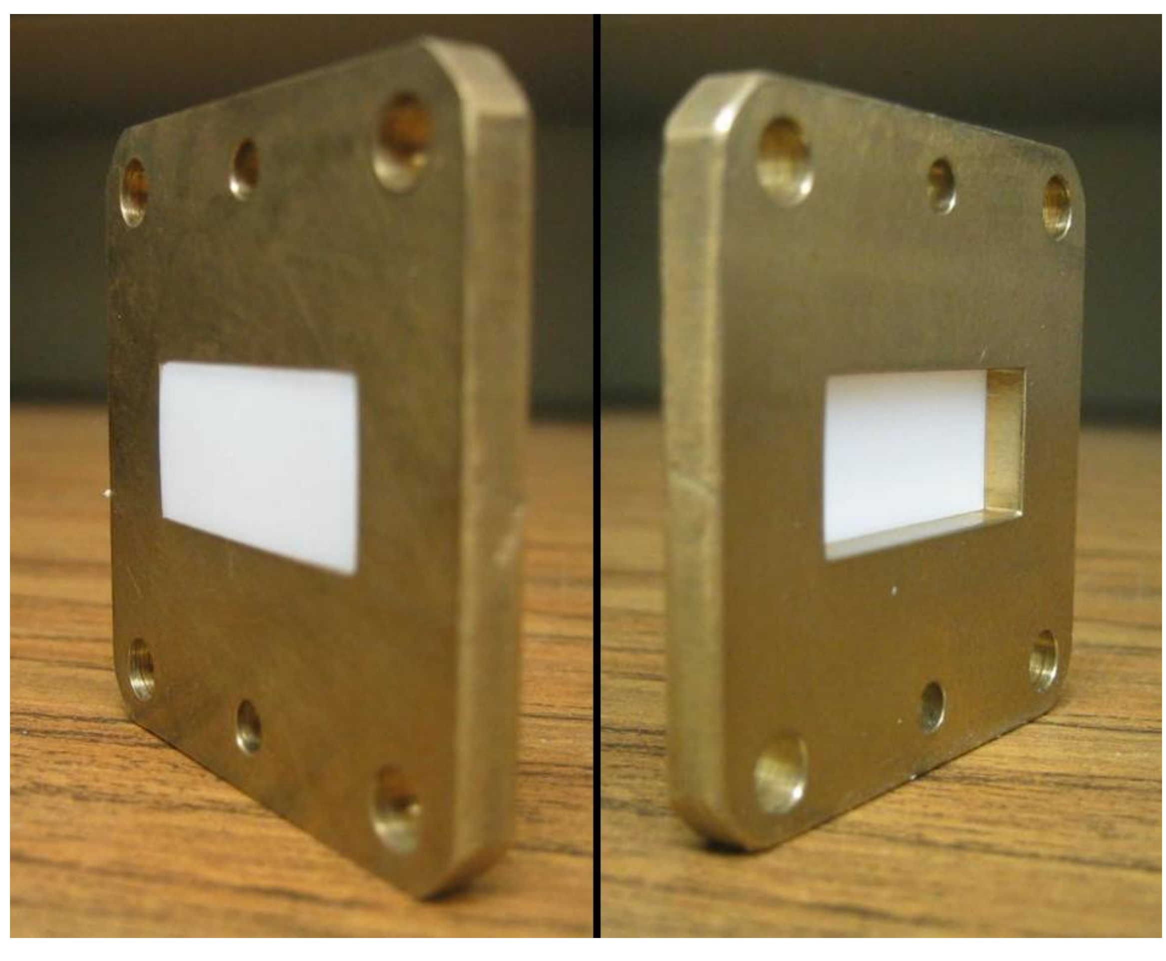

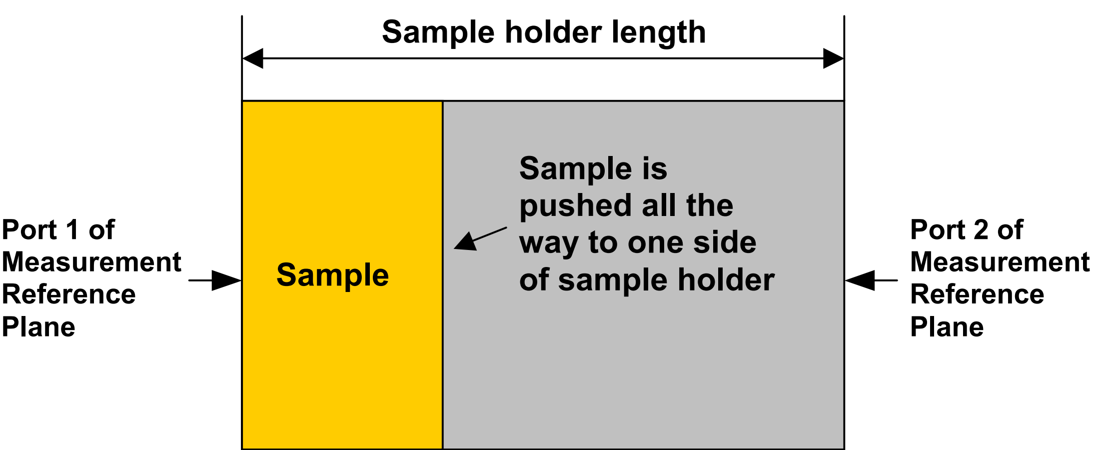

Figure 4-21. Side view of material-filled sample holder. The sample is securely placed on one side of the sample holder to allow for more precise placement and eliminate location ambiguity.

4.8.3 8510C Measurement

Upon successful completion of the waveguide calibration, the S-parameters of the material can then be measured directly. The de-embedding of parameters is unnecessary, since the network analyzer is calibrated at the reference plane of the material. This is contrary to the simulated case, in which there is no simple way of placing the excitation directly at the reference plane of the material under test, and the de-embedding of the S-parameters for the material was therefore required.

The 8510C gives the choice of extracting raw data, unformatted S-parameters, or formatted S-parameters. For our application, only the unformatted S-parameters, which are given as a real and imaginary part in citifile ASCII format, are of interest. The data from direct measurement of the Teflon sample is shown in Figures 4-22 through 4-25, and is compared with the expected theoretical values of a typical Teflon sample with ε_r = 2.1 and $tan(\delta)$ = 0.005.

4.8.4 Measurement Data

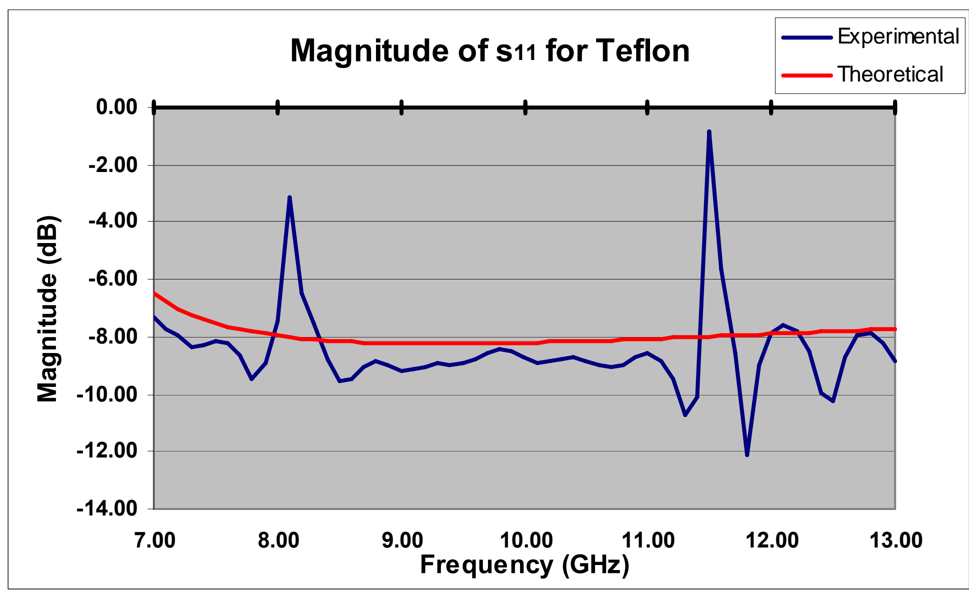

Figure 4-22. Magnitude of s_{11} resulting from a measurement of the Teflon sample inserted in the sample holder.

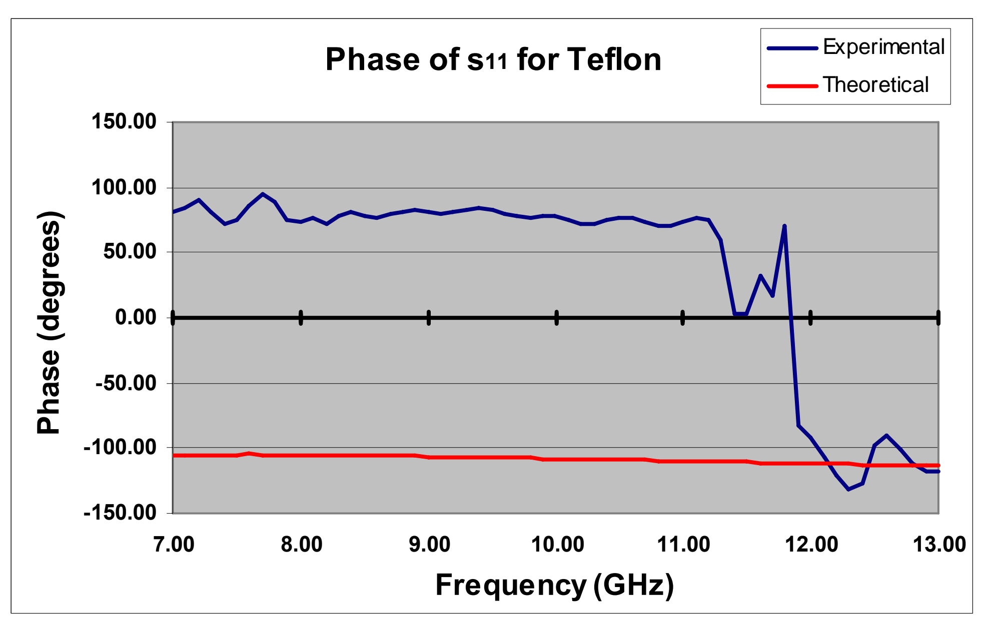

Figure 4-23. Phase of s_{11} resulting from a measurement of the Teflon sample inserted in the sample holder.

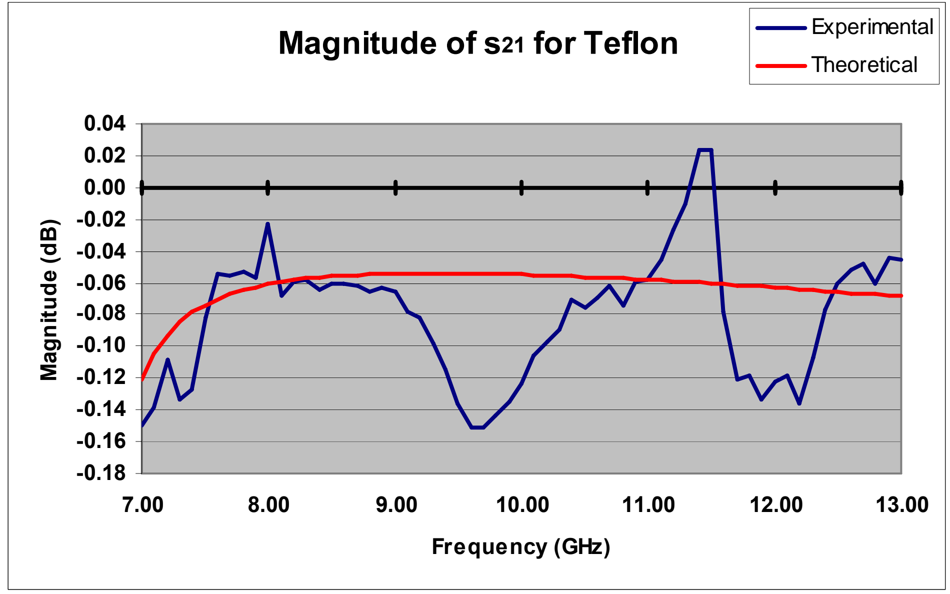

Figure 4-24. Magnitude of s_{21} resulting from a measurement of the Teflon sample inserted in the sample holder.

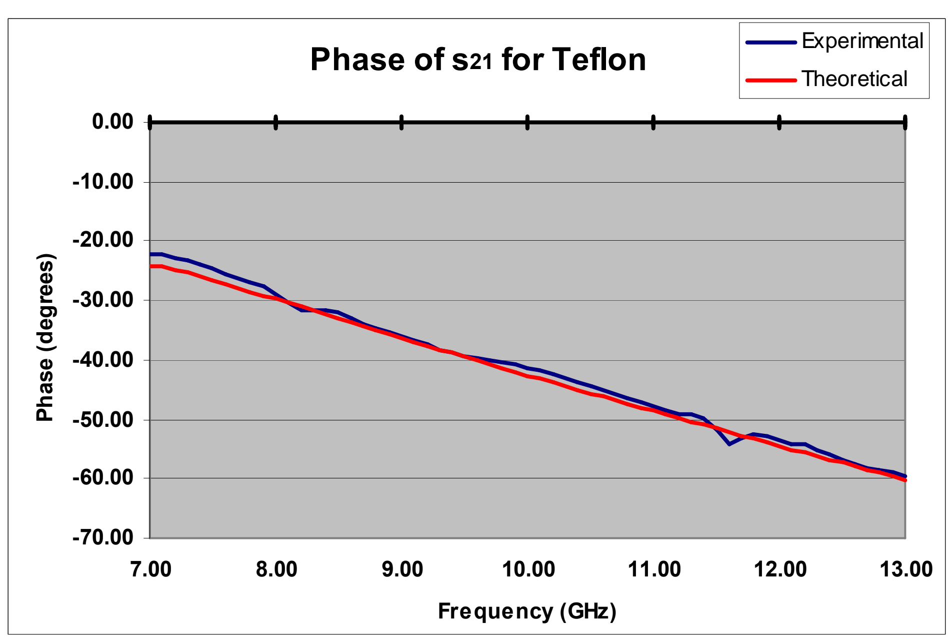

Figure 4-25. Phase of s_{21} resulting from a measurement of the Teflon sample inserted in the sample holder.

A comparison of the experimental S-parameters with the theoretical parameters shows similar results for the magnitude of s_{11} and the phase of s_{21}. The offsets, if shown to be repeatable, can be characterized and removed as systematic errors. The magnitude graph of s_{21}, however, shows a less exact match between the theoretical and experimental results, and unknown resonances appear in the measurement. For the phase of s_{11}, a 180-degree offset exists for frequencies below 11.5GHz. This is most likely the result of a calibration error. The high sensitivity of the solution to slight variations in magnitude and phase cause steep errors in the loss tangent solution, as seen in Figure 4-29. Further development must be done to mitigate these errors.

The quality of the calibration can be gauged by connecting a known standard, and checking to see how close the measurement is to the expected value. In this case, the waveguide *thru'* was reconnected. The deviation from the expected value of $s_{21} = 1\angle 0$ is observed in Figures 4-26 and 4-27. This error is partially due to the flange tightness and imperfections at the interface of the waveguide sections, but regardless of the cause, it will have an adverse affect on the computed complex permittivity. Extended analysis has not performed in this work, but if this error is shown to be repeatable, it may be possible to negate the effect of calibration errors upon the measurement.

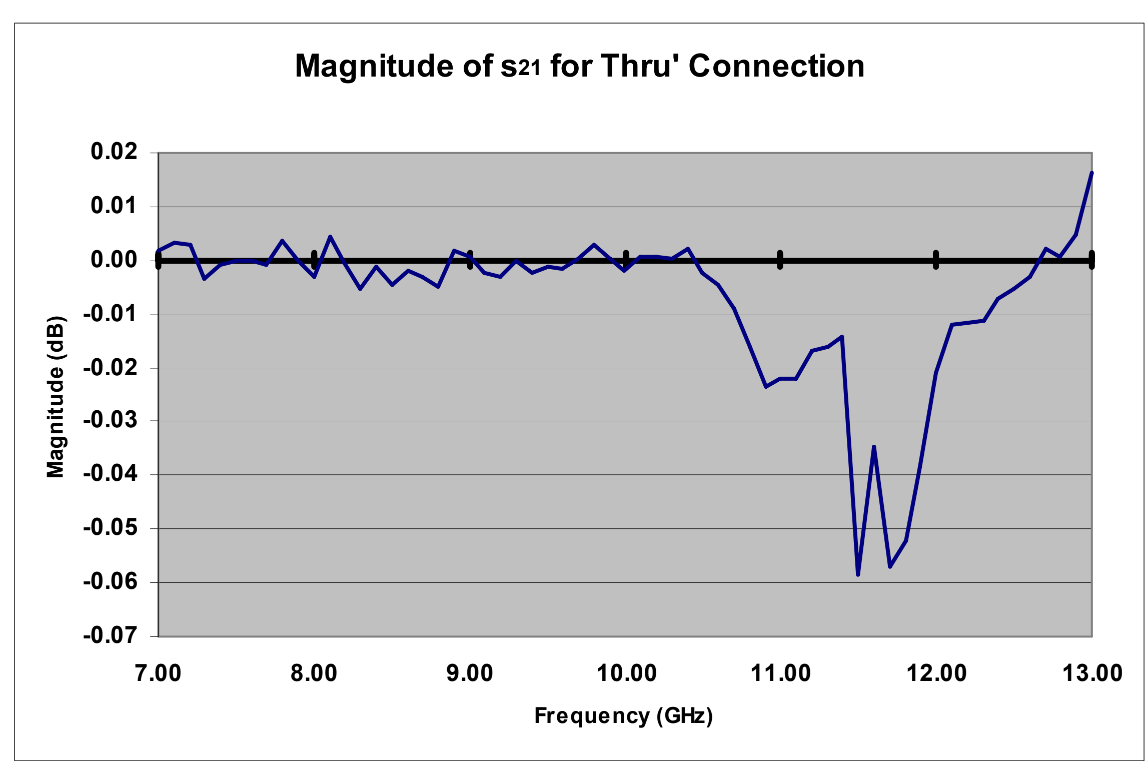

Figure 4-26. Magnitude of s_{21} resulting from a direct connection of the launcher sections.

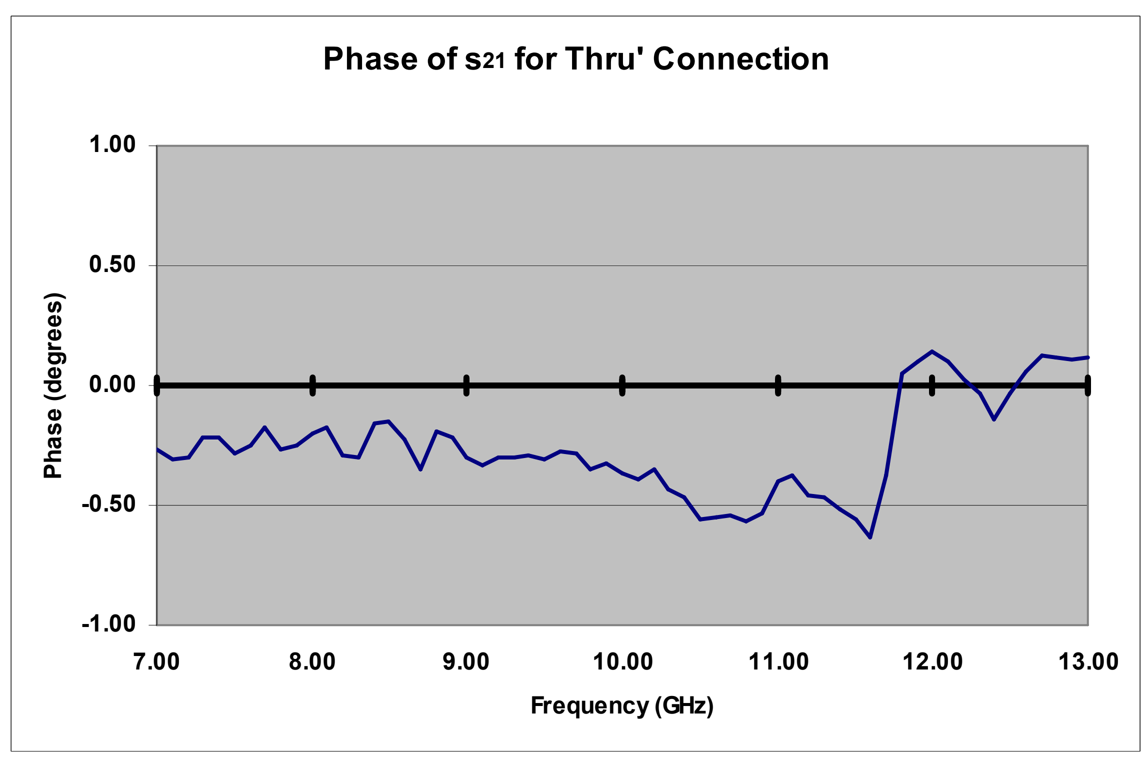

Figure 4-27. Phase of s_{21} resulting from a direct connection of the launcher sections.

4.8.5 Measurement Solution

Using the direct search inverse solution algorithm, the measured data was plugged into the matlab code to solve for the complex dielectric constant. The resulting dielectric constant solution is shown in Figure 4-28, while the loss tangent solution is shown in Figure 4-29.

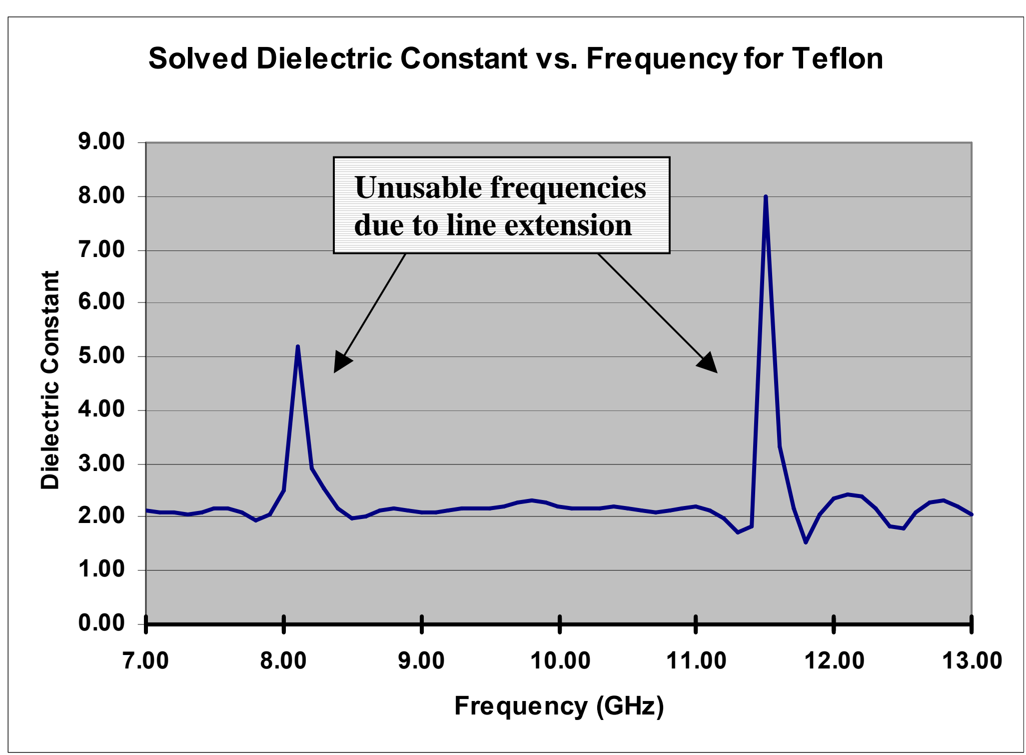

Figure 4-28. Dielectric constant solution vs. frequency.

The *line* standard used for the TRL calibration was 1,235 mils in length. Since this *line* length is longer than the previously calculated maximum of 555 mils, there are two frequencies, 8.1GHz and 11.5GHz, for which the length of the “line” standard is a multiple of $\lambda_G/2$, and the TRL calibration is therefore invalid in these regions.

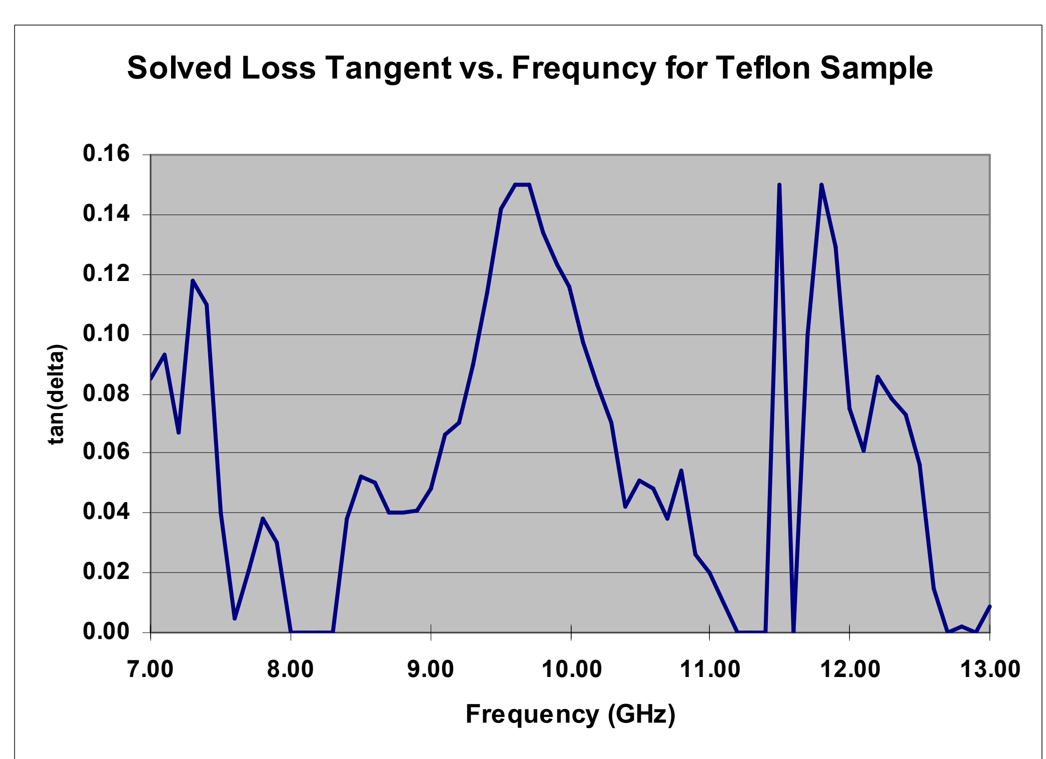

Figure 4-29. Loss tangent solution vs. frequency.

A measured error of less than 5% is achieved for the dielectric constant from 8.5-11GHz, but further development must be performed to remove the anomaly in the loss tangent solution. Due to the high system sensitivity, the sensitivity analysis needs to be expanded, possibly using different S-parameter components for the solution of different material properties.

Using an HP 11644 TRL calibration kit, the same Teflon sample and sample holder were measured. By running the inverse solution algorithm on the measured S-parameters, the dielectric constant and loss tangent solutions of Figures 4-30 and 4-31 were obtained.

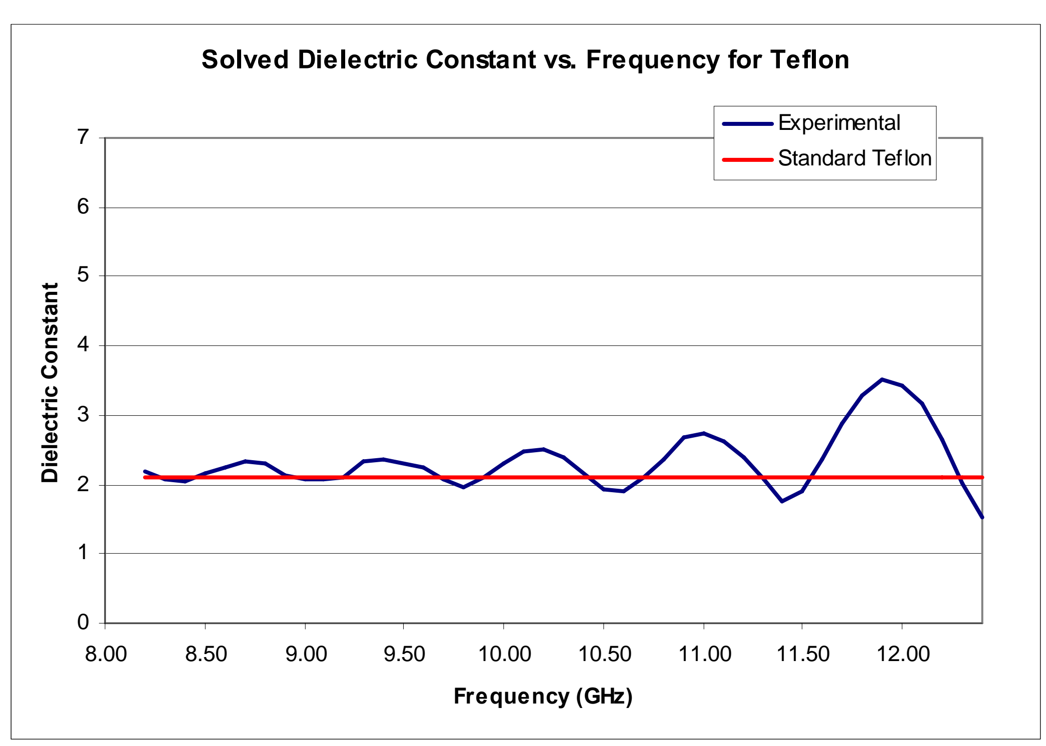

Figure 4-30. Dielectric constant solution vs. frequency for Teflon sample. The previously-measured Teflon sample was re-measured with a separate calibration kit and network analyzer.

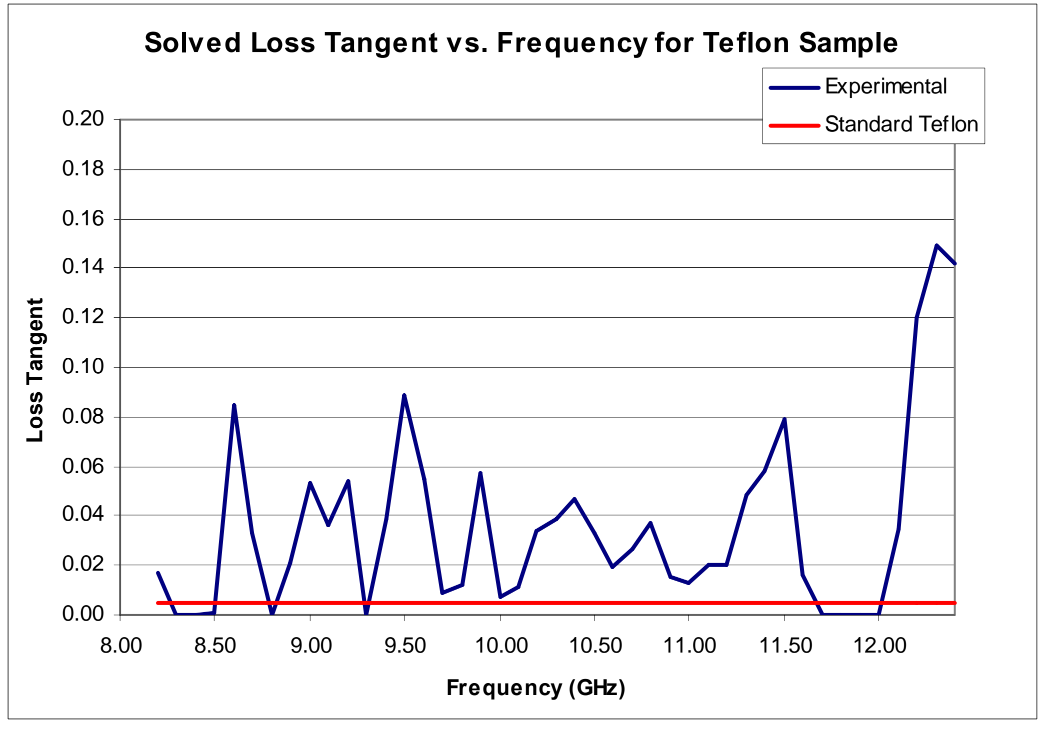

Figure 4-31. Loss tangent solution vs. frequency for Teflon sample. The previously-measured Teflon sample was re-measured with a separate calibration kit and network analyzer.

Finally, a PCB sample of thickness 30 mils was cut to the same dimensions as the waveguide cross-section and then measured. The resulting dielectric constant and loss tangent solutions are shown in Figures 3-32 and 3-33, respectively. For comparison, the stated material properties of $\varepsilon_r' = 3.2$ and $tan(\delta) = 0.003$ are shown.

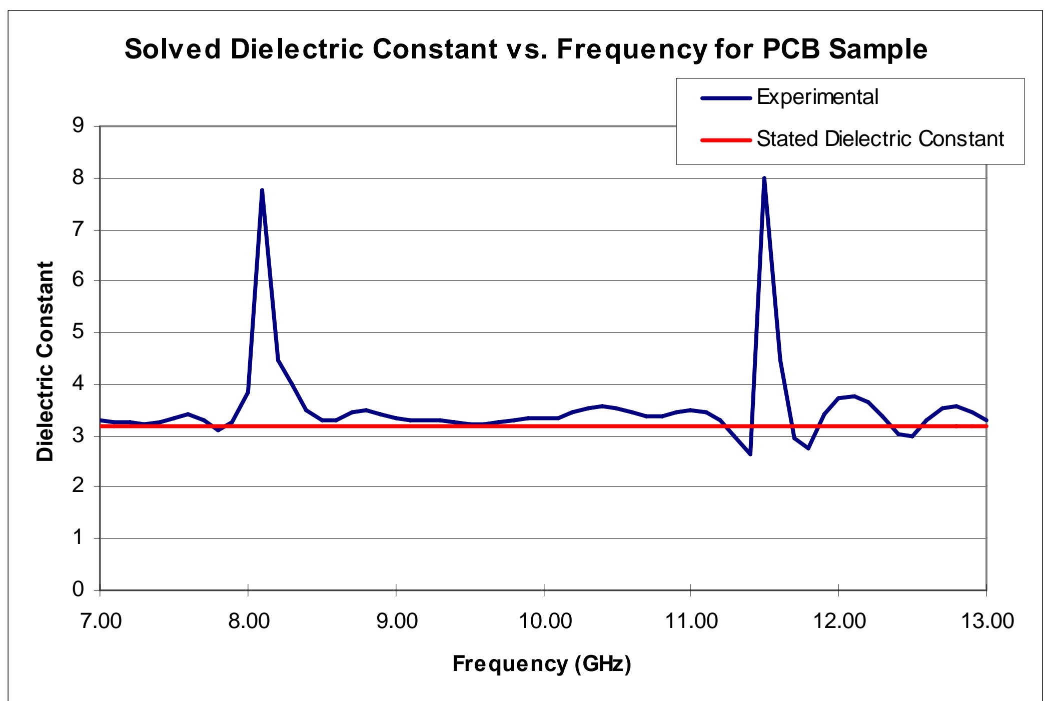

Figure 4-32. Dielectric constant solution vs. frequency for PCB sample.

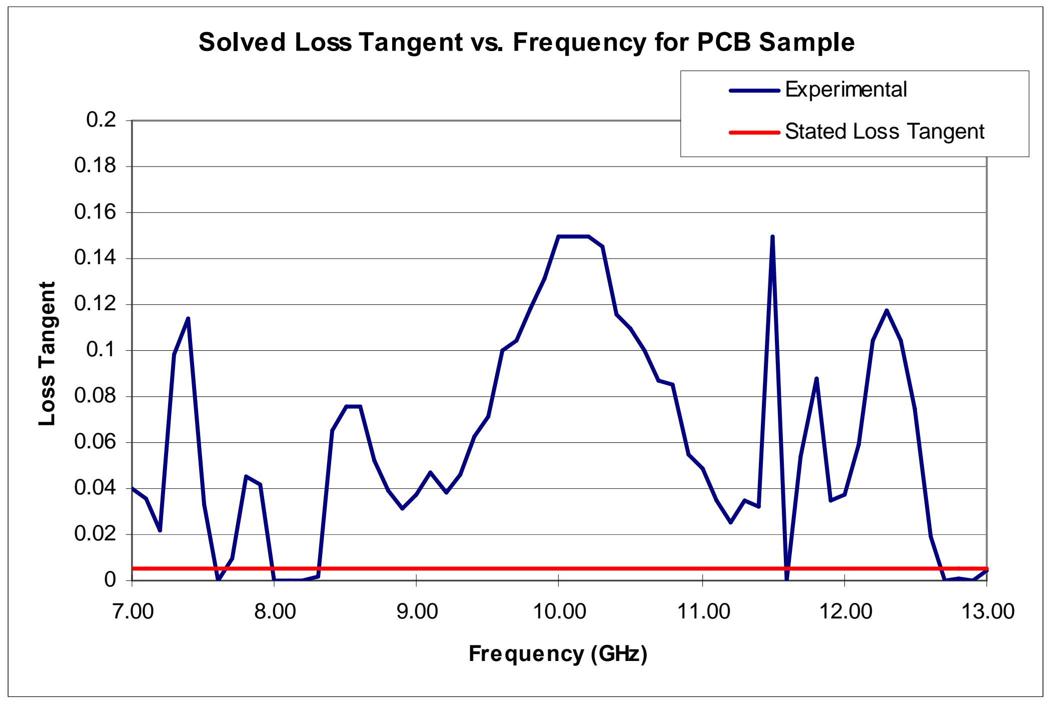

Figure 4-33. Loss tangent solution vs. frequency for PCB sample.

The ambiguous S-parameter variation between different low-loss materials makes it very difficult to obtain in the *tan(δ)* solution of low-loss dielectrics. For example, the theoretical results show the magnitude and phase difference between two Teflon samples with *tan(δ)*=0.001 and *tan(δ)*=0.01 to be only a slight fraction of a dB and degree, respectively. These quantities on the same level as network analyzer calibration errors. As the material loss increases, however, the variation is significant and solution precision is regained.

Chapter 5

Conclusion

In this thesis, a method has been presented to use a simulated error library to effectively characterize thin dielectric sheets of material using rectangular waveguides in the X-band. Supporting results were obtained by using a parallel-plate capacitor test fixture. Having data from separate methods and frequency ranges allows for extended analysis of the material's properties, as well as an added level of confidence in the results.

Summary

Chapter 2 introduced the basic concept of dielectric permittivity through the illustration of the bound charge polarization of a parallel-plate capacitor. A rundown of some commonly used dielectric characterization techniques was then presented, with some of the advantages and disadvantages highlighted for each method. Since technology and developments within the field of dielectric characterization are rapidly progressing, the list does therefore not include some of the newest methods, but does serve as an effective introduction and overview.

Chapter 3 discusses the theory and use of the parallel-plate capacitor for the purpose of dielectric characterization. When the electric field is assumed to be directed straight from one electrode to the other, the capacitance derivation is very straightforward and simplifies to a linear equation that is dependent only upon size of the plates and the electrical properties of the medium between the plates. The derivation neglects the fringing electric field at the edge of the plates, however. The assumption is facilitated in practice by the introduction of electrode guard rings, which remove the effects of the fringing fields from the capacitance measurements. To verify the capacitor theory, measurements taken with the HP 16451B dielectric test fixture, a guarded electrode structure, are presented.

Chapter 4 explores in depth the use of the rectangular waveguide for the electrical characterization of dielectric sheets of material. The structure of interest consists of a

thin sample placed in the cross-section of a short waveguide section, from which the resulting S-parameters are used to derive its complex permittivity. The theoretical S-parameters are found exclusively in terms of the thickness and complex permittivity of the sample. These theoretical parameters are compared to those from a comparable 3D electromagnetic simulation, from which a very close match is found. Next, an inverse solution algorithm is presented to determine the complex material properties given a set of experimental S-parameters. The algorithm makes extensive use of an error library, produced by the electromagnetic simulator, to remove the systematic error from the measurement.

Recommended Future Work

As previously stated, the preceding work of this chapter, while essential, is only an intermediate step in the long run of the project. While the sample-in-waveguide method works well for some material types, it is not suitable for flexible materials and also requires intricate cutting of the sample. To alleviate these problems, an alternative method that altogether avoids the insertion of material into the waveguide is more attractive. If the sample is placed between the two flanged waveguide sections, the measured S-parameters, along with the 3D-simulated error library, can be used to extrapolate the complex permittivity. The method does not suffer from the preceding drawbacks mentioned in chapter 4 and would be highly effective for the measurement of thin sheets of material, such as fabrics, which can not be easily placed inside of the waveguide. The proposed method has previously been impractical, since the development of field equations in such a situation is an arduous, if not impossible, task. With the help of the simulated error data, however, it now seems to be an optimistic possibility.

The major obstacle encountered with this proposed approach is in dealing with the waveguide discontinuity created by the separation of waveguide flanges. During close observation of the sample region, the lack of metal continuity through the sample region has been seen to produce standing waves and free radiation. In preliminary study, the high S-parameter sensitivity resulting from the lack of waveguide continuity through the sample material region has been shown to produce large errors that are sometimes

deemed unacceptable. While the method does introduce an air gap discontinuity in the inner waveguide walls, it seems to be possible to remove the effects of the resulting systematic error from the solution by means of the systematic error library. The approach would be very useful in a real-world sense, since the bulk of the time is spent producing the error library, while actual setup time required to take and analyze a measurement is relatively small. If increased accuracy in the solution is desired, however, many iterative simulations runs may be necessary.

Even though the method makes use of the rectangular waveguide geometry in this thesis, the idea of error removal through the use of a simulated error library can be expanded to include many other configurations. The approach holds massive potential for the future of dielectric characterization, as material properties can ideally be found in any situation where the fields can be accurately and precisely modeled. In fact, it may even be possible to extrapolate materials properties from cases in which no previous theoretical analysis has been conducted. Due to exorbitant advances in computing power, ultra-detailed simulations are now much more plausible than they were ten years ago. As a result, much smaller changes in dielectric constant and loss tangent can be resolved from the simulated and measured data.

This method will seemingly work best for thin materials, such as printed circuit boards, plastics, and fabrics. As the thickness of the material increases, the radiation and standing waves caused by the metallic discontinuity have been shown to cause a substantial increase in the magnitude and randomness of the systematic error. The increasing systematic error can cause the accuracy of the solution to decrease to unacceptable levels. Further investigation is required to more precisely determine the dependence of the error upon sample thickness and complex permittivity.

In addition, simulations of the guarded electrode capacitor structure are recommended. By employing the full-wave numerical solution, the effectiveness of the guard rings can be verified and any remaining fringing effects of the electric field can be accounted for.

Conclusions

This thesis has demonstrated the theory and implementation of the X-band rectangular waveguide, along with a 3D high frequency electromagnetic simulator, as a means to efficiently characterize the unknown properties of a test material. Using this methodology, the systematic error is accounted for by replicating the actual structure as a model within the 3D simulation software. For measurement geometries that are very convenient for the insertion of a test sample, but the complexity of the theoretical field calculations prevents the permittivity from being obtainable from the measured S-parameters, the 3D electromagnetic simulator is able to supplement or replace the theoretical calculations, thus moving the solution into the realm of a numerical solution rather than a theoretical solution. In addition, a parallel characterization method, the parallel-plate capacitor, has been employed to provide supporting results.

The waveguide technique presented in chapter 4 is still in its infancy, and further development is needed to develop it into a formidable material characterization method, but the idea of using a comprehensive error library shows promise. 3D electromagnetic simulators have become an increasingly invaluable tool in situations requiring extensive field analysis, and the trend is expected to continue for years to come.

References

1. Agilent, *Basics of Measuring the Dielectric Properties of Materials*. 2005, Agilent Technologies, Inc.: U.S.A. p. 1-32.
2. Balanis, C.A., *Advanced Engineering Electromagnetics*. 1989: John Wiley & Sons, Inc.
3. Baker-Jarvis, J., et al. (2004) *Measuring the Permittivity and Permeability of Lossy Materials: Solids, Liquids, Metals, Building Materials, and Negative-Index Materials*. NIST Technical Note **Volume**, 149
4. Ulaby, F.T., *Fundamentals of Applied Electromagnetics*. 2001, Upper Saddle River, NJ 07458: Prentice Hall. 433.
5. Grove, T.T., M.F. Masters, and R.E. Miers, *Determining Dielectric Constants Using a Parallel Plate Capacitor.* American Journal of Physics, 2005. **73**(1): p. 52-56.
6. Saed, M.A., S.M. Riad, and A. Elshabini-Riad, *Wide-Band Measurement of the Complex Permittivity of Dielectric Materials Using a Wide-Band Cavity.* IEEE Transactions on Instrumentation and Measurement, 1989. **38**(2): p. 488-495.
7. Riad, S.M. *The Deconvolution Problem: An Overview*. in *IEEE*. 1986.
8. Harrington, R.F., *Field Computation by Method of Moments*. 1st ed. 1982, Melbourne, FL: Krieger Publishing Co., inc.
9. Baker Jarvis, J., et al. (2004) *Measuring the Permittivity and Permeability of Lossy Materials: Solids, Liquids, Metals, Building Materials, and Negative-Index Materials*. NIST Technical Note **Volume**, 149
10. Olmi, R., et al., *Thickness-Independent Measurement of the Permittivity of Thin Samples in the X band.* Measurement Science and Technology, 2002. **13**: p. 503-509.
11. Sarabandi, K. and F.T. Ulaby, *Technique for Measuring the Dielectric Constant of Thin Materials.* IEEE Transactions on Instrumentation and Measurement, 1988. **17**: p. 631-636.
12. Goldberg, D.E., *Genetic Algorithms in Search, Optimization, and Machine Learning*. 1989, Reading, MA: Addison-Wesley.
13. Holland, J.H., *Adaptation in Natural and Artificial Systems*. 1975, Ann Arbor, MI: University of Michigan Press.
14. Afsar, M.N., J.R. Birch, and R.N. Clarke. *The Measurement of the Properties of Materials*. in *IEEE*. 1986: IEEE.
15. Su, W., S.M. Riad, and A. Elshabini-Riad, *Microwave Material Characterization Using Stripline Resonators.* Internation Journal for Hybrid Microelectronics, ISHM, 1991. **14**(2): p. 48-54.
16. Meng, B., J. Booske, and R. Cooper, *Extended Cavity Perturbation Technique to Determine the Complex Permittivity of Dielectric Materials.* IEEE Transactions on Microwave Theory and Techniques, 1995. **43**(11): p. 2633-2636.
17. Harrington, R.F., *Time-Harmonic Electromagnetic Fields*. 2001: Wiley-IEEE Press. 496.
18. Parkash, A., J.K. Vaid, and A. Mansingh, *Measurement of Dielectric Parameters at Microwave Frequencies by Cavity Perturbation Technique.* IEEE Transactions on Microwave Theory and Techniques, 1979. **27**(9): p. 791-795.

19. Sen, S., P.K. Saha, and B.R. Nag, *New Cavity Perturbation Technique for Microwave Measurement of Dielectric Constant.* Rev. Sci. Instrum., 1979. **50**(12): p. 1594-1597.
20. Popovic, D., et al., *Precision Open-Ended Coaxial Probes for In Vivo and Ex Vivo Dielectric Spectroscopy of Biological Tissues at Microwave Frequencies.* IEEE Transactions on Microwave Theory and Techniques, 2006. **53**(5): p. 1713-1722.
21. Baker-Jarvis, J., et al., *Analysis of an Open-Ended Coaxial Probe with Lift-Off for Nondestructive Testing.* IEEE Transactions on Instruments and Measurement, 1994. **43**(5): p. 711-718.
22. Begley, S. and P. Bartley *The Gated-Reflect-Line Calibration Technique Applied to Material Measurement*. Agilent Technologies **Volume**, 1-27
23. Grignon, R., et al. *Microwave Broadband Free-Space Complex Dielectric Permittivity Measurements on Low Loss Solids*. in *Instrument and Measurement Technology Conference*. 2003. Vail, CO: IEEE.
24. ASTM, *ASTM-D3380-90 Standard Test Method for Relative Permittivity and Dissipation Factor for Polymer-Based Microwave Circuit Substrates*, in *1990 Annual Book of American Society for Testing of Materials*. 1990, ASTM. p. 10.01.
25. Agilent, *16451B Dielectric Test Fixture Operation and Service Manual*. 2000, Agilent Technologies Japan, Ltd.: Japan.
26. HP, *4192A LF Impedance Analyzer Operating and Service Manual*. 2000, Agilent Technologies Japan, Ltd.: Japan. p. 1-469.
27. Bornemann, J. and R. Vahldieck, *Characterization of a Class of Waveguide Discontinuities Using a Modified TEmn Mode Approach.* IEEE Transactions on Microwave Theory and Techniques, 1990. **38**(12): p. 1816-1822.
28. Agilent, *Network Analyzer Basics*. 2004, Agilent Technologies, Inc.: U.S.A.
29. Agilent, *In-Fixture Measurements Using Vector Network Analyzers*. 2006, Agilent Technologies, Inc.: U.S.A.
30. Sadiku, M.N.O. and C.M. Akujuobi, *S-Parameters for Three and Four Cascaded Two-Ports*, Prairie View A&M University: Prairie View, TX. p. 1-5.
31. Pozar, D.M., *Microwave Engineering*. 2nd ed. 1998, New York, Chichester, Weinhein, Brisbane, Singapore, Toronto: John Wiley & Sons, Inc.
32. Davis, W.A., *S-Parameters and Automated Network Analyzers (ANA)*. 1999, Virginia Tech University: Blacksburg, VA. p. 1-33.